



University of Kentucky
UKnowledge

Theses and Dissertations--Physics and
Astronomy

Physics and Astronomy

2022

ANGULAR DISTRIBUTION OF ELECTRON-HELIUM SCATTERING IN THE PRESENCE OF A 1.17 eV LASER FIELD

BRIAN N. KIM

University of Kentucky, brian.kim@uky.edu

Digital Object Identifier: <https://doi.org/10.13023/etd.2022.200>

[Right click to open a feedback form in a new tab to let us know how this document benefits you.](#)

Recommended Citation

KIM, BRIAN N., "ANGULAR DISTRIBUTION OF ELECTRON-HELIUM SCATTERING IN THE PRESENCE OF A 1.17 eV LASER FIELD" (2022). *Theses and Dissertations--Physics and Astronomy*. 95.
https://uknowledge.uky.edu/physastron_etds/95

This Doctoral Dissertation is brought to you for free and open access by the Physics and Astronomy at UKnowledge. It has been accepted for inclusion in Theses and Dissertations--Physics and Astronomy by an authorized administrator of UKnowledge. For more information, please contact UKnowledge@lsv.uky.edu.

STUDENT AGREEMENT:

I represent that my thesis or dissertation and abstract are my original work. Proper attribution has been given to all outside sources. I understand that I am solely responsible for obtaining any needed copyright permissions. I have obtained needed written permission statement(s) from the owner(s) of each third-party copyrighted matter to be included in my work, allowing electronic distribution (if such use is not permitted by the fair use doctrine) which will be submitted to UKnowledge as Additional File.

I hereby grant to The University of Kentucky and its agents the irrevocable, non-exclusive, and royalty-free license to archive and make accessible my work in whole or in part in all forms of media, now or hereafter known. I agree that the document mentioned above may be made available immediately for worldwide access unless an embargo applies.

I retain all other ownership rights to the copyright of my work. I also retain the right to use in future works (such as articles or books) all or part of my work. I understand that I am free to register the copyright to my work.

REVIEW, APPROVAL AND ACCEPTANCE

The document mentioned above has been reviewed and accepted by the student's advisor, on behalf of the advisory committee, and by the Director of Graduate Studies (DGS), on behalf of the program; we verify that this is the final, approved version of the student's thesis including all changes required by the advisory committee. The undersigned agree to abide by the statements above.

BRIAN N. KIM, Student

Dr. Nicholas L. S. Martin, Major Professor

Dr. Christopher Crawford, Director of Graduate Studies

ANGULAR DISTRIBUTION OF ELECTRON-HELIUM SCATTERING IN THE
PRESENCE OF A 1.17 eV LASER FIELD

DISSERTATION

A dissertation submitted in partial
fulfillment of the requirements for
the degree of Doctor of Philosophy
in the College of Arts and Sciences
at the University of Kentucky

By
Brian N Kim
Lexington, Kentucky

Director: Dr. Nicholas L. S. Martin, Professor of Physics
Lexington, Kentucky
2022

Copyright© Brian N Kim 2022

ABSTRACT OF DISSERTATION

ANGULAR DISTRIBUTION OF ELECTRON-HELIUM SCATTERING IN THE PRESENCE OF A 1.17 eV LASER FIELD

We have measured relative differential cross sections for 350 eV electrons scattered by a helium target in the presence of 1.17 eV photons from an Nd:YAG laser. We report an angular distribution of free-free electrons that were scattered elastically at angles between 15° and 80° and of free-free electrons that underwent the process of electron-impact excitation of helium to its unresolved $(1s2s)^1S$ and $(1s2p)^1P$ excited states at angles between 1° and 80° . Our experiments test the momentum transfer dependence and the relationship between elastic and inelastic scattering in the Kroll-Watson approximation. We also explored potential light-dressed atom effects for inelastic scattering at low-scattering angles in helium.

We found good agreement between our experimental results and the Kroll-Watson approximation. Due to the presence of an unknown uncertainty in our apparatus, we are unable to unambiguously test the elastic-inelastic relationship of the KWA and our exploration into light-dressed atom effects are inconclusive. Methods to potentially identify and reduce the impact of this unknown uncertainty are discussed for future works.

KEYWORDS: atomic physics, free-free transitions, helium, laser-assisted free-free scattering, angular distribution, electron scattering

Brian N Kim

May 4, 2022

ANGULAR DISTRIBUTION OF ELECTRON-HELIUM SCATTERING IN THE
PRESENCE OF A 1.17 eV LASER FIELD

By
Brian N Kim

Dr. Nicholas L. S. Martin
Director of Dissertation

Dr. Christopher Crawford
Director of Graduate Studies

May 4, 2022
Date

Dedicated to all my friends and family.

ACKNOWLEDGMENTS

I would like to thank my advisor, Dr. Nick Martin, whose patience, guidance, and support during my graduate career made me the scientist that I am today. The research described in this thesis was possible because of you. I would like to thank the members of my PhD committee: Dr. Wolfgang Korsch, Dr. Tim Gorringer, and Dr. Steve Yates for your guidance, encouragement, and insightful comments during my PhD work. I would also like to thank Dr. Chris Crawford who encouraged me to never give up during my graduate career.

I would like to thank Bruno deHarak and Mike Weaver for all your help, support, and insightful discussions we've had related to this work. Thank you to Mark Broering, Alina Aleksandrova, Laura Kelton, and John Connell for their encouragement and friendship. Thank you to my family who always supported me.

Finally, I would like to thank Victoria Bauer for the love, support, and encouragement she has given me through one of the most challenging part of my life. Thank you for always being by my side.

This work was supported by the United States National Science Foundation under Grants Nos. PHY-1607140 and PHY-2010102 (N. L. S. Martin).

TABLE OF CONTENTS

Acknowledgments	iii
List of Tables	vi
List of Figures	vii
Chapter 1 Introduction	1
1.1 Experiments in Laser-Assisted Free-Free Scattering	4
1.1.1 Elastic Free-Free Experiments	4
1.1.2 Inelastic Free-Free Experiments	11
Chapter 2 Theory	13
2.1 Scattering Cross Section	13
2.1.1 Differential Scattering Cross Section	14
2.2 Classical Free-Free Scattering	15
2.3 Quantum Scattering Theory	18
2.3.1 Volkov Wavefunction	19
2.4 Kroll Watson Approximation	20
2.4.1 Redefining x	23
2.4.2 Relative Cross Sections	25
2.5 Light-Dressing Effects	27
2.5.1 In-House Inelastic Light-Dressed Model	31
Chapter 3 Experimental Apparatus	35
3.1 Vacuum System	36
3.2 Electron Gun	38
3.2.1 Electron Gun Tuning	40
3.3 Gas Jet Nozzle	40
3.4 Scattered-Electron Detector	41
3.4.1 Electrostatic Lenses	43
3.4.2 Electrostatic Energy Analyzer	43
3.4.3 Tuning	44
3.5 Data Acquisition	45
3.5.1 Position-Sensitive Detector	45
3.5.2 Data Acquisition Device	48
3.5.3 Nuclear Instrumentation Modules	48
3.6 Laser	50
3.6.1 Flash Lamp Degradation and Measuring Pulse Width	51
3.7 Timing	52
Chapter 4 Data and Analysis	54

4.1	Free-free Count Rate	54
4.2	Determination of the Elastic and Inelastic Scattering Intensities . . .	57
4.3	Relative Cross Section	60
	4.3.1 PSD Dead-Time Effects	60
	4.3.2 Additional Free-Free Transition Corrections	62
4.4	Correcting for Laser Intensity Variations and Other Effects	63
4.5	Angular Distributions	65
	4.5.1 Elastic Free-Free Angular Distribution	65
	4.5.2 Inelastic Free-Free Angular Distribution	67
	4.5.3 Reanalyzed: Uncertainty of Apparatus	71
Chapter 5 Summary and Conclusion		76
Appendices		78
	Appendix A: Statistics	78
Bibliography		80
Vita		88

LIST OF TABLES

2.1	Values of the parameters used in the argument of KWA	26
2.2	Various static dipole polarizabilities used to plot the Zon model	28
3.1	The timing of major events during the experiment.	53
4.1	Elastic free-free relative cross sections	65
4.2	Inelastic free-free relative cross sections	69
4.3	Elastic free-free relative cross sections with the uncertainty of the apparatus being added linearly.	71
4.4	Inelastic free-free relative cross sections with the uncertainty of the apparatus being added linearly for various scattering angles.	73

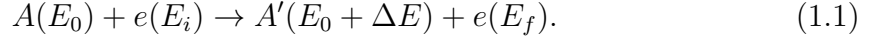
LIST OF FIGURES

1.1	Schematic of the energy profile of elastically scattered electrons	2
1.2	Electron energy-loss spectrum of electron-argon scattering.	5
1.3	Free-free transitions for helium at incident electron energies	7
1.4	Free-free signal for 350 eV electron-helium scattering with respect to polarization direction	7
1.5	The free-free signal for different targets: helium, argon, and molecular nitrogen.	8
1.6	The free-free signal for 350 eV electron-argon scattering with respect to the scattering angle	8
1.7	The free-free angular distribution for one photon absorption of xenon.	10
2.1	Schematic of an electron-atom collision in an oscillating electric field.	15
2.2	Elastic and inelastic KWA.	26
2.3	The Zon model for various static dipole polarizabilities	29
2.4	Zon model for small scattering angles.	29
2.5	The results of the <i>qualitative</i> in-house light dressing model.	34
3.1	Schematic of the LAFF spectrometer.	35
3.2	Photograph of the LAFF spectrometer.	36
3.3	Schematic of the vacuum system.	37
3.4	Diagram of the electron gun.	39
3.5	Wiring diagram of the electron optics of the electron detector.	42
3.6	Schematic of the PSD and NIM with wiring diagram.	46
3.7	PSD electronic dead-time curves.	47
3.8	Schematic of signal processing.	49
3.9	Diagram of laser bench.	50
3.10	Degraded flash lamps.	52
3.11	Schematic of the timing diagram.	53
4.1	A schematic of the energy profile of scattered electrons with the laser on and off.	54
4.2	An example of a timing spectrum.	55
4.3	Elastic-scattering peak profile for different detunings of the first lens.	57
4.4	Comparison of when detector is tuned and detuned	59
4.5	STR vs. NIM count rates	61
4.6	Time-dependent variations of relative cross sections for one photon free-free processes.	64
4.7	Elastic free-free angular distribution for one photon processes	66
4.8	Helium energy states.	67
4.9	Electron energy-loss spectrum	68
4.10	Inelastic LAFF angular distribution for one photon processes.	70

4.11 Elastic free-free angular distribution with the uncertainty of the apparatus being added linearly.	72
4.12 Inelastic free-free angular distribution with the uncertainty of the apparatus being added linearly.	74

Chapter 1 Introduction

What happens when an atom is hit by a free electron¹ while in an electromagnetic field? First consider the case without the field. This process can be described by the following:



The reaction 1.1 refers to a free electron with some initial kinetic energy E_i being scattered off a ground state atom A (with the ground state energy E_0). After the collision, the free electron is scattered with some final kinetic energy E_f and the atom is in some final state A' . If the final state of the atom is still in its ground state (elastic-scattering), then the atom will still have its ground state energy E_0 . If the atom is in some excited state (electron-impact excitation), it will have the energy $E_0 + \Delta E$, where ΔE is the excitation energy of the state. In this work, we are interested in the case where the atom stays neutral and we ignore the case where the atom is ionized (electron impact ionization). In this reaction, we can also determine E_f . Due to the mass of the atom being orders of magnitude greater than the electron, the amount of kinetic energy transferred to the atom is negligible. Thus, for elastic-scattering $E_f \approx E_i$ and for electron-impact excitation² $E_f = E_i - \Delta E$.

Now we consider the same scattering process but in the presence of an electromagnetic field that is represented as $\mathcal{N}\hbar\omega$ where \mathcal{N} and ω refer to the number of photons in, and the angular frequency of, the field, respectively, \hbar is the reduced Planck constant. This process can be described by:



In this reaction, the electron interacts with the electromagnetic field and energy can be transferred to or from the field. This is represented as the electron absorbing or emitting photons. This process is referred to as *free-free transitions* due to the incident and scattered electron being free[1, 2]. Free-free transitions can also be described in terms of bremsstrahlung, where the absorption and emission of a photon by the electron can be referred to as inverse and stimulated bremsstrahlung, respectively[3]. *Laser-assisted free-free* (LAFF) scattering refers to free-free experiments where the electromagnetic field is supplied by a laser, i.e. electron-atom³ scattering in a laser field. In this work, elastic electron-atom scattering in the presence of a laser field will be referred to as *elastic LAFF*⁴ scattering and the inelastic equivalent as *inelastic*

¹A *free electron* is an electron that is not bounded by any potential. Therefore, all the energy of the electron is purely kinetic. In this work, unless stated otherwise, *electron* refers to a free electron.

²I will occasionally refer to electron-impact excitation as *inelastic scattering*.

³LAFF scattering can also be performed with molecular targets. However, this work uses atomic helium as the target and thus I will refer to the process as electron-atom scattering.

⁴In other works, LAFF is referred to as *free-free transitions*, a term I will use occasionally as well. In other works[4], elastic LAFF scattering is referred to as *laser-assisted elastic electron scattering* (LAES).

$LAFF^5$ scattering. Figure 1.1 shows a schematic of the energy profile of elastically scattered electrons when the laser is present and not present.

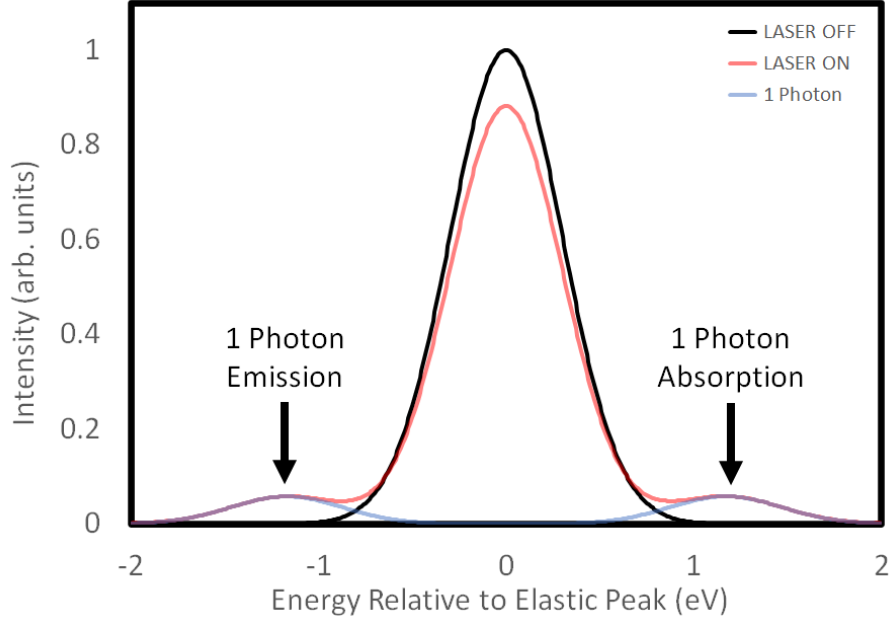


Figure 1.1: Schematic of the energy profile of elastically scattered electrons when the laser is not present (black) and is present (red). The energy profile of scattered electrons that have absorbed or emitted one photon predicted by the Kroll-Watson approximation when the laser is present is also plotted (blue). The energy width of the elastic peak is due to the thermal width of the electrons emitted by the cathode in our non-monochromated electron gun.

When the laser is not present, one sees the elastic-scattering peak. When the laser is on, note that the peak is reduced and two additional peaks are formed one photon energy away from the scattering peak (in this scenario, photon energy is 1.17 eV). These two peaks are the *free-free peaks*, they are electrons that were elastically scattered but also underwent free-free transitions/scattering.

Free-free transitions are not only of interest in fundamental collision physics. It is also a phenomenon of interest in astrophysics and plasma physics. It was proposed by Pannekoek[7] to be important for determining the infrared opacities of certain stars[8]. It is essential in plasma modeling due to the importance of the laser-plasma interaction[9]. A method of heating low density plasma with a laser primarily relies on free-free transitions[10]. Free-free transitions are the dominant radiation transport in air plasma, e.g. cascade arcs[11].

⁵In other works, inelastic LAFF is referred to as *simultaneous electron-photon excitation* (SEPE)[5], *inelastic free-free transition* (IFFT), or *laser-assisted inelastic electron scattering*[6].

A theoretical model by Kroll and Watson[12] has widely been compared to experimental free-free data. It is a semiclassical model in the *soft-photon limit*⁶ that uses quantum electron-atom scattering theory in the presence of a classical electromagnetic field. The model relates the free-free differential cross section $d\sigma_{FF}^n/d\Omega$ (into the solid angle $d\Omega$) to the field-free (i.e., in the absence of a laser field) differential cross section of the scattering peak $d\sigma/d\Omega$. It has the form of

$$\frac{d\sigma_{FF}^n}{d\Omega} = \frac{p_f}{p_i} J_n^2(x) \frac{d\sigma}{d\Omega} \quad (1.3)$$

$$x = -0.0220\lambda^2 I^{1/2} E_i^{1/2} \left(\frac{\hat{\epsilon} \cdot \mathbf{Q}}{p_i} \right) \quad (1.4)$$

where n is the number of photons absorbed ($n < 0$) or emitted ($n > 0$); J_n is the Bessel function of the first kind of order n ; p_i and p_f are the initial and final momenta of the electron, respectively; λ , I , and $\hat{\epsilon}$ are the wavelength in μm , intensity in GW/cm^2 , and polarization direction of the field, respectively; E_i is the incident electron energy in eV; and $\mathbf{Q} = \mathbf{p}_f - \mathbf{p}_i$ is the momentum transfer.

In LAFF scattering, there are three interactions: electron-atom, laser-electron, and laser-atom. This model assumes that the laser-atom interaction is negligible; the purpose of the atom is allow energy and momentum to be conserved during this process. The Kroll-Watson approximation (KWA) will be covered in section 2.4.

In this work, we will measure the relative differential cross sections of 350 eV electrons scattered by a helium target in the presence of a laser field from an Nd:YAG laser as the scattering angle is adjusted. Our results are compared to the KWA to test its momentum transfer dependence in helium for elastic and inelastic scattering. We also discuss the search for deviations from the KWA due to light-dressed atom effects (when the laser-atom interaction is not negligible). To our knowledge, this is the first angular distribution measurement of electron-helium elastic and inelastic scattering in a Nd:YAG laser field for electrons with 350 eV. In previous work, we presented the angular distribution of elastic LAFF scattering of argon and found it consistent with the KWA[14]. Thus, we expect that elastic LAFF scattering of helium will also be found consistent with the KWA. Due to the presence of a high dipole polarizability of certain excited states of helium, deviations from KWA at small inelastic scattering angles are expected.

We will first briefly cover the experimental history of LAFF scattering experiments. Chapter 2 will cover the relevant classical and quantum scattering theory for these processes. The derivation of the Kroll-Watson approximation will be covered and light-dressed atom effects will be discussed. Chapter 3 will describe our experimental apparatus, chapter 4 will discuss the analysis and results of our work, and chapter 5 contains our summary and conclusions.

⁶The soft-photon limit is when photon energy transferred is much smaller than the kinetic energy of the scattered electron and any transition threshold energy[13].

1.1 Experiments in Laser-Assisted Free-Free Scattering

A comprehensive review of free-free experiments was given by Mason in 1993[1] and of free-free theories was given by Ehlötzky in 1998[15]. Here we will briefly summarize early LAFF experiments⁷ and discuss more recent developments. This section is split into two parts: elastic LAFF and inelastic LAFF experiments.

1.1.1 Elastic Free-Free Experiments

In 1976, Andrick and Langhans[16] observed free-free transitions using an in-house continuous-wave CO₂ laser with a wavelength of 10.6 μm (photon energy of 0.117 eV). An electron beam was scattered by argon atoms in the presence of the laser field. They observed free-free peaks one photon energy away from the elastic-scattering peak. In 1978, they measured the ratio of the free-free and field-free elastic cross section with a laser intensity of 7 kW/cm²[3]. They found their results to be consistent with a perturbative model in the soft-photon limit by Krüger and Schulz[17] and a model by Geltman[18] that evaluated the transition matrix element exactly using computed elastic-scattering wave functions.

The first multiphoton free-free processes were observed in 1977 by Weingartshofer *et al.*[19] by scattering electrons off argon atoms in the presence of a *pulsed* CO₂ laser. By using a pulsed laser, they were able to achieve laser intensities nearly on the order of GW/cm². At these intensities, multiphoton processes are expected to occur and can be described by semiclassical, soft-photon models. They used a model by Krüger and Jung that is similar to the Kroll-Watson approximation but with a modification to account for their less-than-ideal laser pulse conditions[20]. Up to three photon processes were seen. Their results can be seen in figure 1.2.

Weingartshofer *et al.*[2] later carried out several qualitative studies of multiphoton free-free processes with argon and hydrogen molecules in the presence of a laser field from their pulsed CO₂ laser. By taking advantage of the temporal profile of the laser beam, they were able to compare free-free signals at different laser intensities. They also adjusted the incident electron energy and the scattering geometry. They found their results to be in qualitative agreement to the theory by Krüger and Jung (and by extension the KWA)[20]. In 1981, they reported quantitative measurements of multiphoton free-free transitions with argon and found up to eleven-photons processes. However, the lack of a single-mode, homogeneous laser beam made direct tests of the KWA not experimentally feasible. Their measurements were indirect tests of the incident electron energy and scattering geometry dependence. Due to their large statistical uncertainties, no definite conclusions were made[21].

In 1985, Bader performed free-free experiments with a liquid-nitrogen cooled continuous-wave CO laser with an output power of ~ 20 W. The laser was focused down to have a diameter of ~ 1.5 mm (which corresponds to an intensity of ~ 1.1 kW/cm²). The wavelength of the CO laser is 5.3 μm and tested the wavelength dependence of the KWA. He found his results to be consistent with the model[22].

⁷I define “early experiments” as the experiments that are discussed in these two reviews.

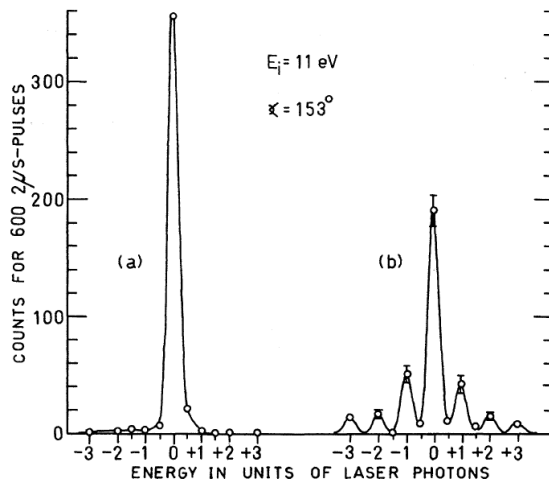


Figure 1.2: Electron energy-loss spectrum of electron-argon scattering. The left is when the CO₂ laser field was not present while it was present on the right. Figure from [19].

In 1987, Wallbank *et al.* started a series of experimental tests of the KWA. They experimentally measured the differential cross sections for free-free transitions in argon as a function of laser intensity. With their pulsed CO₂ laser with a hybrid oscillator, they were able to produce both single longitudinal-mode and multimode laser pulses[23, 24]. They continued their work in argon by measuring the free-free differential cross sections for incident electron energies from 8 to 20 eV through scattering angles 10° and 140°. They measured up to three photon processes[25].

They continued their work by measuring the differential free-free cross sections of helium with respect to incident electron energy at a scattering angle of 9°[25, 26, 27]. They explored the soft-photon limit by using a scattering geometry that was known to have produced experimental results consistent with KWA but used incident electron energies ranging from 0.2 to 2.5 eV (which is comparable to the 0.117 eV photons from the CO₂ laser)[28]. They then performed series of experiments where the laser polarization was perpendicular to the scattering plane where KWA predicts vanishing cross sections. The experiments were performed with incident electron energies from 1 to 20 eV and scattering angles from 14° to 140°. They concluded that KWA is inadequate for describing free-free transitions for low-energy electrons in the presence of a CO₂ laser field[29].

Their studies were continued by performing two sets of free-free experiments with helium with an incident electron energy of 22 eV for various scattering geometries. The first set had the laser polarization parallel to the incident electron momentum for scattering angles between 20° and 70°. The second set had a fixed 70° scattering angle but changed the laser polarization direction while it was still parallel with the scattering plane. Their results were compared to both the KWA and a more sophisticated *R*-matrix Floquet calculation. Both models were in good agreement with the experimental data[30]. When the triatomic CO₂ was used as the target,

they found good qualitative agreement with KWA when the laser polarization was parallel to the scattering plane. However, when the polarization was perpendicular to the plane, they still observed a free-free signal despite the predictions of KWA. They believe it may have been due to the presence of vibrational structure in the ground state of CO_2 [31].

In 2011, the Martin laboratory started a series of experiments to test the KWA for LAFF experiments in an Nd:YAG laser field. They explored the incident electron energy dependence of KWA by performing one photon emission experiments with helium. The scattering angle was 135° to align the electron-detector with the laser polarization. Various incident electron energies ranging from 50 to 350 eV were used[32]. Their results are shown in figure 1.3. They then performed an experiment to test the KWA dependency on the direction of polarization. Electrons at varying incident energies were scattered by helium. The scattering angle was 90° and the angle between the electrons and laser beam was 45° . The laser beam went through a beam-splitter cube and a rotatable $\lambda/2$ -plate before reaching the *interaction region*⁸. The beam-splitter cube ensures only horizontally polarized light is transmitted and the $\lambda/2$ -plate rotates the direction of the linearly-polarized light. Thus, the polarization of the laser can be rotated on a plane that is perpendicular to the scattering plane[33, 34]. Their results are shown in figure 1.4. (Simulations run by deHarak *et al.* explored the effects of double scattering in free-free experiments as a possible explanation for non-vanishing free-free cross sections forbidden by KWA[34].) The Martin laboratory also explored the target independence of KWA by performing one, two, and three photon processes in helium, argon, and molecular nitrogen[35]. These results are shown in figure 1.5. Other experiments explored the momentum transfer dependence of elastic electron-argon LAFF scattering. Electrons with an incident energy of 350 eV were scattered by argon atoms at various scattering angles between 4° and 80° [14]. The results are shown in figure 1.6 and were found to be consistent with the Kroll-Watson approximation.

This work is a continuation of testing the validity of the Kroll-Watson approximation for the momentum transfer dependence of elastic and inelastic electron-helium LAFF scattering in an Nd:YAG laser field.

⁸The interaction region is where the electrons and atomic targets intersect.

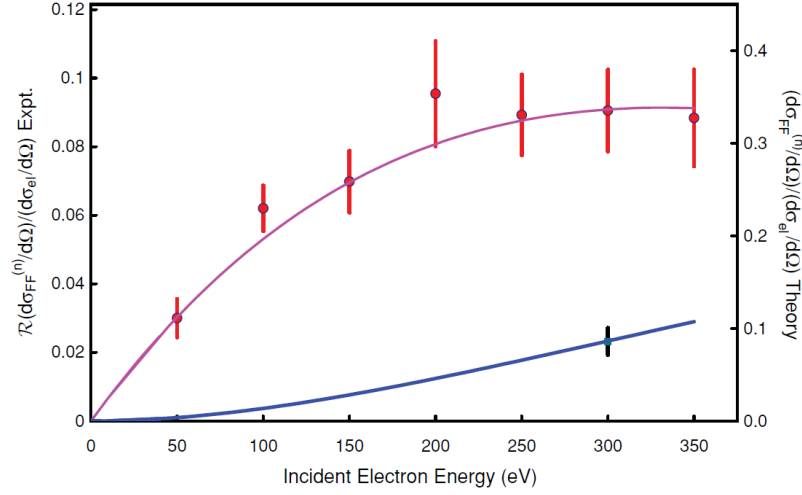


Figure 1.3: Free-free transitions for helium at incident electron energies from 50 to 350 eV at a scattering angle of 135° . The red points are for one-photon emission and the blue point is for two-photon emission. The lines are fitted KWA calculations for one-photon (red) and two-photon (blue) emission. Figure from [32].

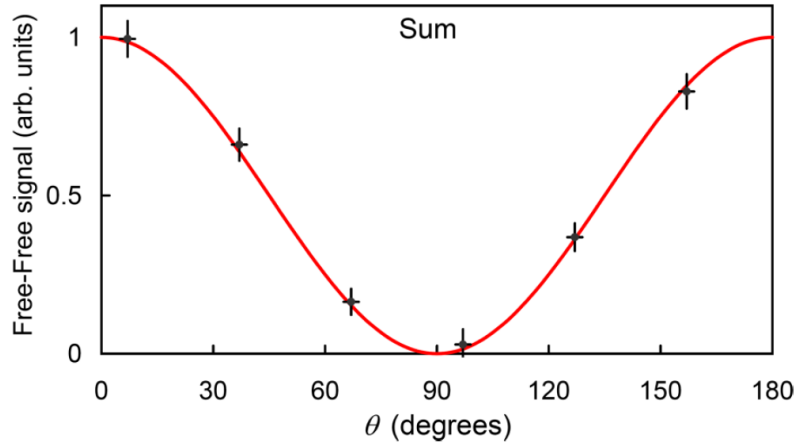


Figure 1.4: Free-free signal for 350 eV electron-helium scattering with respect to polarization direction. The polarization direction was varied in a plane that is perpendicular to the scattering plane (0° and 180° is parallel with the scattering plane while 90° is perpendicular to the plane). The scattering angle is 90° . The red curve is the KWA. Figure from [33].

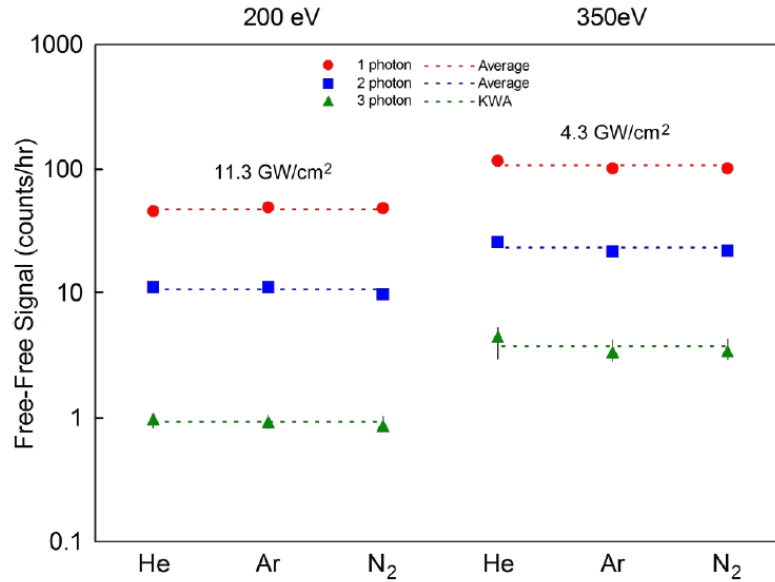


Figure 1.5: The free-free signal for different targets: helium, argon, and molecular nitrogen. The scattering angle is 90° . Figure from [35].

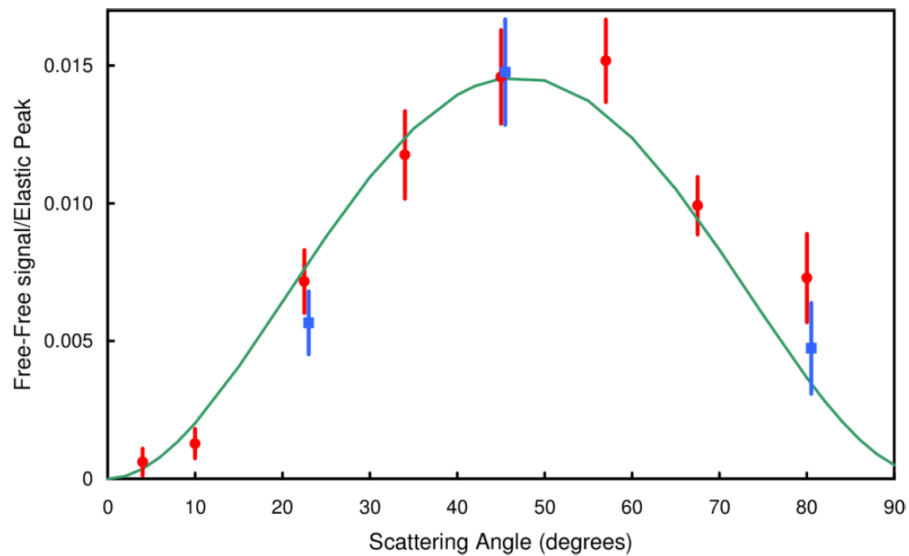


Figure 1.6: The free-free signal for 350 eV electron-argon scattering with respect to the scattering angle. The red data point had an estimated pressure of 1.0 torr at the interaction region while the blue data points had an estimated pressure of 0.1 torr. The green line is the KWA. Figure from [14].

In 2010, Kanya *et al.* performed laser-assisted free-free scattering experiments with xenon. 1 keV electrons were scattered by xenon in the presence of a femtosecond, near-infrared Ti:sapphire laser field (corresponding photon energy of 1.56 eV)[36]. In 2015, they reported the first unambiguous experimental observation of light-dressed atom effect in xenon. Their results are shown in figure 1.7. They observed a peak profile at small scattering angles ($< 0.5^\circ$) which was not predicted by the KWA[37]. They compared their results to calculations based on a model by Zon[38] that stated light-dressing effect are proportional to the dipole polarizability of the target atom. These calculations showed that the peak profile at small scattering angles can be interpreted as light-dressed atom effect. They noted that the discrepancies from the Zon model for scattering angles less than 0.2° may have been due to a slight misalignment between the electrons and laser beams[37, 39].

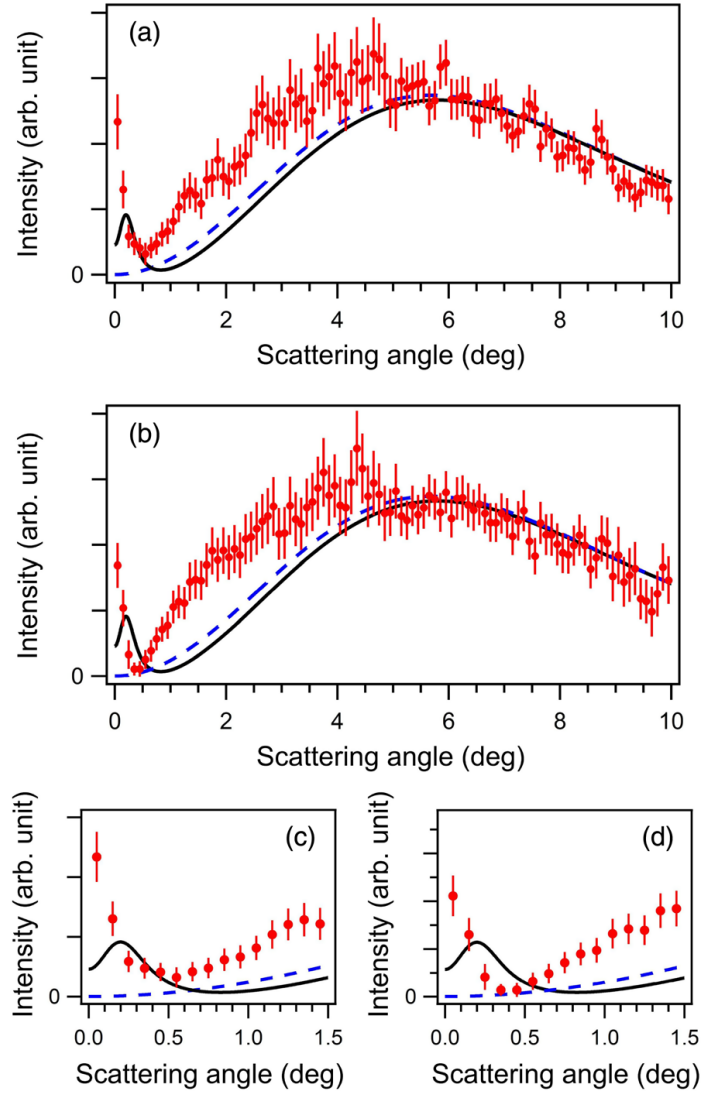


Figure 1.7: The free-free angular distribution for one photon absorption (a) and emission (b) of 1 keV electron-xenon scattering in a Ti:sapphire laser field with a corresponding photon energy of 1.56 eV. Plots (c) and (d) are the expanded views of (a) and (b), respectively. The blue dashed-line is the KWA and the black solid-line is a modified Zon model. Figure from [37].

1.1.2 Inelastic Free-Free Experiments

An inelastic free-free transition is when an electron is inelastically scattered by an atomic target in the presence of a laser field. In addition to the energy lost in the collision, the electron may absorb or emit photons from or to the laser field. The first observation of inelastic free-free transitions was reported by Mason and Newell in 1987[40, 5]. Low-energy electrons were scattered by ground state helium atoms in a continuous-wave CO₂ laser field. The electron energy was below the threshold of excitation to the metastable 2³S excited state. However, the helium atom can be excited by a combination of electron-impact excitation and photon absorption. This process is known as simultaneous electron-photon excitation (SEPE). In 1989, Wallbank *et al.* performed their own inelastic free-free experiments using a pulsed CO₂ laser. Following a similar procedure to Mason and Newell, they detected metastable 2³S state more than one photon energy away from the excitation energy. This was the first multiphoton inelastic free-free transition process observed[41]. Geltman and Maquet extended the KWA for inelastic free-free transitions and found good qualitative agreement between the KWA, the experimental results of Mason and Newell, and Wallbank *et al.*[42].

Mason and Newell continued their work by changing the polarization of their laser from linear to circular. Their results were consistent with KWA for electron energies above the excitation energy for the 2³S excited state of helium but there were qualitative differences for electron energies below it[43].

Wallbank *et al.* continued their work by exploring the laser intensity and polarization direction dependence of the inelastic KWA. They found qualitative agreement between their experimental results and the model[44]. They also measured the relative free-free cross sections of the 2¹S excited state of helium and the 2³P excited state of argon and neon. These were the first results for states other than the 2³S state of helium[45]. Then they performed free-free experiments with incident electron energy of 40 eV, much higher than the excitation energies for both the 2¹S and 2¹P excited states of helium. They were able to observe the one photon free-free transitions of the two excited states of helium[46]. An in depth study of the 2¹P excited state of helium was performed for various incident electron energies and scattering angles from 36 to 70 eV and 13° to 31°. They concluded that there was enough of a disagreement with KWA where laser-atom interactions may need to be considered[47]. Recently, Ajana *et al.* performed inelastic free-free experiments for electron-helium scattering of the 2¹P excited state using the same apparatus. They measured free-free angular distributions of one photon processes using 45 eV electrons between the scattering angles 5° and 35°. They found good qualitative agreement between their experimental results and the KWA when the laser intensity was time-averaged. However, they noticed signs of structure at scattering angles below 15°[48].

Inelastic free-free transitions in helium were observed in an Nd:YAG laser field by Luan *et al.* They measured the cross section of the 2³S and 2¹S excited states of helium with and without the laser field being present. They noticed a decrease in the threshold incident electron energy necessary to excite a ground state helium atom to these excited states. However, as the incident electron energy was increased, the cross

section started to decrease while the laser field was present. Eventually, the laser-on cross section was lower than the laser-off cross section. They believe this may have been due to multiphoton ionization of the metastable states of helium[49].

Chapter 2 Theory

In this chapter, we will discuss the theory of free-free scattering. We begin by first discussing how scattering is quantified in terms of cross sections.

2.1 Scattering Cross Section

Scattering theories and experiments are quantified by the concept of a *cross section*, which can be modeled by theories and measured by experiments. It is useful to first discuss cross sections in the framework of classical mechanics before moving to the quantum analog. The classical scattering theory covered here is primarily based on the text *Classical Mechanics* by John R. Taylor[50].

When a projectile approaches a target, the target will exert a force on it causing the projectile to be deflected or *scattered*. Attempting to quantify every aspect of the projectile's interaction with a target is not practical. However, if there are many similar projectiles and many similar targets, we can look at the statistical distribution of the scattered projectiles to gain insight into the projectile-target interaction.

Consider a finite-sized beam that consists of non-interacting, monoenergetic projectiles that is directed towards a target assembly that consist of many identical targets. The assembly is considered *thin* so we can assume any individual projectile will only interact with at most one target. The region where the projectile beam and the target assembly intersect is referred to as the *interaction region*. At the interaction region, the projectile can *hit* a target and be scattered or it can miss. The probability of a *hit* is dependent on how much of the cross-sectional area *Area* of interaction region was *filled* (i.e., a target was present instead of empty space). Note that *Area* of the interaction region is also the cross-sectional area of the projectile beam. Then the probability of a projectile being scattered is

$$\text{Probability of scattering} = \frac{N_{target} \sigma}{Area} \quad (2.1)$$

where N_{target} is the number of targets in *Area* and σ is the cross-sectional area of one target and is often referred to as the *total cross section*. σ is dependent on the projectile, target, and the energy of the incident projectile[51]. Thus, finding σ gives us information on the projectile-target interaction for a given incident energy. This can be done by sending a known number of projectiles per unit time $\dot{N}_{incident}$ at the targets and measuring the number of projectiles that are scattered per unit time $\dot{N}_{scattered}$ giving us the following relationship:

$$\dot{N}_{scattered} = \frac{\dot{N}_{incident} N_{target}}{Area} \sigma. \quad (2.2)$$

Let us define the incident projectile flux $F_{incident} = \dot{N}_{incident}/Area$, the number of incident projectiles per unit time that traverses the cross-sectional area of the

projectile beam. After substituting in $F_{incident}$ and rearranging equation 2.2, we find that

$$\sigma = \frac{\dot{N}_{scattered}/N_{target}}{F_{incident}}. \quad (2.3)$$

The total cross section is the ratio of all scattered projectiles per unit time per target and the incident flux.

2.1.1 Differential Scattering Cross Section

In many instances, we want to know how the projectile-target interaction depends on a certain physical quantity such as projectiles being scattered in a specific direction. For simplicity, we will define a coordinate system based on one projectile being scattered by one target. Since the projectile can be scattered in any direction from the point of collision (where the projectile interacted with the target), it is natural to use a spherical coordinate system where the point of collision is the origin. Then we have the polar angle θ and azimuth angle ϕ . After the collision, the projectile is scattered into some solid angle $d\Omega$. A solid angle can be considered the three-dimensional analog to angular displacement. In spherical coordinates, it is defined as

$$d\Omega = \sin \theta \, d\theta \, d\phi. \quad (2.4)$$

Experimentally, one puts the detector at the *scattering angle* θ_{scatt} facing the origin and measure the number of scattered projectiles. The scattering angle is defined as the angle between the momentum of the projectile before (initial) and after (final) the collision. The detector will have a finite angular acceptance that can measure scattered projectiles within a certain solid angle $\Delta\Omega$. However, we will continue assuming our angular acceptance is the unit solid angle $d\Omega$. Let us adjust equation 2.2 where we account for the angular acceptance.

$$\dot{N}_{scattered} \text{ (into } d\Omega) = \frac{\dot{N}_{incident} N_{target}}{Area} d\sigma \text{ (into } d\Omega) = \frac{\dot{N}_{incident} N_{target}}{Area} \frac{d\sigma}{d\Omega} d\Omega. \quad (2.5)$$

We use $\dot{N}_{scattered}$ (into $d\Omega$) since we only consider the scattered projectiles that enter into the solid angle $d\Omega$ per unit time. Since the only change is what is being measured, the incident projectile beam and target assembly are not changed. $d\sigma$ (into $d\Omega$) is the cross-sectional area of the target where a projectile will be scattered into the solid angle $d\Omega$. In equation 2.5, I used the relationship

$$d\sigma \text{ (into } d\Omega) = \frac{d\sigma}{d\Omega} d\Omega \quad (2.6)$$

where factor $\frac{d\sigma}{d\Omega}$ is the *differential cross section*¹. Note that if $\frac{d\sigma}{d\Omega} d\Omega$ is integrated over all solid angles, we obtain the total cross section.

$$\sigma = \int \frac{d\sigma}{d\Omega} d\Omega = \int_0^{2\pi} \int_0^\pi \frac{d\sigma}{d\Omega}(\theta, \phi) \sin \theta \, d\theta \, d\phi \quad (2.7)$$

¹In this work, the differential cross section is the differential with respect to the solid angle. However, it can be with respect to any combination of variables describing the scattering, such as energy and/or solid angle.

where we show explicitly the angular dependence of the differential cross section.

By rearranging equation 2.5 and substituting $F_{incident}$ we find that

$$\frac{d\sigma}{d\Omega}(\theta, \phi) = \frac{\dot{N}_{scattered}(\text{into } d\Omega)/N_{target}/d\Omega}{F_{incident}}. \quad (2.8)$$

The differential cross section is the ratio of projectiles scattered into the solid angle $d\Omega$ per unit time per target per unit solid angle and the incident flux.

2.2 Classical Free-Free Scattering

We now derive the classical differential cross section for free-free scattering. The derivation here is similar to that of Kroll & Watson[12] and Madsen[13].

Consider a free electron being scattered by an atom in the presence of an electromagnetic field as shown in figure 2.1. \mathbf{p}_α and \mathbf{p}_β refer to the instantaneous momenta of the electron before and after the collision, respectively. \mathbf{p}_i is the asymptotic, time-averaged momenta of \mathbf{p}_α and \mathbf{p}_f is the same to \mathbf{p}_β . \mathbf{p}_i and \mathbf{p}_f are the observable linear momenta of the electron (i.e., the momenta that can be measured). We consider the collision to be instantaneous, thus \mathbf{p}_α and \mathbf{p}_β occur at the same time at the same phase of the electromagnetic wave.

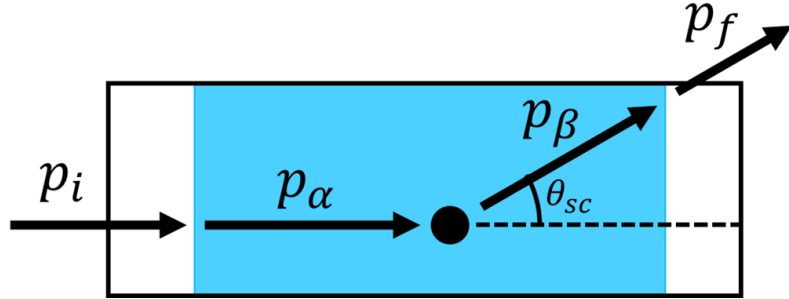


Figure 2.1: Schematic of an electron-atom collision in an oscillating electric field. The momenta are defined in the text. The blue region represent the electron in the presence of an external electromagnetic field.

Since we are in the classical framework, we only consider elastic electron-atom scattering. We can find the differential cross section by recalling equation 2.8. The incident electron flux $F_{incident} = \dot{N}_{incident}/Area$ can be found by finding the number of electrons that passes through a cross-sectional area $Area$ per unit time². The number of electrons that passes through $Area$ per unit time would be the same as electrons in an imaginary volume defined by $Area \times \frac{p_i}{m} dt$. For simplicity, we only concern ourselves with one electron to find the incident electron flux per electron³

$$F_{incident} = \frac{\dot{N}_{incident}}{Area} = \frac{1 \times Area \times \frac{p_i}{m} dt}{Area dt} = \frac{p_i}{m}. \quad (2.9)$$

²This is the same $Area$ that was used section 2.1.

³This is the equivalent of saying we define the density of electrons as 1 electron per unit volume.

We concern ourselves with what happens immediately before and after the collision in the electromagnetic field. We describe the field by its vector potential in the dipole approximation:

$$\mathbf{A} = \mathbf{a} \cos(\omega t) \quad (2.10)$$

where \mathbf{a} is the vector potential amplitude and has the phase

$$\alpha = \omega t. \quad (2.11)$$

We consider the collision to be instantaneous and therefore at a specific phase. Since the phase is only present in the cosine function in equation 2.10, we only concern ourselves in the phase range $0 \leq \alpha \leq \pi$. Then a normalized phase interval is $\frac{d\alpha}{\pi}$. We can find an expression for the free-free differential cross section by using equation 2.8 and 2.9.

$$\frac{d\sigma_{FF}}{d\Omega} = \frac{\dot{N}_{scattered}(\text{into } d\Omega)/N_{target}/d\Omega}{p_i/m} \frac{d\alpha}{\pi}. \quad (2.12)$$

The numerator can be found using equation 2.5 and 2.9 for elastic-scattering.

$$\dot{N}_{scattered}(\text{into } d\Omega)/N_{target}/d\Omega = \frac{p_\alpha}{m} \frac{d\sigma_{el}}{d\Omega}. \quad (2.13)$$

Substituting equation 2.13 into 2.12 results in

$$\frac{d\sigma_{FF}}{d\Omega_\beta} = \frac{p_\alpha}{p_i} \frac{d\sigma_{el}}{d\Omega} \frac{d\alpha}{\pi} \quad (2.14)$$

where $d\Omega_\beta$ is used to explicitly show this is the solid angle that momentum \mathbf{p}_β is directed towards. This expression is not sufficient since momentum p_β is not an observable quantity. To continue, we look for the relationship between $d\Omega_\beta$ and $d\Omega_f$ where $d\Omega_f$ is the solid angle that momentum \mathbf{p}_f is directed towards.

We begin by multiplying both sides by $d\alpha$. The quantity $d\alpha d\Omega_\beta$ can be represented in the spherical coordinate system as

$$d\alpha d\Omega_\beta = d\alpha \delta(p_\beta - p_\alpha) \frac{d^3 p_\beta}{p_\beta^2} \quad (2.15)$$

where $d^3 p_\beta$ is the volume element in p_β -space and δ is the Dirac delta function. The momentum of the electron will change due to the field by an amount $-e\mathbf{A}$ ⁴. Then the instantaneous momenta and the asymptotic, time-averaged momenta are related by

$$\begin{aligned} \mathbf{p}_\alpha &= \mathbf{p}_i - e\mathbf{A} \\ \mathbf{p}_\beta &= \mathbf{p}_f - e\mathbf{A}. \end{aligned} \quad (2.16)$$

The argument in the Dirac delta function in equation 2.15 can be converted from $\delta(p_\beta - p_\alpha)$ to $\delta(p_\beta^2 - p_\alpha^2)$ by using the following relationship[52]:

⁴The elementary charged e is positive, i.e. $e = |e|$.

$$\delta[(x-a)(x-b)] = \frac{1}{|a-b|} [\delta(x-a) + \delta(x-b)], a \neq b. \quad (2.17)$$

Then we have the relationship

$$\begin{aligned} \delta(p_\beta^2 - p_\alpha^2) &= \delta((p_\beta - p_\alpha)(p_\beta + p_\alpha)) \\ &= \frac{1}{2p_\beta} [\delta(p_\beta - p_\alpha) + \delta(p_\beta + p_\alpha)] \\ &= \frac{1}{2p_\beta} \delta(p_\beta - p_\alpha) \\ \delta(p_\beta - p_\alpha) &= 2p_\beta \delta(p_\beta^2 - p_\alpha^2) \end{aligned} \quad (2.18)$$

where the term $\delta(p_\beta + p_\alpha)$ was removed since it is not physically realizable in the spherical coordinate system.

We find an expression for $p_\beta^2 - p_\alpha^2$ by using equations 2.16

$$p_\beta^2 - p_\alpha^2 = p_f^2 - p_i^2 - 2e\mathbf{Q} \cdot \mathbf{a} \cos(\alpha). \quad (2.19)$$

where $\mathbf{Q} = \mathbf{p}_f - \mathbf{p}_i$ is the momentum transfer.

By substitution equation 2.18 and 2.19 into equation 2.15 and changing the coordinate system from p_β -space to p_f -space (replacing d^3p_β with d^3p_f), we obtain the following:

$$\begin{aligned} d\alpha' d\Omega_\beta &= \frac{2}{p_\beta} d\alpha' \delta(p_\beta^2 - p_\alpha^2) d^3p_\beta \\ &= \frac{2}{p_\beta} d^3p_f \delta(p_f^2 - p_i^2 - 2e(\mathbf{Q} \cdot \mathbf{a}) \cos(\alpha')) d\alpha' \\ &= \frac{2}{p_\beta} p_f^2 dp_f d\Omega_f \delta(p_f^2 - p_i^2 - 2e(\mathbf{Q} \cdot \mathbf{a}) \cos(\alpha')) d\alpha' \\ &= \frac{p_f}{p_\beta} dp_f^2 d\Omega_f \delta(p_f^2 - p_i^2 - 2e(\mathbf{Q} \cdot \mathbf{a}) \cos(\alpha')) d\alpha' \end{aligned} \quad (2.20)$$

where the last step used the relationship $dp^2 = 2p dp$. To continue the derivation, we use another Dirac delta function relationship[52]:

$$\delta[f(x)] = \sum_i \frac{\delta(x - x_i)}{|f'(x_i)|}, \text{ if } f(x_i) = 0 \text{ and } f'(x_i) \neq 0, \quad (2.21)$$

which we can use to evaluate the delta function

$$\begin{aligned} \delta(p_f^2 - p_i^2 - 2e(\mathbf{Q} \cdot \mathbf{a}) \cos(\alpha')) d\alpha' &= \sum \frac{\delta(\alpha' - \alpha) d\alpha'}{|2e(\mathbf{Q} \cdot \mathbf{a}) \sin(\alpha')|} \\ &\rightarrow \frac{1}{|2e(\mathbf{Q} \cdot \mathbf{a}) \sin(\alpha)|}. \end{aligned} \quad (2.22)$$

We find the classical free-free cross section by substituting equation 2.20 with 2.22 into equation 2.14 to obtain

$$\boxed{\frac{d\sigma_{FF}}{d\Omega_f} = \frac{p_f}{p_i} \frac{d\sigma_{el}}{d\Omega} \frac{dp_f^2}{|2\pi e(\mathbf{Q} \cdot \mathbf{a}) \sin(\alpha)|}}. \quad (2.23)$$

Recall that $p_\alpha = p_\beta$ (see delta function in equation 2.15).

We can find the change in kinetic energy of the electron by using equation 2.19 and recognizing $p_\alpha^2 - p_\beta^2 = 0$

$$\Delta E = \frac{(\mathbf{p}_f^2 - \mathbf{p}_i^2)}{2m} = \frac{e}{m}(\mathbf{Q} \cdot \mathbf{a}) \cos(\alpha) \quad (2.24)$$

The maximum value of equation 2.24 is when $\cos(\alpha) = 1$.

$$\boxed{E_{classical\ limit} = \frac{e}{m}(\mathbf{Q} \cdot \mathbf{a})} \quad (2.25)$$

is the classical limit of the energy transferred between the field and the electron.

2.3 Quantum Scattering Theory

To continue our discussion on electron-atom scattering, we now discuss quantum scattering theory.

Bransden & Joachain define cross sections as “the ratio of the number of events of this type per unit time and per unit scatterer, to the flux of the incident particles with respect to the target” [53]. Recall that cross sections are only dependent on the interactions between projectile and target for a given energy. So, we are free to choose the incident flux⁵. If the incident flux is set to unity, then cross sections can be interpreted as *transition probabilities per unit time (transition rate), per unit target scatterer and per unit flux of the incident particles with respect to the target* [53].

The following derivation to the cross section from the transition rate is from the text *Modern Quantum Mechanics* by J. J. Sakurai [54]. The transition rate for quantum scattering theory is given by

$$w(i \rightarrow f) = \frac{2\pi}{\hbar} |T_{fi}|^2 \delta(E_f - E_i) \quad (2.26)$$

where T_{fi} is the *T matrix* or the *transition matrix*⁶. Equation 2.26 assumes it is integrated over energy with the density of final states. Doing so gives the form

$$w(i \rightarrow f) = \frac{mk_f(2\pi)^3}{(2\pi)^2\hbar^3} |T_{fi}|^2 d\Omega \quad (2.27)$$

⁵We took advantage of this earlier when we defined $F_{incident}$ by setting the density of electrons to be 1 electron per unit volume.

⁶Equation 2.26 is very similar to Fermi’s golden rule except it uses the more general T matrix.

which is the transition rate for scattered particles in the solid angle $d\Omega$. m and k_f are the mass and final wavenumber of the scattered particle, respectively. Equation 2.27 assumes the wave functions were normalized to a delta function. To find the differential cross section, we divide equation 2.27 by the incident flux equation in terms of wavenumber

$$F_{incident} = \frac{p_i}{m(2\pi)^3} = \frac{\hbar k_i}{m(2\pi)^3} \quad (2.28)$$

where the density of incident electrons is taken to be 1 electron in a volume of $(2\pi)^3$. Then the differential cross section is

$$\frac{d\sigma}{d\Omega} = \frac{k_f}{k_i} \left(\frac{m(2\pi)^3}{(2\pi)\hbar^2} \right)^2 |T_{fi}|^2. \quad (2.29)$$

If we find the T matrix for free-free transitions, then we can find the quantum free-free differential cross section. To find the T matrix, we look at the relationship between the S and the T matrix

$$S_{fi} = \delta_{fi} - i2\pi\delta(E_f - E_i)T_{ni} \quad (2.30)$$

and compare with the S matrix for free-free scattering[55]

$$S_{fi} = \delta_{fi} - \frac{i}{\hbar} \int_{-\infty}^{+\infty} \langle X_f(\mathbf{r}, t') | V(\mathbf{r}) | \Psi_i(\mathbf{r}, t') \rangle dt' \quad (2.31)$$

where $X(\mathbf{r}, t)$ is the wave function for an electron coupled with an external electromagnetic field and $\Psi(\mathbf{r}, t)$ is the wave function for an electron in the presence of a scattering potential $V(\mathbf{r})$ and coupled to an external electromagnetic field. To continue, we must find $X(\mathbf{r}, t)$.

2.3.1 Volkov Wavefunction

To find the wave function of an electron coupled with an external electromagnetic field, we solve the time-dependent Schrödinger equation. In the dipole approximation, the laser field can be described by the vector potential $\mathbf{A}(t)$. Then the Hamiltonian of an electron coupled to an external electromagnetic field is

$$H_{e-laser} = \frac{1}{2m} [\hat{\mathbf{p}} - e\mathbf{A}(t)]^2 \quad (2.32)$$

where m is the electron mass, $e = |e|$ is the elementary charge, and $\hat{\mathbf{p}}$ is the momentum operator. Then the time-dependent Schrödinger equation for the state wave function $X(\mathbf{r}, t)$ is

$$i\hbar \frac{\partial}{\partial t} X(\mathbf{r}, t) = \frac{1}{2m} [\hat{\mathbf{p}} - e\mathbf{A}(t)]^2 X(\mathbf{r}, t). \quad (2.33)$$

The solution to equation 2.33 can be found in atomic physics textbooks such as the one by B. H. Bransden & C. J. Joachain[53]. The wave function that solves the time-dependent Schrödinger equation is

$$X(\mathbf{r}, t) = \frac{1}{(2\pi)^{3/2}} \exp \left\{ i \frac{\mathbf{p}}{\hbar} \cdot \left(\mathbf{r} + \frac{e}{m} \int^t \mathbf{A}(t') dt' \right) - i \frac{E}{\hbar} t - i \frac{e^2}{2m\hbar} \int^t \mathbf{A}^2(t') dt' \right\} \quad (2.34)$$

and is known as the Volkov wave function. E is the kinetic energy of the free electron. Note that \mathbf{p} is the eigenvalue of the momentum operator $\hat{\mathbf{p}}$.

Equation 2.34 is the general form of the Volkov wave function. To proceed, we use equation 2.10 to obtain

$$X(\mathbf{r}, t) = \frac{1}{(2\pi)^{3/2}} \exp \left\{ -i \frac{E + \frac{e^2 a^2}{4m}}{\hbar} t + i \frac{\mathbf{p}}{\hbar} \cdot \left(\mathbf{r} + \frac{e\mathbf{a}}{m\omega} \sin(\omega t) \right) - i \frac{e^2 \mathbf{a}^2}{8m\hbar\omega} \sin(2\omega t) \right\} \quad (2.35)$$

This is the form of the wave function we will use to describe the electron in a laser field.

2.4 Kroll Watson Approximation

In this section, we derive the Kroll Watson Approximation (KWA), a widely used model for free-free processes that we touched upon in chapter 1. The model is considered semiclassical since quantum scattering theory is used but the electromagnetic field is treated classically. We follow a similar derivation as shown by Kroll and Watson[12] and Rahman[55]. We return to equation 2.31 and use equation 2.35,

$$S_{fi} = \delta_{fi} - \frac{i}{\hbar} \int_{-\infty}^{+\infty} \langle X_f(\mathbf{r}, t) | V(\mathbf{r}) | \Psi_i(\mathbf{r}, t) \rangle dt' \quad (2.36)$$

Let us evaluate the time integral by assuming that the scattering potential is weak to employ the first Born approximation[56] to obtain

$$\frac{i}{\hbar} \int_{-\infty}^{+\infty} \langle X_f(\mathbf{r}, t) | V(\mathbf{r}) | X_i(\mathbf{r}, t) \rangle dt'. \quad (2.37)$$

We evaluate the matrix element and integrate to obtain

$$\begin{aligned} \int_{-\infty}^{+\infty} \langle X_f(\mathbf{r}, t) | V(\mathbf{r}) | X_i(\mathbf{r}, t) \rangle dt' &= \frac{1}{(2\pi)^3} \frac{i}{\hbar} \int_{-\infty}^{+\infty} e^{i(E_f - E_i)t'/\hbar} dt' \\ &\quad \times \int_{-\infty}^{+\infty} \exp \left\{ -i \frac{e}{m\hbar\omega} \mathbf{Q} \cdot \mathbf{a} \sin(\omega t) \right\} dt' \\ &\quad \times \int V(\mathbf{r}) e^{-i(\mathbf{Q} \cdot \mathbf{r})/\hbar} d^3 r' \end{aligned} \quad (2.38)$$

where we used the momentum transfer $\mathbf{Q} = \mathbf{p}_f - \mathbf{p}_i$. To continue, we use the following three relationships:

- *Jacobi-Anger Expansion*[57] which expands plane wave into cylindrical waves

$$\exp\{i\rho \cos(\varphi')\} = \sum_{n=-\infty}^{+\infty} i^n J_n(\rho) e^{in\varphi'} \quad (2.39)$$

where J_n is the n^{th} Bessel function of the first kind. For our use, we let $\varphi' = \varphi - \frac{\pi}{2}$ to obtain

$$\exp\{i\rho \sin(\varphi)\} = \sum_{n=-\infty}^{+\infty} J_n(\rho) e^{in\varphi}. \quad (2.40)$$

- *1st Born Approximation scattering amplitude*[54]

$$f_{\text{Born}}^{(1)} = -\frac{m}{2\pi\hbar^2} \int V(\mathbf{r}) e^{-i\mathbf{Q}\cdot\mathbf{r}/\hbar} d^3r' \quad (2.41)$$

- *Inverse Fourier transform of the δ function*[52]

$$2\pi\delta(x - \zeta) = \int_{-\infty}^{+\infty} e^{i\eta(x-\zeta)} d\eta \quad (2.42)$$

Using equation 2.40, 2.41, and 2.42 on equation 2.38, we obtain

$$\begin{aligned} & \frac{i}{\hbar} \int_{-\infty}^{+\infty} \langle X_f(\mathbf{r}, t) | V(\mathbf{r}) | X_i(\mathbf{r}, t) \rangle dt' \\ &= -\frac{1}{(2\pi)^3} \frac{i}{\hbar} \frac{2\pi\hbar^2}{m} \sum_{n=-\infty}^{+\infty} J_n\left(-\frac{e}{m\hbar\omega}(\mathbf{Q}\cdot\mathbf{a})\right) f_{\text{Born}}^{(1)} \int_{-\infty}^{+\infty} e^{i(E_f - E_i + n\hbar\omega)/\hbar} dt' \\ &= -2\pi \frac{1}{(2\pi)^3} \frac{i}{\hbar} \frac{2\pi\hbar^2}{m} \sum_{n=-\infty}^{+\infty} J_n\left(-\frac{e}{m\hbar\omega}(\mathbf{Q}\cdot\mathbf{a})\right) f_{\text{Born}}^{(1)} \delta((E_f - E_i + n\hbar\omega)/\hbar). \end{aligned} \quad (2.43)$$

We can now evaluate the S matrix using our result above for the n^{th} element.

$$S_{fi} = \delta_{fi} - i2\pi\delta(E_f - E_i + n\hbar\omega) \left[-\frac{1}{(2\pi)^3} \frac{2\pi\hbar^2}{m} J_n\left(-\frac{e}{m\hbar\omega}(\mathbf{Q}\cdot\mathbf{a})\right) f_{\text{Born}}^{(1)} \right]. \quad (2.44)$$

Comparing equation 2.44 with equation 2.30, we can see that the T_{fi} matrix is

$$T_{fi} = -\frac{1}{(2\pi)^3} \frac{2\pi\hbar^2}{m} J_n\left(-\frac{e}{m\hbar\omega}(\mathbf{Q}\cdot\mathbf{a})\right) f_{\text{Born}}^{(1)}. \quad (2.45)$$

By using our result of equation 2.45 in equation 2.29, we find the differential cross section for LAFF scattering for n photons:

$$\begin{aligned}\frac{d\sigma_{FF}^n}{d\Omega} &= \frac{k_f}{k_i} \left(\frac{m(2\pi)^3}{2\pi\hbar^2} \right)^2 \left| -\frac{1}{(2\pi)^3} \frac{2\pi\hbar^2}{m} J_n \left(-\frac{e}{m\hbar\omega} (\mathbf{Q} \cdot \mathbf{a}) \right) f_{Born}^{(1)} \right|^2 \\ &= \frac{k_f}{k_i} J_n^2 \left(-\frac{e}{m\hbar\omega} (\mathbf{Q} \cdot \mathbf{a}) \right) \frac{d\sigma_{Born}^{(1)}}{d\Omega}\end{aligned}\quad (2.46)$$

where $d\sigma_{Born}^{(1)}/d\Omega$ is the differential cross section for elastic electron scattering in the first Born approximation. If the first Born approximation is sufficient in describing the differential cross section for elastic-scattering, then we obtain the *Kroll Watson Approximation*

$$\boxed{\frac{d\sigma_{FF}^n}{d\Omega} = \frac{p_f}{p_i} J_n^2(x) \frac{d\sigma_{el}}{d\Omega}} \quad (2.47)$$

where

$$\boxed{x = -\frac{e}{m\hbar\omega} (\mathbf{Q} \cdot \mathbf{a})}. \quad (2.48)$$

Looking at the delta function in equation 2.44, $n > 0$ refers to photon emission and $n < 0$ to photon absorption by the electron⁷. Then the kinetic energy of the electron after n photons free-free scattering is

$$E_f = E_i - n\hbar\omega \quad (2.49)$$

Kroll and Watson showed that if the first Born approximation is insufficient in describing the scattering cross section, then the KWA will still holds provided that the frequency is low and if the photon energy transfer is less than the classical limit. To find the classical limit, let us compare the the argument of KWA (equation 2.48) with the classical maximum change in kinetic energy of the electron (equation 2.24).

$$|x| = \left| -\frac{e}{m\hbar\omega} (\mathbf{Q} \cdot \mathbf{a}) \right| = \frac{E_{classical\ limit}}{\hbar\omega} \quad (2.50)$$

where it can be seen that x is the classical limit on the number of photons that can be transferred in free-free scattering.

Let us now compare the KWA with the classical cross section. We look at the Debye asymptotic formula for Bessel functions (the asymptotic limit for $n \sim x$)[12, 58]:

$$J_n^2 \approx \frac{2\cos^2[\sqrt{x^2 - n^2} - |v\cos^{-1}(\frac{n}{x})| - \frac{\pi}{4}]}{\pi\sqrt{x^2 - n^2}}, \text{ when } n < x \quad (2.51)$$

$$J_n^2 \approx \frac{2e^{-2\int_0^n \cosh^{-1}(\frac{n'}{|x|})dn'}}{\pi\sqrt{x^2 - n^2}}, \text{ when } n > x \quad (2.52)$$

⁷Photon absorption may also be referred to as *stimulated bremsstrahlung* and photon emission as *inverse bremsstrahlung*[12]

where n is the number of photons absorbed/emitted by the electron and x is the argument of the Bessel function in the KWA. Then equation 2.51 refer to the scenario when the energy transfer is less than what is classically allowed while equation 2.52 refer to the scenario when more energy is transferred than classically allowed.

We can relate the classical scattering phase α to the quantum parameters of KWA by the following relationship:

$$n = |x| \cos(\alpha). \quad (2.53)$$

Now, consider the case where the energy transfer is below the classical limit equation 2.51. Since the number of photons transferred is large, we can use the average value of \cos^2 , $\langle \cos^2 \rangle = \frac{1}{2}$. Using equation 2.47, 2.48, 2.51, 2.53, and $\langle \cos^2 \rangle = \frac{1}{2}$, we find that

$$\frac{d\sigma_{FF}}{d\Omega} \approx \frac{p_f}{p_i} \frac{d\sigma_{el}}{d\Omega} \frac{m\hbar\omega}{\pi e(\mathbf{Q} \cdot \mathbf{a}) \sin(\alpha)}. \quad (2.54)$$

When compared with the classical free-free differential cross section (equation 2.23), we find that

$$dp_f^2 = 2m\hbar\omega \rightarrow \frac{dp_f^2}{2m} = \hbar\omega \quad (2.55)$$

One can think of dp_f^2 as *bins* that correspond to “bins of energy” of $\hbar\omega$ [13].

2.4.1 Redefining x

The argument of the Bessel function in the KWA (equation 2.48) is not ideal for experimentalists since the vector potential \mathbf{A} is not a measurable quantity. All experiments discussed in this work used a laser to supply the electromagnetic field. Thus, it is more convenient to express x in terms of intensity I and wavelengths λ . It is also more convenient to use the kinetic energy of the incident electron E_i rather than its momenta p_i and p_f .

We start by recognizing that the direction of \mathbf{a} is also direction of polarization $\hat{\mathbf{e}}$ of the laser field.

$$x = -\frac{ea}{m\hbar\omega} p_i \left(\frac{\hat{\mathbf{e}} \cdot \mathbf{Q}}{p_i} \right) \quad (2.56)$$

where $(\hat{\mathbf{e}} \cdot \mathbf{Q})$ is normalized to the initial momenta p_i . Then the quantity $(\frac{\hat{\mathbf{e}} \cdot \mathbf{Q}}{p_i})$ can be determined by the scattering geometry of the experiment.

We use the following relationships:

- Electric field $\mathcal{E}(t)$ from the vector potential in the Coulomb gauge[59],

$$\mathcal{E}(t) = -\partial_t \mathbf{A} = \omega a \sin(\omega t) \hat{\mathbf{e}} = \mathcal{E}_0 \sin(\omega t) \hat{\mathbf{e}} \quad (2.57)$$

then

$$a = \frac{\mathcal{E}_0}{\omega} \quad (2.58)$$

where \mathcal{E}_0 is the magnitude of the electric field.

- Electric field and intensity of the field[60],

$$I = \frac{1}{2}c\epsilon_0|\mathcal{E}_0|^2 \rightarrow \mathcal{E}_0 = \left(\frac{2I}{c\epsilon_0}\right)^{1/2} \quad (2.59)$$

where ϵ_0 is the permittivity of free-space and c is the speed of light in vacuum.

- The angular frequency ω with wavelength λ ,

$$\omega = \frac{2\pi c}{\lambda} \quad (2.60)$$

- Incident electron momentum and energy

$$E_i = \frac{p_i^2}{2m} \rightarrow p_i = (2mE_i)^{1/2} \quad (2.61)$$

Substituting equation 2.58, 2.59, 2.60, (2.61) into equation 2.48 we obtain

$$x = - \left(\frac{4e^2}{(2\pi)^4 m \hbar^2 c^5 \epsilon_0} \right)^{1/2} \lambda[\text{m}]^2 I \left[\frac{\text{W}}{\text{m}^2} \right]^{1/2} E_i[\text{J}]^{1/2} \left(\frac{\hat{\epsilon} \cdot \mathbf{Q}}{p_i} \right) \quad (2.62)$$

in the SI unit system. However, in our experiments, SI units are not convenient. We make a unit conversation to have the wavelength λ , intensity I , and incident electron energy E_i in $[\mu\text{m}]$, $[\frac{\text{GW}}{\text{cm}^2}]$, and $[\text{eV}]$, respectively. Doing the unit conversions, we obtain

$$\begin{aligned} x &= - \left(\frac{e^3 \times 10^{-11}}{4\pi^4 m \hbar^2 c^5 \epsilon_0} \right)^{1/2} \lambda[\mu\text{m}]^2 I \left[\frac{\text{GW}}{\text{cm}^2} \right]^{1/2} E_i[\text{eV}]^{1/2} \left(\frac{\hat{\epsilon} \cdot \mathbf{Q}}{p_i} \right) \\ &\approx -0.0220 \lambda[\mu\text{m}]^2 I \left[\frac{\text{GW}}{\text{cm}^2} \right]^{1/2} E_i[\text{eV}]^{1/2} \left(\frac{\hat{\epsilon} \cdot \mathbf{Q}}{p_i} \right). \end{aligned} \quad (2.63)$$

Now we have a form of KWA that is convenient for our experiments:

$$\boxed{\frac{d\sigma_{FF}}{d\Omega} = \frac{p_f}{p_i} J_n^2(x) \frac{d\sigma_{el}}{d\Omega}} \quad (2.64)$$

where

$$\boxed{x = -0.0220 \lambda^2 I^{1/2} E_i^{1/2} \left(\frac{\hat{\epsilon} \cdot \mathbf{Q}}{p_i} \right)} \quad (2.65)$$

where the wavelength of the field λ in μm , intensity of the laser at the collision I in GW/cm^2 , and the incident electron energy E_i in eV. In our work, the electrons have an incident energy of 350 eV. For elastic scattering, $p_i \approx p_f$. In free-free scattering, there are three interactions: laser-electron, electron-atom, and laser-atom. The laser-electron interaction is contained in the Bessel function and the electron-atom interaction is contained in the elastic differential cross section. The main assumption of KWA is that the laser-atom interaction is negligible. The purpose of the atom is to allow the simultaneous conservation of energy and momentum during the free-free transition.

2.4.2 Relative Cross Sections

In our laboratory, the exact geometric efficiency is not known. Thus, we are unable to directly measure absolute free-free cross sections. What is measured in our experiments is the ratio of the laser-on signal to the laser-off signal. To within a geometric overlap factor (the overlap between the laser, electron, and helium beam), this quantity is related to the ratio of the free-free cross section to the field-free cross section

$$\boxed{\frac{d\sigma_{FF}}{d\Omega} \bigg/ \frac{d\sigma_{el}}{d\Omega} = \frac{p_f}{p_i} J_n^2(x)}, \quad (2.66)$$

where the argument x is the same as equation 2.65. Note that on the RHS, there is no dependence on the target. The advantage of relative cross sections can be seen by looking at the definition of differential cross sections (equation 2.8). In an experiment, N_{target} , $d\Omega$, and $F_{incident}$ can be kept constant. Thus, the relative cross section is

$$\frac{d\sigma_{FF}}{d\Omega} \bigg/ \frac{d\sigma_{el}}{d\Omega} = \frac{\dot{N}_{FF}}{\dot{N}_{el}} \quad (2.67)$$

where \dot{N}_{FF} and \dot{N}_{el} refer to the scattering rate of free-free and elastically-scattered electron measured by the detector, respectively. The relative cross section is simply the ratio of their rates.

For inelastic free-free processes, Geltman and Maquet performed an *ansatz* and extended the KWA to inelastic scattering processes. They replaced the elastic cross section in equation 2.64 with the inelastic cross section[42]. They found good qualitative agreement with the experimental results of Mason and Newell[61] and Wallbank *et al.*[41].

As discussed section 1.1, many experiments were performed to test the validity of the KWA in both elastic and inelastic free-free processes. Experimental results have shown disagreements with the KWA, especially in regions where vanishing cross sections are expected[25, 29]. Multiple scattering may be a potential explanation for this deviation[34].

The limits of validity of the KWA are still of interest. This thesis is an experimental examination of the KWA angular distributions in helium for both elastic and

inelastic processes. Figure 2.2 shows predicted KWA angular distributions appropriate to the experiments described in this thesis (see table 2.1). For inelastic scattering, an electron energy loss of 21.22 eV (the energy necessary to excite a ground state helium to its 2^1P excited state) was accounted for when calculating the final momentum of the electron.

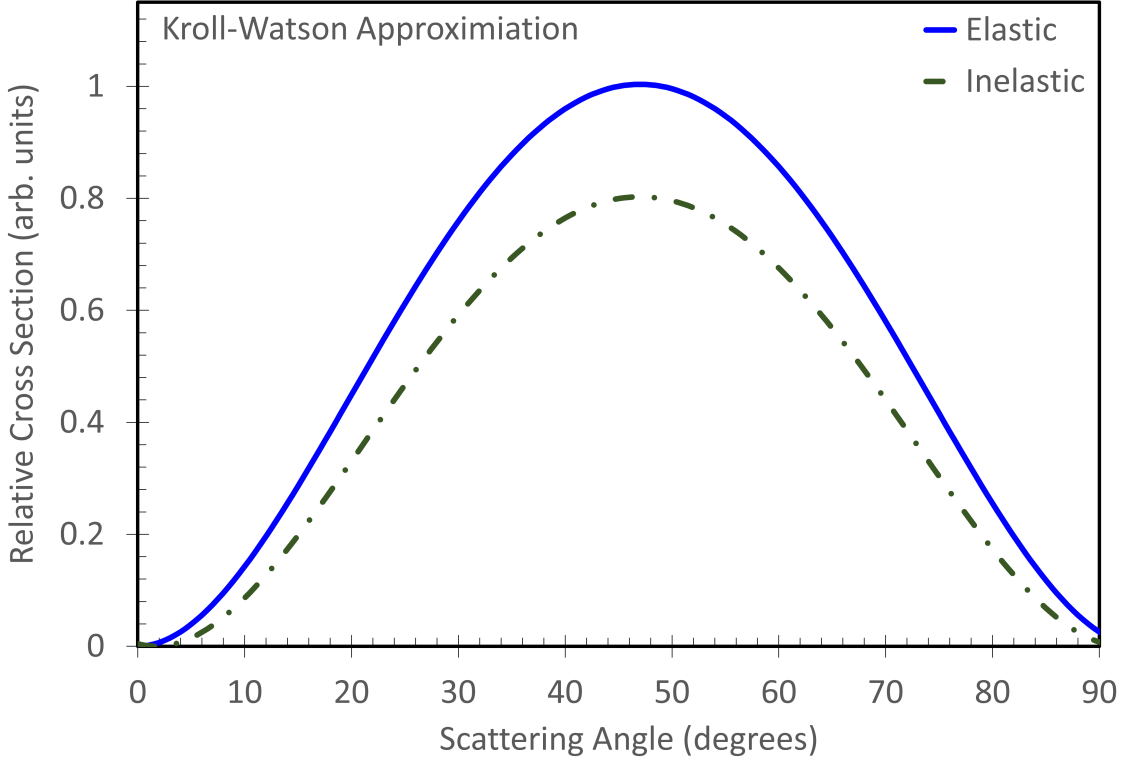


Figure 2.2: Angular distributions for one photon processes ($n = \pm 1$) calculated with the Kroll-Watson approximation for elastic (blue solid-line) and inelastic (green chained-line) scattering using values shown in table 2.1. Both curves were normalized to the 45° elastic calculation.

Wavelength λ	1.064 μm
Intensity I	11.3 GW/cm^2
Incident Electron Energy E_i	350 eV
Polarization $\hat{\epsilon}$	-133°

Table 2.1: Values of the parameters used in the argument of KWA (see equation 2.65). The intensity used the nominal output power of the PowerLite Nd:YAG laser with the measured beam size at the interaction region.

2.5 Light-Dressing Effects

In equation 2.66, the KWA predicts that the properties of the target atom does not affect the free-free relative cross section. The model assumes that the laser-atom interaction is negligible. However, if the electric field of the laser is strong, the target atom can be distorted introducing so-called *light-dressing effects*[62, 4].

We now discuss a model by Zon for free-free processes that does not neglect the laser-atom interaction. The model uses perturbation theory in the context of bremsstrahlung for S-state atoms[38]. He used the scattering potential

$$V(\mathbf{r}, t) = \frac{1}{4\pi\epsilon_0} \left[-\frac{Ze^2}{r} + e^2 \sum_{j=1}^Z \frac{1}{|\mathbf{r} - \mathbf{r}_j|} + \frac{e\alpha(\omega)}{r^3} (\boldsymbol{\mathcal{E}}_0 \cdot \mathbf{r}) \cos(\omega t) \right] \quad (2.68)$$

where Z is the nuclear charge, \mathbf{r}_j is the position of the j^{th} electron of the atom, and $\alpha(\omega)$ is the dynamic dipole polarizability of the atom. The first two terms refer to the scattering potential of the atomic target. The last term refers to the scattering potential due to the external electric field polarizing the atom. Using the first Born approximation, we obtain the differential cross section

$$\frac{d\sigma_{ZON}}{d\Omega} = \frac{p_f}{p_i} \left| J_n(x) \frac{1}{2\pi\epsilon_0} \frac{mZe^2}{\mathbf{Q}^2} [1 - F_f(\mathbf{Q})] - \frac{1}{4\pi\epsilon_0} \frac{\alpha(\omega)m^2\omega^2x}{\mathbf{Q}^2} [J_{n-1}(x) - J_{n+1}(x)] \right|^2 \quad (2.69)$$

where $F_f(\mathbf{Q})$ is the *form factor* for the excitation from the ground state $|0\rangle$ to some final state $|f\rangle$.

The relationship between the differential cross section and the form factor is given by Sakurai [54]:

$$\frac{d\sigma}{d\Omega} = \frac{p_f}{p_i} \left(\frac{mZe^2}{2\pi\epsilon_0\mathbf{Q}^2} \right)^2 |\delta_{f0} - F_f(\mathbf{Q})|^2 \quad (2.70)$$

that corresponds to the the scattering amplitude

$$f_{f0} = \pm \left(\frac{mZe^2}{2\pi\epsilon_0\mathbf{Q}^2} \right) [\delta_{f0} - F_f(\mathbf{Q})] \quad (2.71)$$

where δ_{f0} is the Kronecker delta function between some final state $|f\rangle$ and the ground state $|0\rangle$. For elastic scattering,

$$f_{00} = f_{el} = \pm \left(\frac{mZe^2}{2\pi\epsilon_0\mathbf{Q}^2} \right) [1 - F_f(\mathbf{Q})]. \quad (2.72)$$

Using equation 2.69 and 2.72, we obtain the following

$$\frac{d\sigma_{ZON}}{d\Omega} = \frac{p_f}{p_i} \left| \underbrace{J_n(x)f_{el}}_{\text{KWA Term}} - \underbrace{\alpha(\omega) \frac{1}{4\pi\epsilon_0} \frac{2m^2\omega^2x}{\mathbf{Q}^2} J'_n(x)}_{\text{Light-Dressing Term}} \right|^2 \quad (2.73)$$

where we used the derivative of the Bessel function of the first kind

$$J'_n(x) = \frac{1}{2}[J_{n+1}(x) - J_{n-1}(x)] \quad (2.74)$$

[52]. The Bessel function argument x is the same as in the KWA (equation 2.65). We note that if the second term is ignored, we obtain the KWA. So, we call the first term the *KWA term* and the second term the *light-dressing term*. We note that angular frequency ω of a 1.17 eV laser field is much less than the atomic unit for angular frequency. Thus, we can replace the dynamic dipole polarizability with the static dipole polarizability α . The appeal of the Zon model is that the laser-atom interaction depends only on the electric dipole polarizability α of the atom.

To compare with the KWA (equation 2.66), we divide both sides of Zon by the elastic differential cross section to obtain the relative cross section

$$\boxed{\frac{d\sigma_{ZON}}{d\Omega} \bigg/ \frac{d\sigma_{el}}{d\Omega} = \frac{p_f}{p_i} \left| J_n(x) - \alpha \frac{1}{4\pi\epsilon_0} \frac{2m^2\omega^2 x}{\mathbf{Q}^2} \frac{J'_n(x)}{f_{el}} \right|^2}. \quad (2.75)$$

To see light-dressing effects, we require that $\left| \alpha \frac{1}{4\pi\epsilon_0} \frac{2m^2\omega^2 x}{\mathbf{Q}^2} \frac{J'_n(x)}{f_{el}} \right| \sim |J_n(x)|$. We note that the light-dressing term increases by a factor of $1/\mathbf{Q}$ (recall that x has a factor of \mathbf{Q}). Thus, we expect to see light-dressing effects if α is large and the scattering angle θ_{scatt} is small.

Figure 2.3 shows equation 2.75 plotted for various static dipole polarizabilities shown in table 2.2⁸ along with the KWA using the values on table 2.1. Figure 2.4 has the same curves as figure 2.3 but for low scattering angles.

Atomic Target	α [Atomic Units]
Helium	1.38
Argon	11.1
Xenon	27.3
Potassium	290

Table 2.2: Various static dipole polarizabilities used to plot the Zon model in figure 2.3. He, Ar, Xe, and K are in their ground states. The dipole polarizabilities came from [63].

⁸These four dipole polarizabilities were chosen since He was used in this work, Ar was the atomic target used in previous works[14], Xe was the atomic target used by Morimoto *et al.* where light-dressing effects were observed[4], and K was a target that was considered but rejected for experimental reasons (see text).

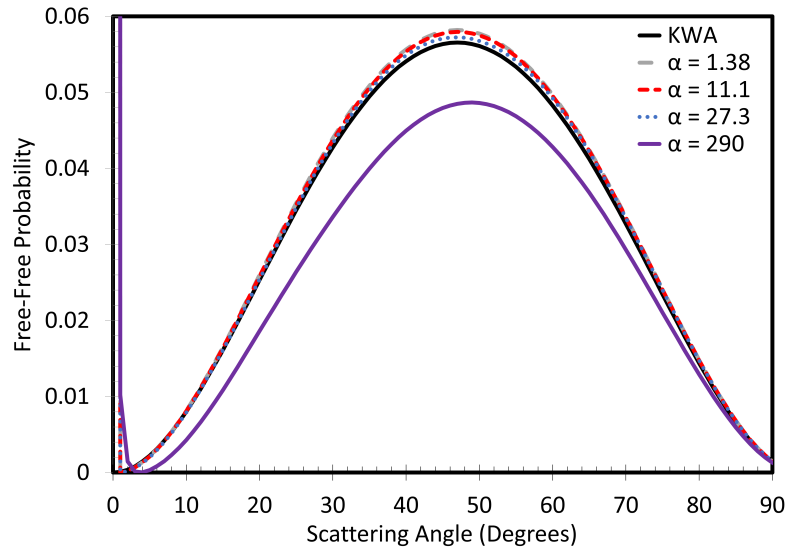


Figure 2.3: The Zon model for various static dipole polarizabilities (see table 2.2). The KWA is also plotted for comparison. Scattering amplitudes are from NIST database[64].

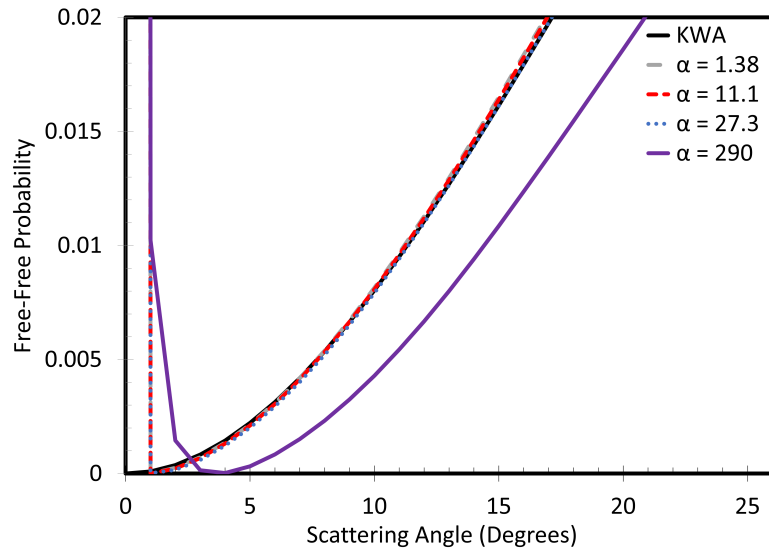


Figure 2.4: The same plot as figure 2.3 for small scattering angles. Cross section data from [64].

Figures 2.3 and 2.4 show that deviations from KWA can be seen at low scattering angles for all targets. However, these deviations occur at scattering angles below 1° . Due to potassium having a relatively large dipole polarizability, it is the only target of the four where deviations from KWA can be seen at higher scattering angles. It is interesting to note that a local minimum can be seen around 4° , which is readily accessible with our apparatus. Unfortunately, exploratory free-free experiments of potassium showed this is not experimentally feasible since an intense potassium beam is required to see a free-free signal. This quickly blocked up the exit aperture of the electron gun requiring frequent cleaning. This makes potassium an unsuitable atomic target for a free-free angular distribution[62].

It was noted that the $(1s2s)^1S$ excited state of helium has a static dipole polarizability of 730 ± 90 a.u.[65]. It was assumed that the Zon model may be applicable to inelastic free-free processes. Preliminary calculations using the cross section data from Fursa and Bray[66] for electron-impact excitation for helium from the ground state to the 2^1S excited state for 500 eV electrons showed unreasonably large relative free-free cross sections. Unfortunately, the Zon model does not appear to work for inelastic scattering. An inelastic free-free scattering model is needed to determine if light-dressed atom effects are expected for inelastic LAFF scattering of helium.

2.5.1 In-House Inelastic Light-Dressed Model

[Hartree atomic units will be used for this subsection.]

Here we present a *qualitative* model developed by Martin (my thesis advisor)[67] for inelastic free-free scattering. The model was developed by considering the Stark mixing of excited states under the influence of an external electromagnetic field. We start by finding the inelastic scattering amplitude for electron-helium scattering in an external electromagnetic field that is linearly polarized as done by Akramine *et al.*[68, 69]. The laser-electron interaction is treated similarly as in section 2.3.1 but in the velocity gauge. The velocity gauge transformation for a wave function $\Psi(\mathbf{r}, t)$ for an atom with N electrons is

$$\Psi(\mathbf{r}, t) = e^{-i\frac{N}{2} \int^t \mathbf{A}^2(t') dt'} \Psi^V(\mathbf{r}, t) \quad (2.76)$$

where Ψ^V is the wave function in the velocity gauge. For a free electron ($N = 1$), we have the Volkov wave function in the velocity gauge:

$$X^V(\mathbf{r}, t) = \frac{1}{(2\pi)^{3/2}} e^{i(\mathbf{k}\cdot\mathbf{r} - Et - \frac{\mathbf{k}\cdot\mathbf{E}_0}{\omega^2} \sin(\omega t))} \quad (2.77)$$

where \mathbf{k} is the wave vector. Since we are not ignoring the laser-atom interaction, we need to find the *dressed* wave function $\Phi(\mathbf{r}, t)$ for helium in an external electromagnetic field. The Hamiltonian for an atom in an external field in the dipole approximation and velocity gauge is

$$H = H_0 + H_{laser-atom} = H_0 - i \sum_{j=1}^2 \mathbf{A}(t) \cdot \nabla_j \quad (2.78)$$

where H_0 is the Hamiltonian for the helium atom when it is not in an external field. Since the magnitude of the electric field is much less than the atomic unit of electric field strength, time-dependent perturbation theory is appropriate.

The Schrödinger equation for this process is

$$i\partial_t \Phi_m(\mathbf{r}, t) = [H_0 + H_{laser-atom}] \Phi_m(\mathbf{r}, t) \quad (2.79)$$

where

$$\begin{aligned} \Phi_m(\mathbf{r}, t) = & e^{-i\mathbf{A}\cdot\mathbf{R}} e^{iE_m t} \\ & \times \left[\psi_m(\mathbf{r}) + \frac{i}{2} \sum_{m'} M_{m'm} \left(\frac{e^{i\omega t}}{E_{m'} - E_m + \omega} - \frac{e^{-i\omega t}}{E_{m'} - E_m - \omega} \right) \psi_{m'}(\mathbf{r}) \right] \end{aligned} \quad (2.80)$$

where the factor $e^{-i\mathbf{A}\cdot\mathbf{R}}$ is included to ensure gauge consistency between the Volkov wave function (see equation 2.77) and $\Phi_m(\mathbf{r}, t)$ ⁹. ψ_m are the eigenstates of H_0 with a

⁹Khalil *et al.* used the laser-atom interaction Hamiltonian in the velocity gauge and solved for $\Phi_m(\mathbf{r}, t)$ using the length gauge.

corresponding energy E_m and \mathbf{R} is the vector sum of the coordinates of the electrons, i.e. $\mathbf{R} = \mathbf{r}_1 + \mathbf{r}_2$ for helium. $M_{m'm}$ is the dipole coupling matrix elements defined as

$$M_{m'm} = \mathcal{E}_0 \langle \psi_{m'} | \hat{\boldsymbol{\epsilon}} \cdot \mathbf{R} | \psi_m \rangle \quad (2.81)$$

where $\hat{\boldsymbol{\epsilon}}$ is the direction of polarization. The sum in equation 2.80 is over all discrete states and integrated over the continuum states. We now write the S matrix elements in the first Born approximation for the inelastic collision:

$$S_{fi} = -i \int_{-\infty}^{+\infty} \langle X_f^V(\mathbf{r}, t) \Phi_f(\mathbf{r}, t) | V_d(\mathbf{r}, t) | X_i^V(\mathbf{r}, t) \Phi_i(\mathbf{r}, t) \rangle dt' \quad (2.82)$$

where

$$V_d(\mathbf{r}, t) = -\frac{2}{r} - \sum_j^2 \frac{1}{r_j} \quad (2.83)$$

and r_j is the position of the j^{th} electron. Note that in equation 2.82 we use the product of the Volkov and the dressed helium wave function since we are now concerned with the initial and final electron as well as the initial and final state of the target helium[54]. Then the S matrix of the n photon process is

$$S_{fi} = \delta(E_f - E_i + \Delta E - n\omega) f_{Born}^{(1)} \quad (2.84)$$

where ΔE is the energy difference between the excited and ground state. $f_{Born}^{(1)}$ is the first Born approximation inelastic free-free scattering amplitude.

The scattering amplitude $f_{Born}^{(1)}$ is comprised of two parts: the scattering amplitude due to laser-electron interaction $f_{laser-electron}$ and the the laser-atom interaction $f_{laser-atom}$.

$$f_{Born}^{(1)} = f_{laser-electron} + f_{laser-atom} \quad (2.85)$$

where

$$f_{laser-electron} = J_n(x) f_{f0}^{(1)} \quad (2.86)$$

$$\begin{aligned} f_{laser-atom} = & + \frac{i}{2} \sum_m \left[\frac{J_{n+1}(x)}{E_m - E_i + \omega} - \frac{J_{n-1}(x)}{E_m - E_i - \omega} \right] M_{mi} f_{fm}^{(1)} \\ & - \frac{i}{2} \sum_m \left[\frac{J_{n-1}(x)}{E_m - E_f + \omega} - \frac{J_{n+1}(x)}{E_m - E_f - \omega} \right] M_{fm} f_{mi}^{(1)} \end{aligned} \quad (2.87)$$

where

$$\begin{aligned} f_{f0}^{(1)} & \text{ is the scattering amplitude for } 0 \rightarrow f, \text{ and} \\ f_{fm}^{(1)} & \text{ is the scattering amplitude for } m \rightarrow f, \text{ and} \\ f_{m0}^{(1)} & \text{ is the scattering amplitude for } 0 \rightarrow m \end{aligned} \quad (2.88)$$

in the first Born approximation. The subscripts 0, m , and f refers to the ground state, intermediate state, and the final state, respectively. This is the result found by Akramine *et al.*[69]. If the laser-atom interaction is negligible, then we obtain the scattering amplitude for the KWA.

The first term of equation 2.87 corresponds to light-dressing of the ground state. Since the first excited state of helium has an excitation threshold energy of approximately 20 eV and our laser has a photon energy of 1.17 eV, i.e., $E_m - E_i \gg \omega$, we ignore light-dressing of the ground state.

The second term of equation 2.87 corresponds to light-dressing of the final state. Martin makes the approximation of treating the helium as a three-state atom: the ground state $(1s^2)^1S$, $(1s2s)^1S$, and $(1s2p)^1P$ states[67]. The energy difference between these two excited levels is 0.602 eV, which is less than the next excited state $(1s3s)^1S$ that is 1.702 eV above $(1s2p)^1P$ [70]. In this three-state atom, we only need to consider the states 2^1S and 2^1P dressing each other due to the external field.

We note that the static dipole polarizability α for the two excited states are

$$\alpha_P = \frac{|\langle 2^1S | R | 2^1P \rangle|^2}{E_S - E_P} = -\frac{|\langle 2^1P | R | 2^1S \rangle|^2}{E_P - E_S} = -\alpha_S \quad (2.89)$$

where α_P and α_S is the dipole polarizability for the 2^1P and 2^1S states, respectively. E_P and E_S are the state energy of the two states. We also use the relationship between the electric field magnitude \mathcal{E}_0 and the field intensity I :

$$\mathcal{E}_0 = (8\pi\alpha_{FS}I)^{1/2} \quad (2.90)$$

where $\alpha_{FS} \approx \frac{1}{137.036}$ is the fine structure constant. Then the dipole coupling matrix element is

$$M_{SP} = [8\pi\alpha_{FS}I\alpha_P(E_S - E_P)]^{1/2} (\hat{\epsilon} \cdot \hat{\mathbf{R}}) \quad (2.91)$$

$$M_{PS} = [8\pi\alpha_{FS}I\alpha_S(E_P - E_S)]^{1/2} (\hat{\epsilon} \cdot \hat{\mathbf{R}}) \quad (2.92)$$

where the first equation refers to the inelastic scattering of $(1s^2)^1S$ to $(1s2s)^1S$ with $(1s2p)^1P$ being the intermediate dressing state. The second equation is when the roles of $(1s2p)^1P$ and $(1s2s)^1S$ are switched. Then using equation 2.85, 2.86, 2.87, 2.91, and 2.92, we can find the relative differential free-free cross section

$$\frac{d\sigma_{FF}^n/d\Omega}{d\sigma_{S0}/d\Omega} = \left| J_n(x) - [2\pi\alpha_{FS}I\alpha_P(E_S - E_P)]^{1/2} (\hat{\epsilon} \cdot \hat{\mathbf{R}}) \times \left[\frac{J_{n-1}(x)}{E_P - E_S + \omega} - \frac{J_{n+1}(x)}{E_P - E_S - \omega} \right] \times \left(i \frac{f_{P0}}{f_{S0}} \right) \right|^2 \quad (2.93)$$

and

$$\frac{d\sigma_{FF}^n/d\Omega}{d\sigma_{P0}/d\Omega} = \left| J_n(x) - [2\pi\alpha_{FS}I\alpha_S(E_P - E_S)]^{1/2} (\hat{\epsilon} \cdot \hat{\mathbf{R}}) \times \left[\frac{J_{n-1}(x)}{E_S - E_P + \omega} - \frac{J_{n+1}(x)}{E_S - E_P - \omega} \right] \times \left(i \frac{f_{S0}}{f_{P0}} \right) \right|^2 \quad (2.94)$$

where $d\sigma_{S0}/d\Omega$, $d\sigma_{P0}/d\Omega$, f_{S0} , and f_{P0} are the inelastic differential cross section from the ground state to the 2^1S state, differential cross section from the ground state to the 2^1P state, the scattering amplitude from the ground state to the 2^1S , and the scattering amplitude from the ground state to the 2^1P state, respectively.

Martin expanded the Born scattering amplitudes as a power series of the momentum transfer Q and took the radial integral to equal the integrand evaluated at the Bohr radius (a_0) to obtain

$$(if_{0P}/f_{0S}) \sim 6/Q \quad (2.95)$$

$$(-if_{0S}/f_{0P}) \sim Q/6. \quad (2.96)$$

The results of these calculations is shown in figure 2.5. This is a *qualitative* model that shows we expect to see light-dressing effects for electron-impact excitation of helium to its $(1s2s)^1S$ state in the presence of an Nd:YAG laser field.

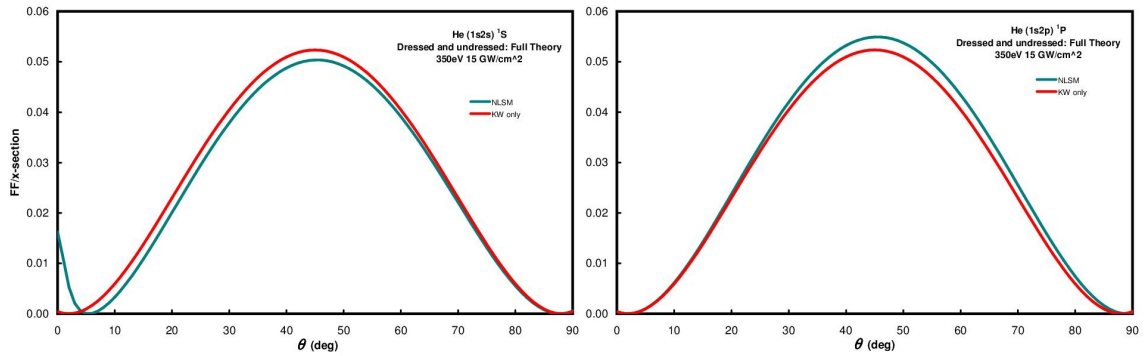


Figure 2.5: The results of the *qualitative* in-house light dressing model. The left is electron-impact excitation of helium from its ground state to the 2^1S excited state that is dressed by the 2^1P excited state. The right is when the roles of the two excited states are reversed. Figure from [71].

Chapter 3 Experimental Apparatus

To perform laser-assisted free-free (LAFF) scattering experiments, there are four things needed: electrons, targets, a laser field, and an electron detector. In our LAFF spectrometer/apparatus, we employ the *cross-beam* geometry technique with an electron beam, an atomic target beam, and a laser beam. The intersection of the three beams is known as the *interaction region*. A scattered-electron detector is aimed at the interaction region to measure the number of electrons scattered in a particular direction. The orientation of the electron beam and the detector determines the scattering plane. The laser beam enters the interaction region in the scattering plane while the atomic target beam is perpendicular to the scattering plane. A schematic of the LAFF spectrometer is shown in figure 3.1 and a photo is shown in figure 3.2.

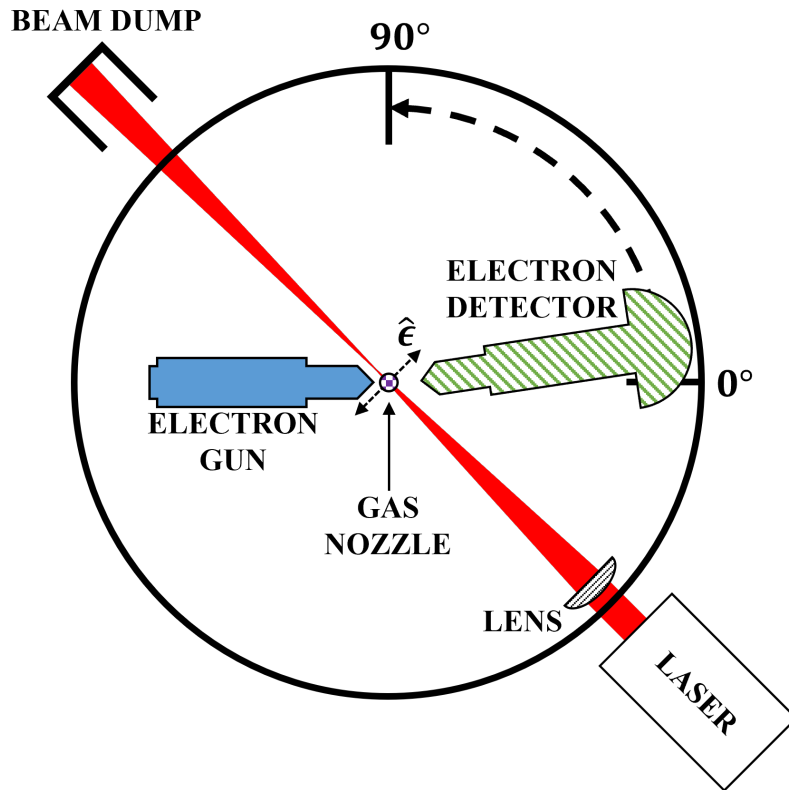


Figure 3.1: Schematic of the LAFF spectrometer (inside a vacuum chamber). $\hat{\epsilon}$ is the laser polarization direction.

The main components shown in the figures 3.1 and 3.2 are:

1. An unmonochromated *electron gun* to produce the electron beam.
2. A *gas nozzle* used to produce a helium target beam.
3. A *scattered-electron detector* to count electrons with a specific energy.

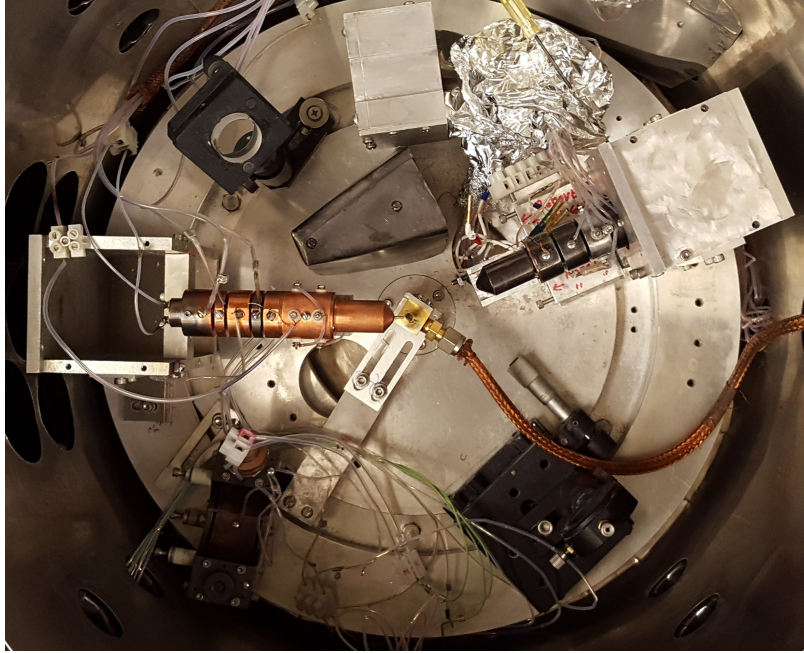


Figure 3.2: Photograph of the LAFF spectrometer. The gas jet nozzle is oriented perpendicularly outward. The laser is not in the photograph. An electrostatic shield has been removed for clarity.

4. A *laser* (located outside the chamber) to produce a laser beam.

Excluding the laser, all components are located inside of a vacuum chamber.

3.1 Vacuum System

Electron-scattering experiments must be performed in a high vacuum. Our system is able to reach pressures in the 10^{-7} torr range when the helium beam is off. During experiments, the helium beam is kept on and the background helium pressure is in the 10^{-4} torr range. A schematic of the major components of the vacuum system can be seen on figure 3.3. The system is comprised of the following components:

1. The *vacuum chamber* where the electron gun, gas nozzle, and scattered-electron detector are located. The stainless steel chamber is comprised of a hollow, upright cylindrical body with an inner diameter of 18 in, a fixed bolted-on disk bottom, and a removable top disk lid. The inner surface of the chamber is lined with high permeability μ -metal shielding to reduce the effects of external magnetic fields. A vacuum seal between the bottom, top, and body is made with Viton o-rings. A rail-mounted hoist is used to lift the lid when the chamber is at atmospheric pressure.

Extending from the body, top, and bottom are multiple ConFlat flanges. The flanges are used for the following:

- an *ion gauge head* to monitor the pressure inside of the chamber.
- multiple voltage feedthroughs to electrically connect the electron gun and detector to external power supplies.
- a *gas feedthrough* to connect the external helium tank to the gas nozzle.
- two high-transmission *laser windows* for the laser to enter and exit the system.
- a *rotary feedthrough* to position the scattered-electron turntable.

A pumping port is used to connect the chamber to the diffusion pump.

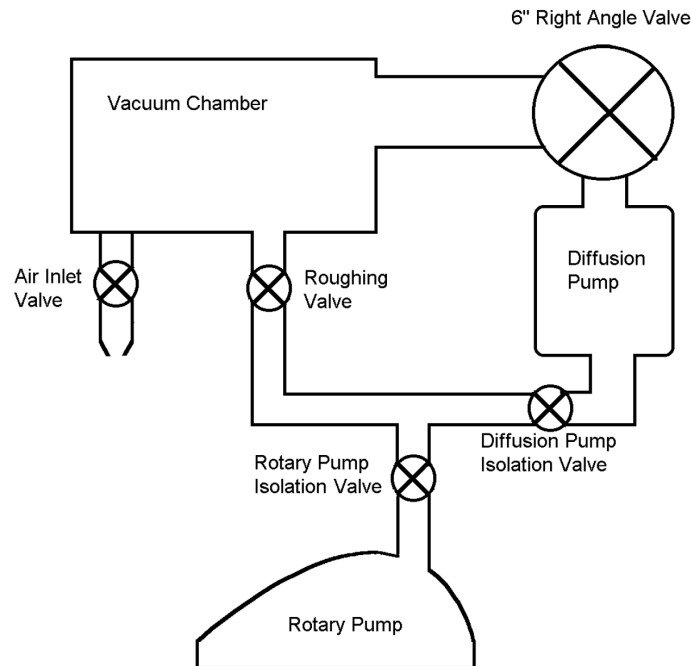


Figure 3.3: Schematic of the vacuum system. Modified from [72].

2. A Varian VHS-6 *diffusion pump* is used to achieve high vacuum in the chamber. The diffusion pump contains a reservoir of oil at its base which is heated to its gas phase. The oil vapor rises through a jet assembly where it is directed back down towards the inner wall of the pump. This directs other gases down the body of the pump resulting in excess gas at the lower levels of the pump where it is evacuated by a rotary *backing pump*. The body of the diffusion pump is externally wrapped by a water cooling line that condenses the oil on the interior surface of the pump. The oil returns to the reservoir to be heated again.

On top of the diffusion pump is a *cold trap baffle* to prevent oil from the diffusion pump from entering the chamber. The trap is cooled by a Freon refrigerator to temperatures in the -40's °C. A thermocouple is placed at the cold trap to monitor its temperature.

3. A Welch Duo-Seal *belt-drive pump* is used for two purposes. Its primary duty is to be the backing pump for the diffusion pump. Its second duty is to evacuate the vacuum chamber, i.e., pump the vacuum chamber down to 1 mtorr, before it is connected to the diffusion pump. The exhaust is vented to a fume hood.

Other components include two thermocouple gauges and various valves. The thermocouple gauges are used to monitor the pressure of the diffusion pump and inlet line of the belt-drive pump. Thermocouple gauges can measure pressures from 1 mtorr to standard atmosphere. The valves are used to isolate the various components of the system, such as when the chamber needs to be opened for maintenance or the diffusion pump needs to be isolated as the chamber is evacuated. The location of the valves are shown in figure 3.3.

The pumps and the cold trap are normally kept on continuously. There are several conditions where the vacuum system will shutdown automatically. They include:

1. interruption of electric power.
2. interruption of water flow in the diffusion pump cooling line.
3. sudden change in the pressure inside the chamber.
4. pressure inside the chamber becomes too high.
5. overheating of the diffusion pump.

The diffusion pump and external power supplies are kept on a protected circuit that will turn off and remain off until the system undergoes a manual reset if one of the above conditions are met. The belt-drive pump and cold trap are kept on separate outlets and will only turn off for loss of electric power. Once power is restored, they will turn back on.

3.2 Electron Gun

The electron beam for this work was produced by an in-house electron gun based on the design by Erdman and Zipf[73]. The electrons are produced by thermionic emission from a cathode filament made from 1% thoriated tungsten wire with a diameter of 0.114 mm. A series of electrostatic lenses are used to shape the electron beam produced by the cathode until it goes through a nosecone of a known diameter directed at the interaction region. A diagram of the electron gun is shown in figure 3.4. A photograph of the electron gun can be seen in figure 3.2.

The cathode is in a circuit with two power supplies: a constant current source that heats the filament and a constant voltage source to hold the cathode at a known electric potential. In this work, the cathode was held at the electric potential -350 V. We consider the interaction region to be at electric ground (0 V) thus the incident electrons have an energy of 350 eV. The cathode is placed in a copper housing with a small aperture such that the tip of the cathode and the aperture are aligned. The electric potential on the housing can determine the intensity of the electron beam. A

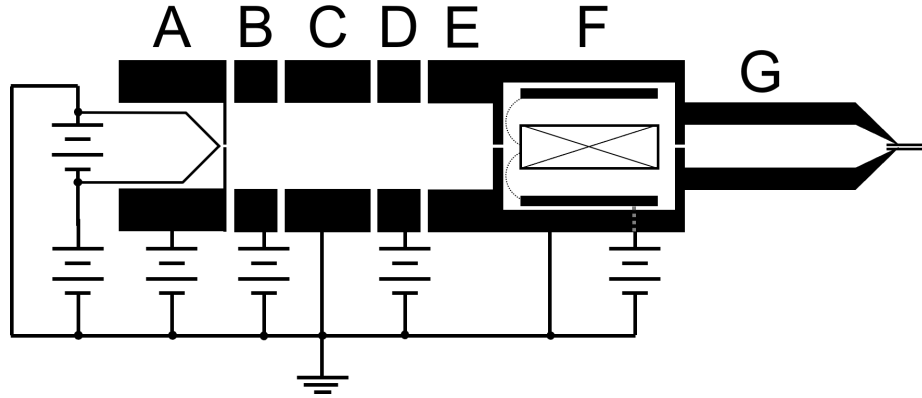


Figure 3.4: Diagram of the electron gun. A is the cathode housing with the cathode filament, B–E are electrostatic lenses, F is the “deflector plates” assembly, G is the nosecone.

positive voltage between the cathode and its housing will usually produce a stronger electron beam. However, a negative voltage may also produce a stronger electron beam due to focusing effects into the aperture.

Following the cathode housing are two sets of two electrostatic lenses. Each set includes a *thin lens* and a *thick lens* where the length of the thin lens is half of that of the thick¹. The thick lenses are electrically-grounded while the thin lenses have a non-zero electric potential. Following these is the “deflector plates” assembly. The housing of the assembly is a thin, cylindrical copper shell capped by copper plates with a small aperture in the center and is electrically-grounded. Inside the assembly are four rectangular plates that are top, left, down, and right from the perspective of the electron. The four plates are electrically connected to each other and to a single constant voltage supply². Following the deflector plates assembly is an electrically-grounded copper nosecone that is tipped with a molybdenum tube with an inner diameter of 0.75 mm.

The cathode housing, the four electrostatic lenses, and the deflector plates assembly, which includes 1 mm collimating apertures (see figure 3.4), shape the electron beam as it travels towards the tip of the gun. The molybdenum tube allows the tip of the electron gun to be placed close to the interaction region without the risk of it being hit by the laser beam. The electron beam at the interaction region can then be considered parallel due to the relatively long collimator and due to the short distance between the tip of the electron gun and the interaction region. This can be seen in figure 3.4.

¹The thin lens in our electron gun has a length of 1/4 in while the thick lens had a length of 1/2 in. Both lenses have an outer and inner diameter of 1 in and 1/2 in, respectively.

²In the past, each plate was connected to a constant voltage supply. The purpose of the deflector lens was to create a non-cylindrical symmetric electric field to adjust the path of the outgoing electron beam. Since the four plates are now electrically connected to each other and to a single voltage supply, it is effectively another electrostatic lens. For historic reasons, we still refer to this as the *deflector lens*.

3.2.1 Electron Gun Tuning

Excluding the electrically-grounded components of the electron gun, all components are connected to a power supply which can be adjusted. The cathode current and its electric potential were not changed in this work. Changing the cathode current and electric potential changes the energy profile of the electron beam. Due to the electron gun being used in previous works[32, 33, 34, 14], the tuning of the electron gun is known³. However, the electron gun must still undergo occasional *fine tuning*. We believe the main reason for this is due to oil vapors from the diffusion pump entering into the chamber despite the cold trap baffle. It settles on non-grounded electrostatic lenses and breaks down to create a dielectric dark film that may cause charging effects⁴. The fine tuning can compensate for the charging effects. Due to the lack of a functioning Faraday cup, to directly measure the electron beam intensity, tuning is performed by optimizing the scattered-electron signal.

Due to the elastic scattering peak increasing by orders of magnitude at small scattering angles[64], it was necessary to reduce the scattering count rate to more manageable levels. In previous work[14], adjusting the voltage between the cathode and its housing accomplished this. However, in the present work, we noticed unstable energy shifts that would take several hours to stabilize. It was decided a better method was to intentionally detune the second thin lens (from the perspective of the electrons). There were two concerns reducing the count rate using this method:

1. Charging of electron gun components
2. Divergence of the electron beam

For the first concern, following the second thin lens is a thick, electrically-grounded lens followed by the first aperture of the deflector plates assembly (which is also electrically-grounded). There is less of a concern about charging effects if the electrons are impacting electrically-grounded components. For the second concern, recall that the apertures of the deflector plates assembly and the nosecone acts as a collimator. The tip of the nosecone is also placed close to the interaction region. Due to this, the divergence of the electron beam is not a concern. As long as the electron gun tuning for measuring free-free electrons and the scattering count rate of the scattering peak are the same, no corrections are necessary when calculating the relative cross section.

3.3 Gas Jet Nozzle

The target beam is produced by helium gas that continuously flowed through a stainless steel nozzle inside the chamber from an external tank. The diameter of the target

³There was an instance where a new tuning of the electron gun was needed due to a power supply failure and the lack of a suitable replacement at the time. We found no noticeable difference in the electron beam profile and gave identical results for elastic free-free experiments for a scattering angle of 45° , the experiments we used to normalize our results.

⁴The dark film is visible on figure 3.2 where the second thin lens (from the perspective of the electrons) is a darker shade than the other electrostatic lens.

beam is closed to 1 mm due to the inner diameter of the nozzle being 1 mm, and it is placed right under the interaction region⁵. The pressure at the interaction region can be controlled by an external valve between the tank and the nozzle. To keep the pressure constant between experiments, the background pressure of the chamber when the helium beam was left on was monitored by an ion gauge.

3.4 Scattered-Electron Detector

The scattered-electron detector, which we also refer to as the *electron detector*, can measure the number of electrons scattered at a specific direction and energy. In this work, the word *detector* has two different usages. The *scattered-electron detector* refers to the system of electrostatic lenses, the hemispherical electrostatic energy analyzer, and the position-sensitive detector. The last component is the second usage of *detector*. A diagram of the scattered-electron detector can be seen in figure 3.5. Excluding the position-sensitive detector, all components of the scattered-electron detector are covered in a thin layer of graphite⁶. A front cover, also covered in a layer of graphite, is also placed in front of the electron detector. In figure 3.2, one can see the electron detector with the cover off. The power supplies setting the electric potential of the electron optics are electrically floated on a *ramp*, comprised of two power supplies in series. The purpose of the ramp will be covered in section 3.4.3.

The scattered-electron detector is on a turntable inside of the chamber that can be rotated externally without the need to open up the vacuum chamber. An external single-turn rotary ($400 \pm 3\%$) k Ω potentiometer is used to determine the scattering angle inside the chamber. Each scattering angle has a corresponding resistance measurement from the potentiometer. We determine what resistance corresponds to $\theta_{scatt} = 0^\circ$ by mechanical means when the chamber is open, and later checking for scattering symmetry in the detector signal about 0° . Using this latter technique, we found that the resistance corresponding to 0° shifted from the beginning to the end of our data collection. During the course of the experiment, the resistance was lowered by 0.08 k Ω , which corresponds to a shift of -0.007° , a negligible shift.

⁵When aligned, the gas nozzle is placed as close to the interaction region as possible while still missing the laser beam.

⁶The graphite is applied by using Dag from Acheson company, colloidal graphite in a solvent that evaporates when applied. Historically, applying Dag on the electron gun's electrostatic lenses created a "plastic" under electron bombardment that caused instabilities with the electron beam[72].

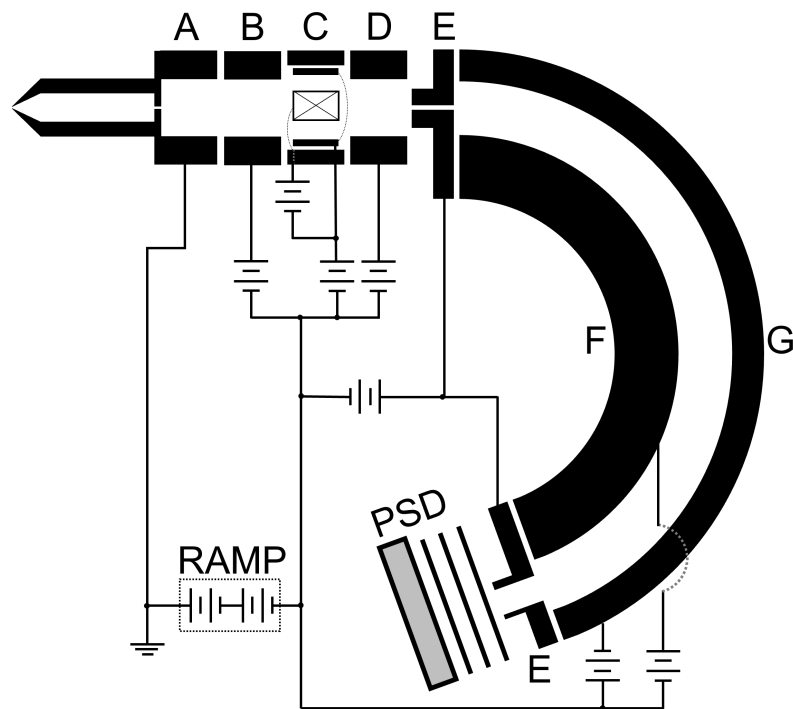


Figure 3.5: Wiring diagram of the electron optics of the electron detector. A is the nosecone; B–D are electrostatic lenses (C contains deflector plates); E are the entrance and exit plates of the analyzer; F and G are the inner and out hemispherical-sector electrodes of the analyzer, respectively. PSD is the position-sensitive detector. Elements B–G are electrically floated on the RAMP.

3.4.1 Electrostatic Lenses

The first component of the scattered-electron detector is the electrically-grounded nose cone with an opening diameter of 1.5 mm which corresponds to an angular acceptance of approximately 2.5° ⁷ Following the nosecone are three electrostatic lenses. The second lens contains four rectangular electrostatic deflector plates top, left, down, and right from the perspective of the incoming electron. The top and bottom plates are held at the same electric potential as the second electrostatic lens. The left and right plates are attached to two separate power supplies and are electrically-floated on top of the power supply connected to the second lens. The purpose of the lenses is to both slow and shape the incoming electron beam. This is accomplished by the electric field due to the voltages between the electron optics.

3.4.2 Electrostatic Energy Analyzer

The Comstock Model AC-901 Electrostatic Energy Analyzer, which we will now refer to as the *analyzer*, consist of two concentric hemispherical-sector electrodes operated with a constant voltage difference between them. This results in an electric field that is directed radially outwards. The analyzer is a velocity selector for charged particles and only electrons with kinetic energy within a certain range can pass through. All components (with the exclusion of electric insulators) are covered in graphite.

The negatively charged electrons experience an acceleration radially inwards due to the electric field. This specific kinetic energy required to traverse the analyzer is the *transmission energy*. This energy can be derived using classical mechanics and electrostatics⁸. Due to the shape of the analyzer, the electric field between the two electrodes is spherically symmetric and radially outward. Since fringe effects are ignored, one can represent the electric field as a field due to some fictitious, positive, point charge q , where q is placed at the spherical origin of the two spherical electrodes. We relate q to the voltage between the electrodes. This can be accomplished by finding using the relationship between voltage and electric field:

$$\Delta V = - \int_{r_2}^{r_1} \vec{E} \cdot d\vec{r} = - \int_{r_2}^{r_1} (k_e \frac{q}{r^2} \hat{r}) \cdot (dr \hat{r}) = k_e q \left(\frac{r_2 - r_1}{r_1 r_2} \right) \quad (3.1)$$

$$q = \frac{\Delta V}{k_e} \left(\frac{r_1 r_2}{r_2 - r_1} \right). \quad (3.2)$$

where ΔV is the voltage between the electrode; r_1 and r_2 are the radial distance from the origin to the inner and outer electrode, respectively; and k_e is the Coulomb constant.

⁷The angular acceptance is determined from the solid angle formed by the area of the detector entrance aperture and its distance from the interaction region.

⁸Specifically, one needs to relate centripetal with electrostatic force. One can find this information in many textbooks but I will refer to Taylor[50] and Griffiths[60]

An incoming electron experiences a centripetal force due to the electrostatic attraction between it and the point charge. Relating the two, we obtain

$$F_c = m_e \frac{v^2}{r} = k_e \frac{eq}{r^2} \quad (3.3)$$

where F_c is the centripetal force the electron undergoes, m_e is the mass of the electron, v is the speed of the electron, $e = |e|$ is the charge magnitude of an electron, and r is the distance from the origin to the trajectory of the electron. Using equation 3.2 and 3.3, we can find the transmission energy

$$TE = \frac{1}{2} m_e v^2 = \frac{r_1 r_2}{2r(r_2 - r_1)} e\Delta V \quad (3.4)$$

The dimensions are given in the technical brochure[74]: $r=36.5$ mm, $r_1=32.5$ mm, and $r_2=40.5$ mm.

$$TE[eV] = 2.25 \Delta V \quad (3.5)$$

The transmission energy also determines the spread of energies of the electrons passing through the analyzer. We found that the the energy spread is approximately 1 eV. Which is similar to the width of the electron beam and enables that observation of a complete free-free peak.

3.4.3 Tuning

The tuning of the scattered-electron detector is determined by power supplies electrically connected to the electron optics as shown in figure 3.5. All power supplies are electrically floated on two power supplies in series (for coarse and fine adjustments) that we refer to as the *ramp*. The ramp allows us to adjust the energy of an incoming electron to equal the pass-energy, the energy a scattered-electron must have to enter the analyzer at the transmission energy after passing through the electron optics. To begin the tuning of both the electron gun and electron detector, we first obtain an electron beam and have the electron detector able to detect some scattered electrons. This can be done through simulations of the electron optics, such as with SIMION[75]. However, both are electron gun and detector are “mature” from previous works. Thus, we have a “coarse tuning” that fulfills our first requirement.

Due to the presence of the collimator in the electron gun and the tip of its nosecone being very close to the interaction region, the divergence of the electron beam is not a primary concern. We want to maximize the electron beam current and maximize our electron detector’s efficiency. Due to the lack of a functional Faraday cup, we use an alternative method of maximizing the electron beam current. We set the pass-energy of the detector at a scattering peak (we used the unresolved $(1s2s)^1S$ and $(1s2p)^1P$ scattering peak, which we will now refer to as the inelastic peak). We tune both the electron gun and detector to maximize the intensity of the peak.

We first tune the electron detector by adjusting the electric potentials of the three electrostatic lenses and the deflector lenses in an iterative process to maximize the

electron count rate of the inelastic peak. We found that the entrance and exit plate of the analyzer required no adjustments. We then do the same with the electron gun by adjusting the electric potential on the two thin lenses and the deflector plates to once again maximize the intensity of the peak. We avoid adjusting the electric potential of the cathode housing when possible due to the long period of time needed for the electron beam to stabilize. We repeat this process until we are confident both the electron gun and detector are tuned. Due to the charging effects discussed in section 3.2.1, the electron gun requires the occasional fine tuning. This is accomplished by adjusting the electric potential on the electron optics of only the gun to maximize the intensity of the scattering peak.

Since the detector is tuned on the inelastic scattering peak, the detector was most responsive in this region of the electron energy-loss spectrum. Thus, when measuring for free-free electrons near the elastic-scattering peak, the detector is slightly out-of-tune. However, since we are looking for relative cross sections, this is not a significant concern.

3.5 Data Acquisition

This section will discuss the data acquisition of measuring the number of scattered electrons. The four key components of this system is the position-sensitive detector (PSD), the Nuclear Instrumentation Modules (NIM), the in-house data acquisition device (DAQ), and a computer for analysis⁹.

3.5.1 Position-Sensitive Detector

At the end of the analyzer is the position-sensitive detector (PSD) which allows for temporal and spatial measurement of the incoming electron. The PSD is comprised of three microchannel plates (MCPs) followed by the square resistive anode encoder (RAE). Each MCP is an electron multiplier where an incoming electron causes a large burst of secondary electrons from one or more microchannels of the MCP. A high voltage across the MPCs brings the electrons to the next MCP and eventually to the RAE. When the large burst of electrons is deposited on the RAE, the four corners of the RAE will measure the relative charge (the portion of the charge measured at a corner relative to the total charge)[76]. The four signals are sent to the Quantar Technology 24012 Detector pre-amp that contains four charge and shaping amplifiers along with one fast shaper amplifier for the sum of the four signals. They are sent to the Quantar Technology 2401B position analyzer, where the signal is processed to determine if the signal corresponds to a real electron impact and its position on the RAE. The count rate of total incoming pulses that is above a certain threshold is referred to as the *RATE* while the count rate of fully processed, valid event (what are considered real electron impacting the RAE) is referred to as the *STROBE* (STR)[77]. The temporal and spatial data is sent to the data acquisition device. The lack of an exit aperture on the analyzer results in an energy spread of electrons that impacted

⁹The specific details on the analysis will be covered in chapter 4

the RAE. Due to the orientation of the PSD, the y-position of an electron corresponds to its energy.

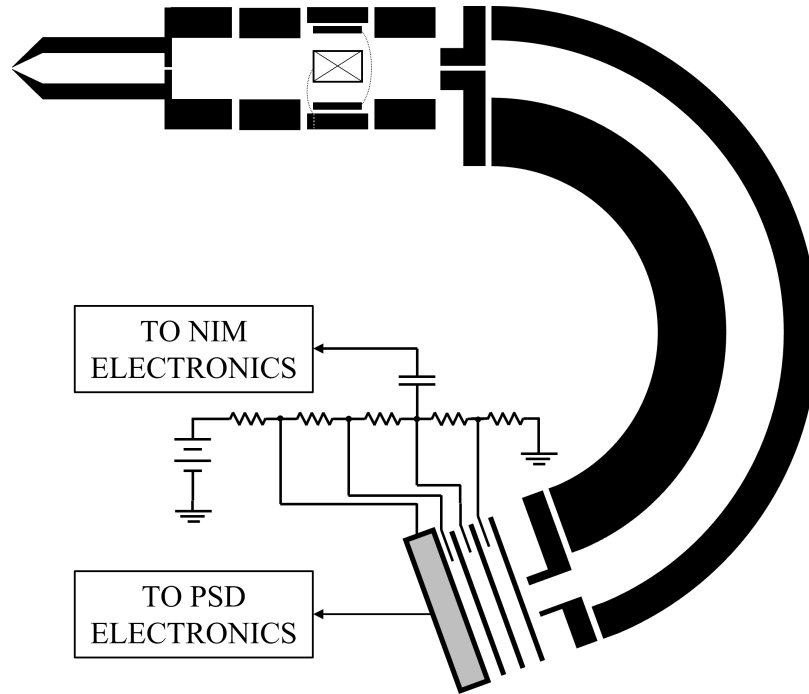


Figure 3.6: Schematic of the PSD and NIM with wiring diagram. PSD and NIM ELECTRONICS are expanded on figure 3.8.

However, the STROBE is not the true count rate of electrons detected due to dead-time effects. The processing of the signals gives the PSD a dead-time of $4 \mu\text{s}$. The dead-time curve due to the processing of the signal is shown in figure 3.7. There is an additional dead-time effect if the microchannels in the MCPs do not have sufficient time to “recharge.” This dead-time is unknown due to its difficulty to quantify (even by the manufacturers)[78].

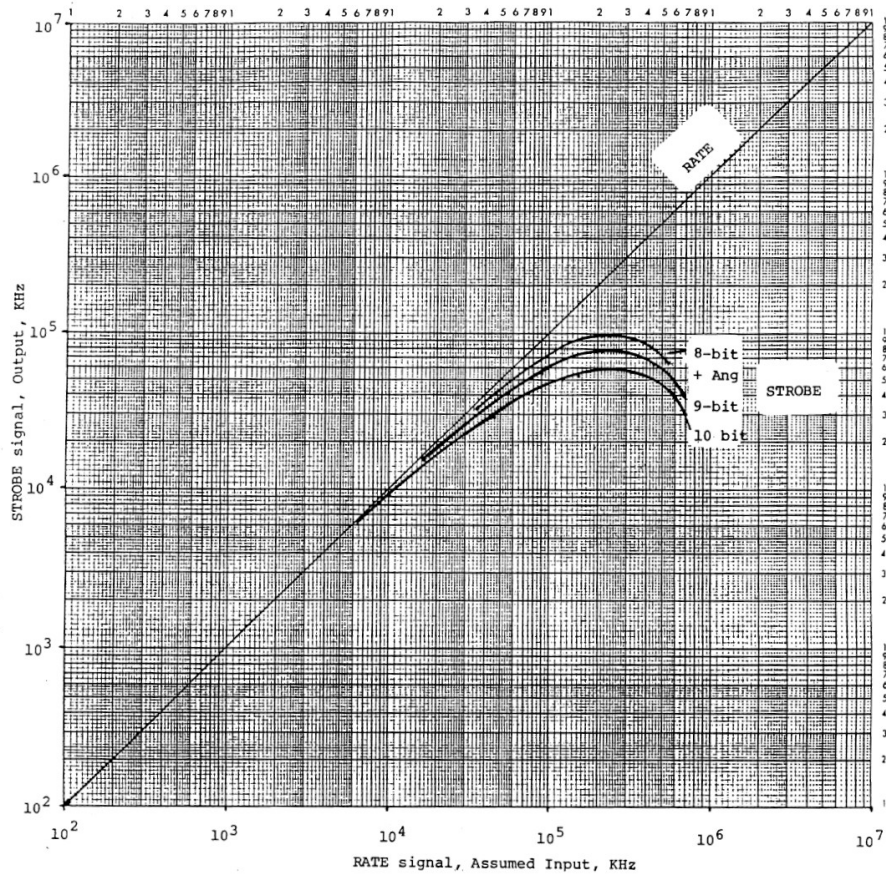


Figure 3.7: PSD electronic dead-time curves. Model used in our work is the 8-bit digitized output. Figure from [78].

3.5.2 Data Acquisition Device

Fully processed data from the position analyzer is sent to our data acquisition device (DAQ) built in-house by W. L. Fuqua III and T. G. Porter of the UK Physics & Astronomy electronic shop. The DAQ uses a Parallax Inc. Propeller™ 1 chip that is comprised of eight independent 32-bit cores processors that is synchronized by a common system clock. The maximum clock speed is 80 MHz (which results in time intervals of 12.5 ns). The DAQ is triggered to collect data from the position analyzer for a pre-determined time duration after a pre-determined time delay appropriate to the laser Q-switch timing (see section 3.7). The DAQ is controlled by a Microsoft Visual Basic 6.0 program on a Microsoft Windows XP computer. The analysis is done by a Microsoft Excel 2002 Visual Basics program. The analysis will be covered in chapter 4.

3.5.3 Nuclear Instrumentation Modules

To compensate for the relatively large dead-time of the PSD, a nuclear instrumentation modules unit (NIM) was used in addition to the PSD. When the electron reaches the second MCP of the PSD, a signal is also sent to the NIM unit as shown in figure 3.8. The voltage pulse from the second MCP is amplified by an Ortec 9301 Fast Pre-Amplifier[79] and shaped by an Ortec 579 Fast Filter Amplifier[80] (doing a similar function to the PSD Preamplifier). An Ortec 473A Constant Fraction Discriminator[81] is used to determine if the signal corresponded to a real electron impact event. Ortec 661 RateMeter and Ortec 871 Timer and Counter are used to count the number of events. These measurements are not recorded by the DAQ and are instead recorded manually.

The advantage of using the NIM unit over the PSD is in its much faster processing time that allows us to measure higher count rates with negligible dead-time effects. From the literature, the NIM unit may have a dead-time as low as 400 ns and up to approximately 1 μ s, significantly less than the PSD deadtime that has a lower limit of 4 μ s. The threshold for significant dead-time effects on the NIM was determined to be approximately 150 kHz. The reasoning for this is explained in section 4.2.

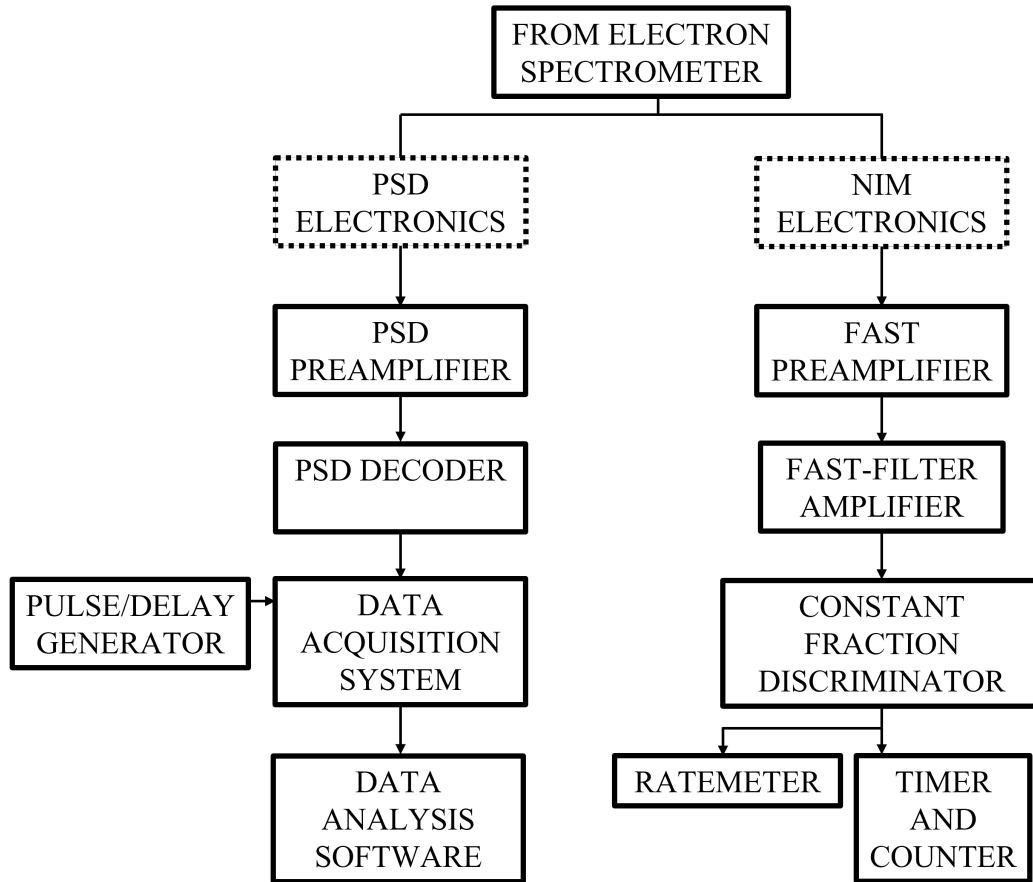


Figure 3.8: Schematic of signal processing.

3.6 Laser

The intense laser field present at the interaction region was supplied by a Continuum Powerlite 9030 Nd:YAG laser. The laser has a repetition of 30 Hz and produces a laser beam with a wavelength of 1064 nm (which corresponds to the photon energy of 1.17 eV). The laser has a nominal energy-per-pulse of 1.6 J and a pulse width of 5-9 ns¹⁰. The laser is comprised of an oscillator cavity (labeled in figure 3.9), two amplifiers, and various *passive* optical elements to control the direction, shape, and polarization of the laser beam. The oscillator and amplifiers are comprised of an Nd:YAG solid-state rod and a xenon flash lamp encased in a water-cooled laser head with a *high brilliance magnesium oxide diffuser*[82]. The flash lamps are discharge lamps used to *optically pump* the rods to achieve a *population inversion*, when a higher energy level is more populated than a lower energy level[53].

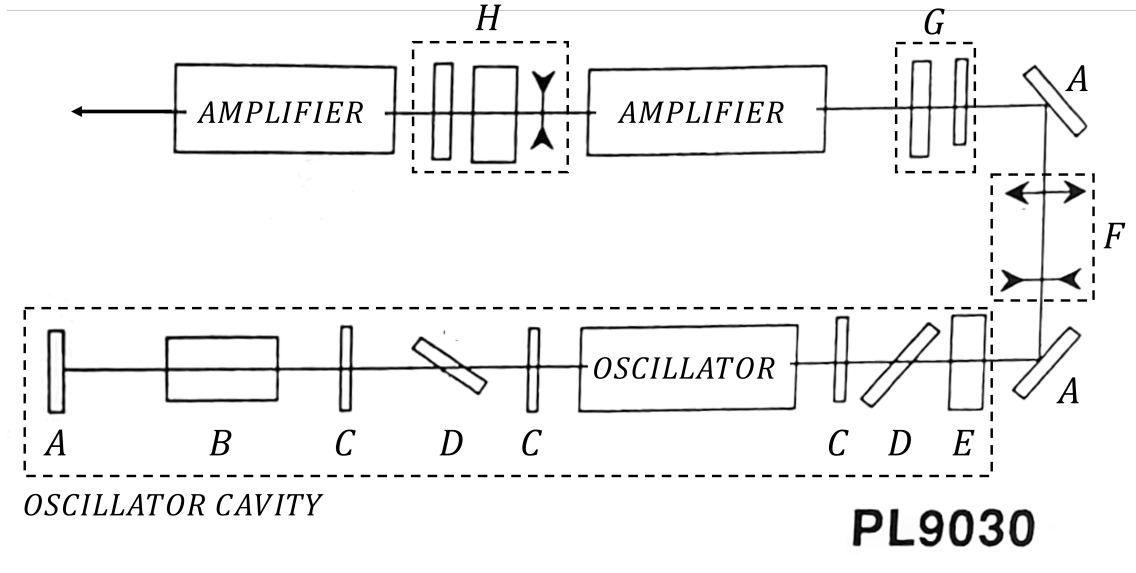


Figure 3.9: Diagram of laser bench. Item(s) labeled *A* are the laser mirrors, *B* is the Pockels cell, *C* are the $\lambda/4$ plates, *D* are the dielectric polarizers, *E* is the output coupler, *F* is the beam expander made from a diverging and converging lens, *G* is a $\lambda/2$ plate and an apodizer, and *H* is a diverging lens, rotator, and an apodizer. Modified diagram from [82].

The oscillator cavity is comprised of a mirror, three $\lambda/4$ plates, the oscillator laser head, two dielectric polarizers, an output coupler, and a Pockels cell. The dielectric polarizers and output coupler transmit horizontally polarized light but deflects vertically polarized light. The Pockels cell can be considered as an *active* wave-plate where it rotates the polarization when on but is transparent to the light when off. When the Pockels cell is off, light is trapped within the cavity and the laser cannot lase due to the configuration of the passive optical elements in the cavity. With the

¹⁰The pulse width is the full-width half-max (FWHM) of the laser pulse.

addition of an active Pockels cell, most of the light in the cavity is horizontally polarized and is allowed to leave. The laser beam goes through a beam expander and two amplifiers increasing both its size and energy-per-pulse. The remaining passive elements are used to shape the beam and control its polarization. The triggering for the laser heads and Pockels cell is controlled by a Stanford Research System, Inc. Model DG535 pulse generator with an accuracy of 1.5 ns[83]. The delay generator will trigger the flash lamps to *fire* at a rate of 30 Hz. During the flash, the higher energy levels in the rod will start to populate. After a pre-determined delay, the delay generator will send another pulse, the *Q-switch delay pulse*, to activate the Pockels cell allowing the laser beam to leave the oscillator cavity. The maximum population inversion is achieved 355 μ s after the flash lamps are triggered, i.e., when the power output is maximized. More information on triggering and timing will be covered in section 3.7.

After the laser beam leaves the laser, it is directed into the vacuum chamber through a laser window by a mirror. Once inside the chamber, the beam is focused slightly beyond the interaction by a +150 mm focal length lens. By using Linagraph burn paper, we know the diameter of the laser beam at the interaction region. The direction of the laser polarization relative to the incident electron momentum is -133° (see figure 3.1 where clockwise is negative angular displacement). Occasionally, the mirror in the oscillator cavity requires adjustments. Which was done periodically during this work.

3.6.1 Flash Lamp Degradation and Measuring Pulse Width

Over time, the flash lamps used to optically pump the Nd:YAG rods will degrade. The degradation is due to the erosion of the flash lamp's electrodes causing opaque deposits to settle on the inner surface of tube. This is more prevalent on the cathode end as shown in figure 3.10[84]. The degradation of the flash lamps results in two noticeable effects: reduction of output power and an increase in laser pulse width. Direct measurements of the output power is not experimentally feasible due to the lack of a power meter with a sufficiently high damage threshold. Normalization due to reduction of output power will be addressed in section 4.4. The pulse width can be found by aiming a photodiode at a laser mirror as the beam is being reflected. The laser mirror has an average reflectance of 0.995 so what is being measured by the photodiode is a tiny fraction of the light that has been scattered rather than reflected. This prevents the saturation of the photodiode allowing us to measure the FWHM. An upper and lower bound was found by measuring the FWHM with flash lamps that needed to be replaced and measuring again with new flash lamps. We concluded that the pulse width of a laser beam is 18 ± 3 ns.

Free-free transitions can only occur if the scattering event occurs in an external electromagnetic field. In LAFF experiments, the field is supplied by a laser. While pulsed lasers can give us an intense field at the interaction region, the drawback is the pulses are very short. For a 30 Hz laser, the data-taking efficiency is $(5.4 \pm 0.9) \times 10^{-7}$. It takes approximately 2 million seconds of real-time to obtain 1 second worth of experimental data.

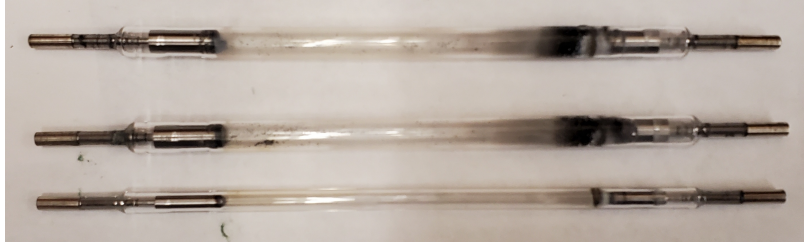


Figure 3.10: Degraded flash lamps. The left side is the anode and the right is the cathode.

To monitor the status of the flash lamps, a thermocouple is attached to the beam dump to monitor its temperature which is recorded by the data-acquisition software. New flash lamps raise the temperature of the beam dump to approximately 40°C above room temperature. This will progressively drop over time. While this can give us the qualitative status of the flash lamps, we found that this method is not precise enough to quantify the reduction in output power of the laser. It also takes approximately an hour for the beam dump to reach thermal equilibrium. There are also external factors that affect the temperature of the beam dump such as room temperature and humidity, which we do not have precise control over.

We also note that as the flash lamps decay, there is an additional delay in the laser beam leaving the laser. The delay is large enough where it is noticeable in our timing spectrum (see section 4.1). This requires us to shift the time bins that we believe contain free-free electrons during the data analysis. This shift can be as large as 3 to 4 time bins (37.5 to 50 ns). However, this delay occurs slowly over the course of weeks. We periodically ran a free-free experiment for one photon emission of elastically scattered electrons at a scattering angle of 45° to monitor the shift and make adjustments in our analysis if necessary. We also noticed that the pulse width increased as the flash lamps decayed. Since the increase is of order nanoseconds while a time bin is 12.5 ns, no change was necessary to the data analysis.

3.7 Timing

Precise timing is required in a LAFF experiment for two reasons: The laser requires precise and stable triggering and data collection must include the time when the laser beam was present at the interaction region. A Stanford Research System, Inc. Model DG535 pulse generator was used to both trigger the laser and our DAQ. Table 3.1 shows the timing of major events and a visual representation is shown in figure 3.11. Since the repetition rate of the laser is 30 Hz, the delay generator is set to 30 Hz.

At the start of each cycle, the delay generator sends a $120\ \mu\text{s}$ long pulse to the laser and the DAQ. The rising edge triggers the flash lamps to fire which also starts the population inversion. The population inversion is represented in figure 3.11 by the green dashed line. The falling edge of the pulse triggers the DAQ which will start to collect data after a $228\ \mu\text{s}$ delay. The delay generator will send a second pulse to the laser after a $355\ \mu\text{s}$ delay. This Q-Switch pulse is sent to the Pockels cell in the

Time (μs)	Event
0	Flash lamps fire
120	DAQ Trigger
348	Data Acquisition Begins
355	Q-Switch Triggered
508	Data Acquisition Ends

Table 3.1: The timing of major events during the experiment.

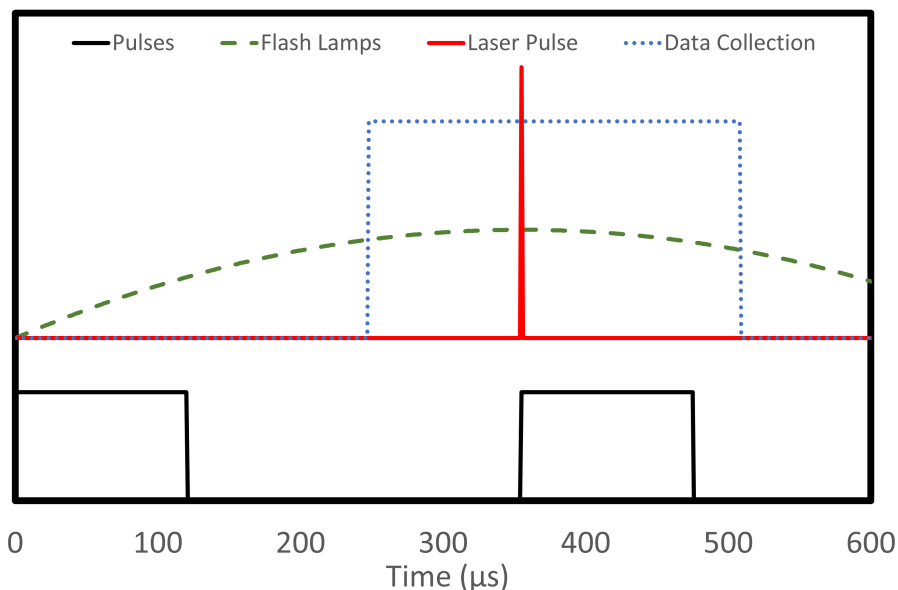


Figure 3.11: Schematic of the timing diagram. The timing corresponds to the times listed on table 3.1.

oscillator cavity to fire the laser. This occurs when the population inversion is at its apex, thus maximizing the laser power output. 228 μs after the DAQ was triggered, it will start to collect 160 μs worth of data. The collection window is large to ensure free-free electrons are detected but also to gather a large background sample size.

Chapter 4 Data and Analysis

In this chapter, we present our analysis of our LAFF experiments in helium. As shown in equation 2.67, the relative cross section was found by taking the ratio of the free-free to the field-free scattering peak rate¹. Figure 4.1 gives a schematic of the energy profile when the laser is on and off. The region Q and P are located one photon energy away from the scattering peak (region R). The difference in regions P and Q is the free-free scattering rate while region R is the field-free scattering peak count rate.

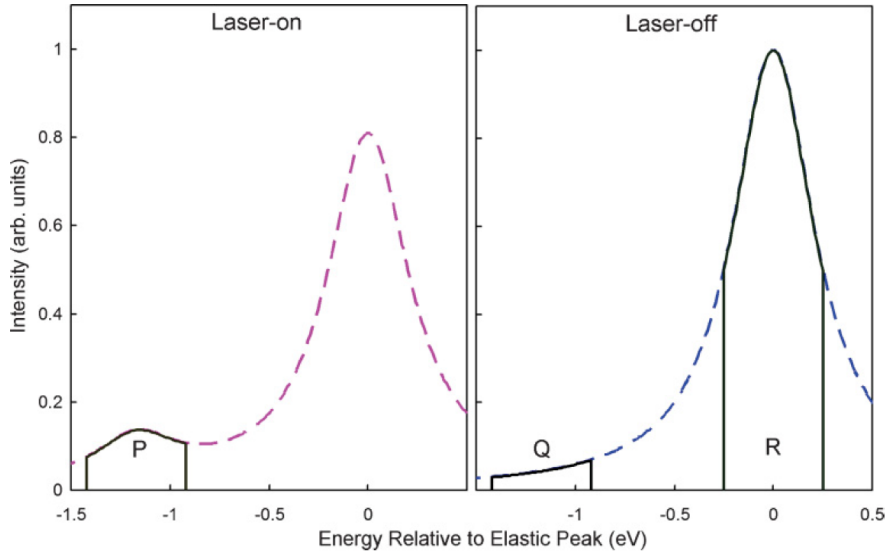


Figure 4.1: A schematic of the energy profile of scattered electrons with the laser-on (left) and laser-off (right). P , Q , and R are measured rates in the experiment. Figure from [32].

Each experiment consisted of a timing spectrum that measured the number of electrons detected in 12.5 ns time intervals. An example of a typical timing spectrum is shown in figure 4.2. By performing experiments at various scattering angles, a free-free angular distribution was made for elastic and inelastic one photon free-free processes. The method of calculating the relative cross sections and the process of normalization is described below.

4.1 Free-free Count Rate

In each experiment, we took a timing spectrum where the number of electrons detected were placed into 12.5 ns time bins. By calculating the time it would take for

¹*Free-free* refers to electrons that underwent free-free transitions while *field-free* refers to the scattering peak when the laser was not present at the interaction region.

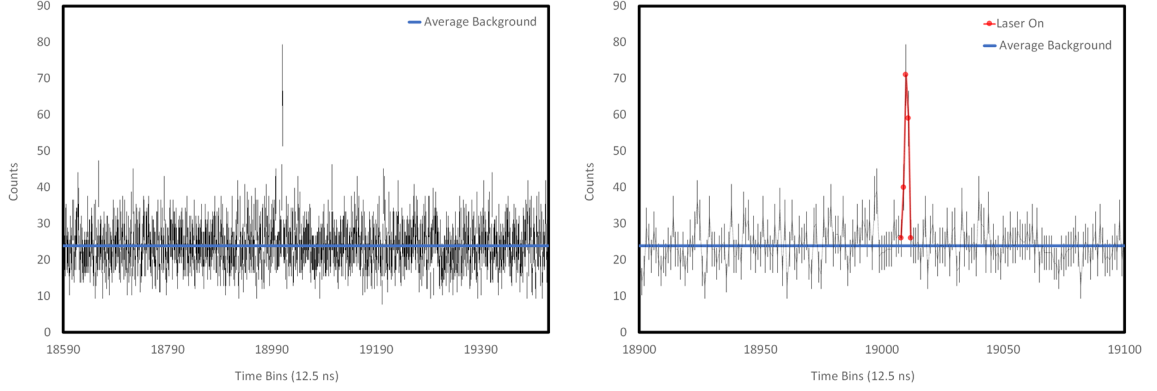


Figure 4.2: An example of a timing spectrum. This experiment was an 1 photon emission elastic LAFF experiment that ran for 1 hour. The blue line is the average background count $N_{background}$. The left plot shows the full time range of data collection. On the right plot, the data points in red are the time bins when the laser beam was present at the interaction region. The lines were included to guide the eye.

the laser beam to be present at the interaction region (and with the benefit of previous works on this apparatus[32, 33, 35, 14]), we know which time bins contains electrons that were scattered in the presence of the laser field. By measuring the background counts and the use of Poisson statistics (see appendix A), we were able to find the count rate of excess electrons that are free-free electrons. As one can see in figure 4.2, a timing spectrum has hundreds of time bins correspond to scattered electrons when the laser was not present at the interaction region. We were able to obtain the average background counts per bin $N_{background}$ and its uncertainty $\delta N_{background}$

$$N_{background} = \frac{1}{N_{bins}} \sum_{i=1}^{N_{bins}} x_i \quad (4.1)$$

$$\delta N_{Background} = \frac{1}{N_{bins}} \sqrt{\sum_{i=1}^{N_{bins}} x_i} \quad (4.2)$$

where N_{bins} is the number of laser-off time bins and x_i is the number of counts in the i^{th} laser-off time bin.

Knowing the background counts per bin, we are able to find the total free-free count rate \dot{N}_{FF} . The free-free signal on the timing spectrum spans 5 time bins (which we will refer to as the *laser-on bins*), corresponding to 62.5 ns. Despite the measured pulse width of the laser being (18 ± 3) ns, there is a time spread of electron trajectories through the analyzer. In principle, we can find \dot{N}_{FF} by taking the sum of the laser-on bins after subtracting off the background and dividing it by the total laser-on time T for the experiment.

$$\dot{N}_{FF} = \frac{1}{T} \sum_{i=1}^5 (y_i - N_{background}) = \frac{1}{T} \left(\binom{5}{\sum_{i=1}^5 y_i} - (5 N_{background}) \right) \quad (4.3)$$

where y_i is the number of counts in the i^{th} laser-on time bin. By Poisson statistics, the uncertainty of y_i is $\sqrt{y_i}$. $N_{background}$ has a negligible uncertainty (because N_{bins} in equation 4.2 is very large) compared to the uncertainty of the counts in a laser-on time bin. Thus, our free-free count rate is

$$\dot{N}_{FF} \pm \delta \dot{N}_{FF} = \frac{1}{T} \left(\binom{5}{\sum_{i=1}^5 y_i} - (5 N_{background}) \right) \pm \frac{1}{T} \sqrt{\binom{5}{\sum_{i=1}^5 y_i}}. \quad (4.4)$$

4.2 Determination of the Elastic and Inelastic Scattering Intensities

To find the relative cross section (see equation 2.67), we require the total elastic and inelastic scattering rates. As stated in section 3.5.3, due to dead-time effects, the NIM unit is used to measure the count rate in the scattering peaks rather than the STROBE of the PSD. However, some scattering peaks are intense enough where there are still significant dead-time effects. To overcome this, we used a method that intentionally detuned the first electrostatic lens (which I will now refer to as the *first lens*) of the scattered-electron detector. By intentionally detuning the first lens (by changing its electric potential), we adjust the trajectory of the electrons entering the detector. Detuning the first lens only reduced the number of electrons that reaches the analyzer and the electron energy-loss spectrum did not shift in energy. Figure 4.3 shows the elastic peak at various detunings of the first lens.

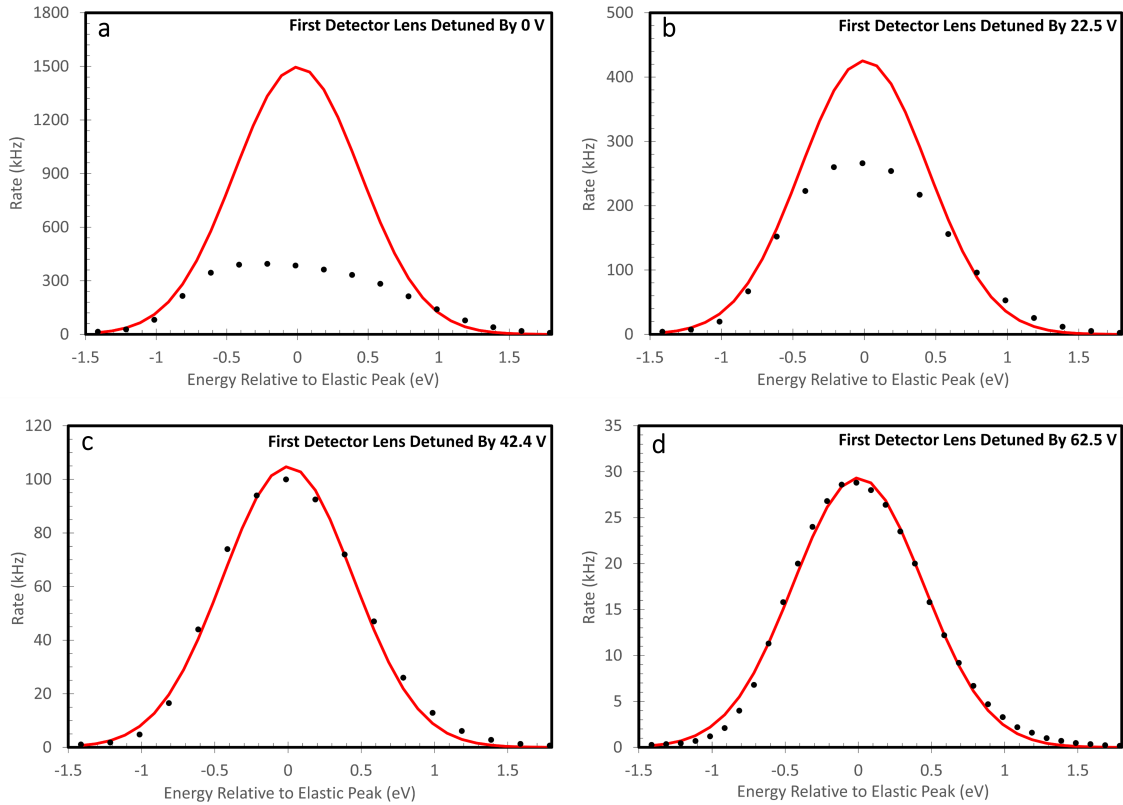


Figure 4.3: Elastic-scattering peak profile for different detunings of the first lens of the scattered-electron detector. The black dots are count rates measured on the NIM unit. The red curve is a Gaussian curve whose profile (spread and peak location) were determined when the first lens was detuned by 62.5 V. The Gaussian curve corresponds to an energy full-width, half max (FWHM) of 1.05 eV.

In figure 4.3, when the first lens is not detuned, the shape of the peak is a plateau. When the count rate is reduced by detuning the first lens by 22.5 V, the plateau is less apparent. However, when the first lens is detuned by more than 42.4 V, the shape of

the peak appears to be a Gaussian curve, as expected. By curve-fitting a Gaussian to the 62.5 V detuned data using least-squares fit in Mathematica[85, 86, 87], the correct profile of the scattering peak (its peak location and spread) was determined. The spread of the profile corresponds to an energy full-width at half-maximum (FWHM) of 1.05 eV. Count rates above 150 kHz produces significant dead-time effects, thus we fit our 1.05 eV FWHM Gaussian curve to the other detunings in figure 4.3, but only using data points in the wings below 150 kHz². The scaling was determined using Mathematica[85].

Figure 4.3 shows that detuning the first lens does not distort the energy profile of the elastic-scattering peak. However, fitting a Gaussian curve to the wings of the plateaued peaks is not accurate enough to obtain the true total elastic-scattering count rate, and we therefore used the following indirect method.

We used a *feature* of the energy-loss spectrum where dead-time effects are not expected when the detector is both tuned and detuned. We used an inelastic scattering peak (the unresolved 2¹S and 2¹P scattering peak) to find the count rate of the elastic scattering peak. The following was used:

$$\dot{N}_{el}(deduced) = \frac{\dot{N}_{inel}(tuned)}{\dot{N}_{inel}(detuned)} \times \dot{N}_{el}(detuned). \quad (4.5)$$

To test this method, we carried out experiments for count rates where we can measure both the tuned and detuned count rates directly.

These measurements comparing the count rate of the inelastic scattering peak when the detector are tuned and detuned is shown in figure 4.2. The data is also fitted with a linear model. We found that the *tuned/detuned* ratio is 40.3 ± 0.8 . Since the change in scale of the spectrum is due to detuning an electron optics lens of the scattered-electron detector, we expect this ratio to hold for all scattering angles. We assume the linear relationship holds for detuned count rates above 4 kHz, i.e., for tuned count rates above 150 kHz. This is a reasonable assumption provided that detuning does not cause charging of the electron lenses. We saw no evidence of such effects. Figure 4.3 also supports this argument.

Then the count rate for scattering peaks greater than 150 kHz can be found with the following relationship:

$$(\dot{N}_{el} \pm \delta\dot{N}_{el})_{deduced} = (40.3 \pm 0.8) \times (\dot{N}_{el} \pm \delta\dot{N}_{el})_{detuned} \quad (4.6)$$

$$(\dot{N}_{inel} \pm \delta\dot{N}_{inel})_{deduced} = (40.3 \pm 0.8) \times (\dot{N}_{inel} \pm \delta\dot{N}_{inel})_{detuned} \quad (4.7)$$

If the scattering peak count rate was below 150 kHz, then this method is not used and the rate is instead measured directly. Using the indirect method, we could measure elastic peak count rates as high as 11 million counts per second (the count rates in the wings, one photon energy away from the elastic scattering peak were, of course, much lower).

²Only 8 out of 17 data points in figure 4.3a, and 10 out of 17 in figure 4.3b had count rates under 150 kHz.

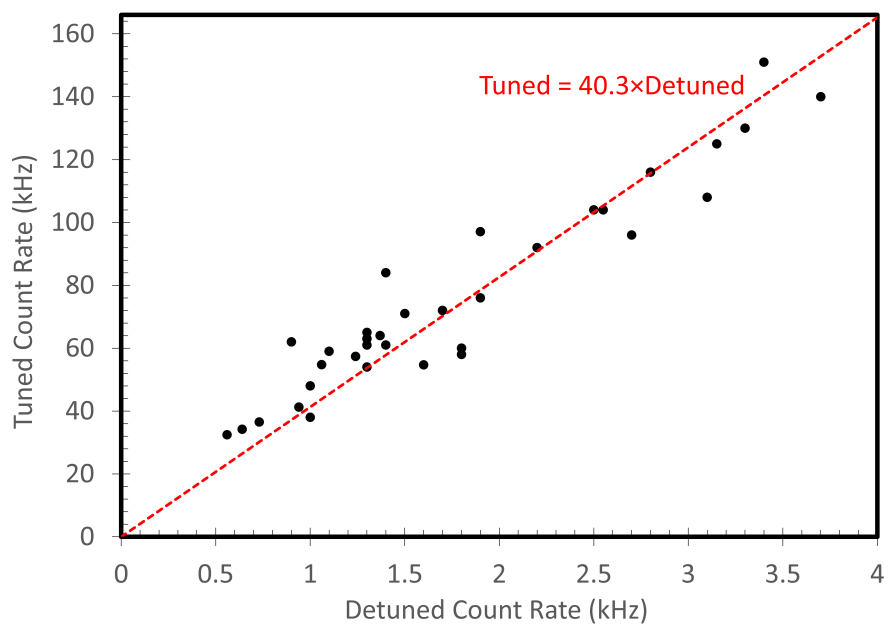


Figure 4.4: A comparison of the count rate measured when the detector is tuned and detuned. A linear model was fitted to the data.

4.3 Relative Cross Section

The free-free rate is given by equation 4.4 and the field-free peak scattering rate can be measured directly or indirectly using equation 4.6 and 4.7. One can then find the relative cross section by dividing the two quantities. However, there are still experimental factors that must be considered. Specifically, the PSD has dead-time effects even when the detector is off-the-peak and additional free-free electrons contributed from other parts of the spectrum.

4.3.1 PSD Dead-Time Effects

As stated in section 3.5.1, there is a known dead-time of $4 \mu\text{s}$ due to the signal processing of the PSD. However, this is a lower limit since there are unaccounted sources of dead-time effects, such as the “recharge” time of the MCPs. To characterize the effective dead-time of the PSD, we compare the STR and NIM count rates in a region where the NIM is believed to have negligible dead-time effects. We can reduce the count rate by detuning the first lens of the scattered-electron detector. Our results are shown in figure 4.5. If the PSD had negligible dead-time effects, we would expect all measured points to lie on the blue dashed-line. However, we can see dead-time effects for the STR count rates as low as 35 kHz. A model that relates the *actual count rate* \dot{N}_{actual} to the observed count rate $\dot{N}_{observed}$ due to a non-paralyzable, effective dead-time τ is

$$\dot{N}_{actual} = \frac{\dot{N}_{observed}}{1 - \tau \dot{N}_{observed}}. \quad (4.8)$$

By performing a least-squares fit on our NIM vs STR count rate data, we found an effective dead-time of $\tau = 5.50 \mu\text{s}$ with an uncertainty of $0.15 \mu\text{s}$, a negligible uncertainty. The red solid-line in figure 4.5 is equation 4.8 for a dead-time of $5.50 \mu\text{s}$.

Since every scattering event can be considered random, dead-time effects should not affect the signal-to-background ratio. We find a correction factor ξ to account for the electrons not detected due to dead-time effects of the PSD by taking a ratio of the actual count rate \dot{N}_{actual} to the STR (observed) count rate \dot{N}_{STR}

$$\text{PSD Dead-time Correction Factor} = \xi = \frac{\dot{N}_{actual}}{\dot{N}_{STR}} = \frac{1}{1 - ((5.50 \pm 0.15) \times 10^{-6} \text{ s}) \dot{N}_{STR}}. \quad (4.9)$$

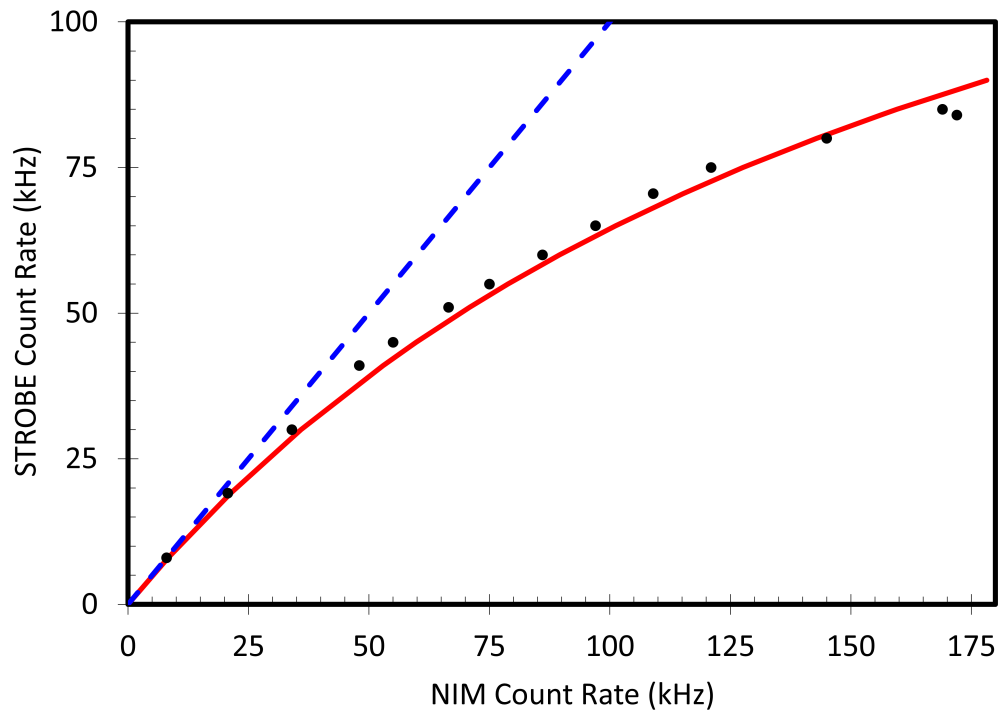


Figure 4.5: The black dots are the measured STR vs. NIM count rates. The blue dashed-line assumes the STR count rate had no dead-time effects while the red solid-line assumes a $5.50 \mu\text{s}$ dead-time.

4.3.2 Additional Free-Free Transition Corrections

In our elastic scattering experiments, we looked for free-free electrons that absorbed or emitted a photon when scattered in the presence of the laser field. We did so by setting the pass-energy of our detector to be one photon energy (1.17 eV) greater or less than the pass-energy to detect the scattering peak. However, as one can see in figure 4.3, due to the FWHM of the scattering peak profile being 1.05 eV, we were looking for free-free electrons while sitting at the *wings* of the scattering peak. In figure 4.1, the intensity of the scattering peak decreases in the presence of the laser field due to free-free transitions. Let us find the free-free rate accounting for the decrease in the intensity of the wings by following a similar derivation by deHarak *et al.*[32].

We use the the same variables used in section 4.1. Let $\dot{N}_{FF}^{(n)}$ be the free-free rate for the n photon(s) processes. The ratio of Q and R in figure 4.1 corresponds to the ratio of the count rate in the wing \dot{N}_{wing} to the count rate at the apex of the scattering peak \dot{N}_{peak} . The reduction of the laser-on wing count rate is $\frac{\dot{N}_{wing}}{\dot{N}_{peak}} \sum_{|n|>0} \dot{N}_{FF}^{(n)}$. Then we have the following relationship

$$\frac{1}{T} \sum_{i=1}^5 y_i = \dot{N}_{FF}^{(1)} + \frac{1}{T} \sum_{j=1}^5 N_{background} - \frac{\dot{N}_{wing}}{\dot{N}_{peak}} \sum_{|n|>0} \dot{N}_{FF}^{(n)} \quad (4.10)$$

where T is laser-on time of an experiment. The LHS of equation 4.10 is total scattering rate detected in the laser-on bins.

Let us assume that only one photon processes are significant. Then we find

$$\dot{N}_{FF}^{(1)} = \frac{1}{1 - 2\frac{\dot{N}_{wing}}{\dot{N}_{el}}} \left(\frac{1}{T} \left(\left(\sum_{i=1}^5 y_i \right) - (5 N_{background}) \right) \right). \quad (4.11)$$

When compared to equation 4.4, we see

$$\text{Background Correction Factor} = \frac{1}{1 - 2\frac{\dot{N}_{wing}}{\dot{N}_{el}}} \quad (4.12)$$

Then the experimental relative free-free cross section, including PSD dead-time effects is

$$\boxed{\frac{d\sigma_{FF}}{d\Omega} / \frac{d\sigma_{el}}{d\Omega} = \xi \frac{\dot{N}_{FF}^{(1)}}{(\dot{N}_{el} - 2\dot{N}_{wing})}}. \quad (4.13)$$

In elastic LAFF experiments, we use equation 4.13, however, due to $\dot{N}_{el} \gg \dot{N}_{wing}$, the correction is negligible. For inelastic processes, similar considerations apply but due the complexity of overlapping scattering peaks (the wings are not isolated), equation 4.13 cannot be applied. However, since the correction is negligible for elastic processes, we expect the same to hold for inelastic processes.

4.4 Correcting for Laser Intensity Variations and Other Effects

We noticed time-dependent variations in our experimental results from preliminary work. These variations occurred slowly enough so their effect on individual experiments is negligible. However, when series of experiments over a long time period are needed, such as for an angular distribution, these variations are a concern. To characterize the time-dependent variations, several one photon free-free experiments of elastically scattered electrons at a scattering angle of 45° were performed periodically during this work. Between scattering angles 0° and 90° , KWA predicts the maximum at 45° for relative cross sections, which enables good counting statistics to be achieved in a relatively short time.

As stated in section 3.6.1, one source of time-dependent variations is flash lamp degradation. As the flash lamps degrade, the laser intensity at the interaction region is reduced. In this work, flash lamps were changed once. We refer to the first set of flash lamps as *old* and the second set as *new*. Figure 4.6 shows the results of these experiments and quadratic curves were fitted to the data as a function of experiment number \mathcal{M} , one for the old flash lamps $F_{old}(\mathcal{M})$, and one for the new flash lamps $F_{new}(\mathcal{M})$. The old flash lamps had been in use for two months prior to the data collection for this work. These two curves were used to normalize the relative cross sections of the angular distribution experiments.

It can be seen in figure 4.6 that $F_{old}(\mathcal{M})$ and $F_{new}(\mathcal{M})$ do not exhibit behavior that one would expect for decaying flash lamps. For the old flash lamps, the relative cross section increased with time, which would suggest laser intensity increased. When the flash lamps were replaced, the relative cross sections increased significantly but continued to increase before it sharply decreased. Several experiments with the old flash lamps had very small statistical uncertainties but fluctuated with respect to time despite regular tuning to minimize other factors that could affect the laser intensities, such as the alignment of the mirror in the oscillator cavity. Thus, these time-dependent variations are not solely due to flash lamps decay. The origin of the uncertainty is unknown.

Potential sources for this unknown uncertainty may include the instability of the climate in our laboratory that could affect the stability of our laser path resulting in a slight misalignment between the electron-helium interaction region and the laser (the laser to interaction region distance is about two meters and the interaction region has a diameter of 0.75 mm). Also, the elastic scattering cross section varies by two orders of magnitude between the scattering angles 0° and 90° [64]. We therefore had to retune the electron gun at smaller scattering angles to have reasonable count rates in the wings of the peak where we run our experiments. The gun was retuned again when we returned to higher scatterings (such as 45°). These retunings may have introduced additional uncertainties.

In order to account for them, we can find an uncertainty based on the *scatter* of the data points from their respective curve. This resulted in an uncertainty of $\pm 21\%$ for the old flash lamps and $\pm 15\%$ for the new flash lamps. We refer to this as the *uncertainty of the apparatus* and can be seen in figure 4.6 as the blue dashed-line. We will at present proceed under the assumption that they are uncorrelated and of

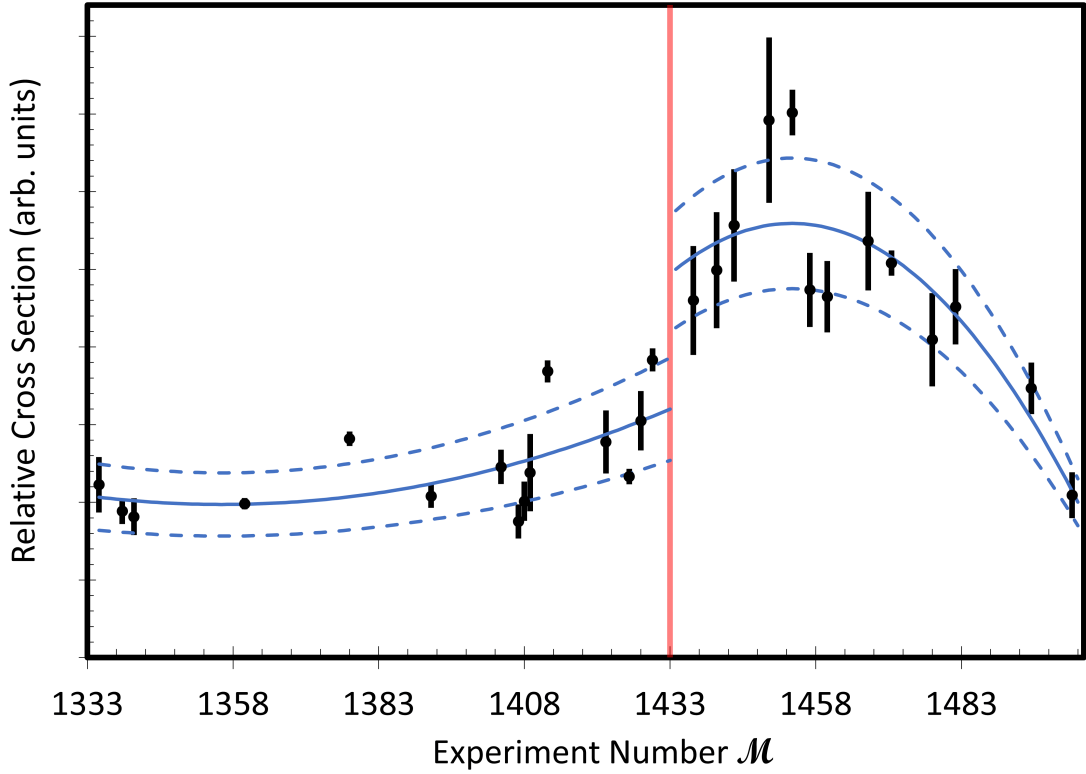


Figure 4.6: Time-dependent variations of relative cross sections (black dots) for one photon free-free processes of elastically scattered electrons from helium at a scattering angle of 45° . Experiment number \mathcal{M} is a chronological identifier given to experiments. The red vertical line is when the laser flash lamps were replaced. Experiments left of the vertical line (old flash lamps) were taken over a four months period while the ones on the right (new flash lamps) were taken over a two-and-half month period. The blue curves are quadratic fits, $F_{old}(\mathcal{M})$ and $F_{new}(\mathcal{M})$, to the data for the old and new flash lamps, respectively. The dashed-lines represent the *uncertainty of the apparatus* from unknown sources, found from the scatter of the data.

a statistical nature.

4.5 Angular Distributions

Here we present the angular distributions (the angular behavior of $\frac{d\sigma_{FF}}{d\Omega} / \frac{d\sigma_{el/inel}}{d\Omega}$, see equation 2.66) for elastic and inelastic electron-helium scattering in an Nd:YAG laser field. When multiple similar experiments (at a given angle) were combined, the method of weighted averages was used. Each angular distribution was fitted with the KWA whose scaling was determined by minimizing the χ^2 between it and its respective experimental data. A $\tilde{\chi}^2$ test was used to determine *goodness-of-fit* (see Appendix A for more information on weighted averages, χ^2 , and the $\tilde{\chi}^2$ test). The scales in the figures are normalized to the KWA elastic cross section at 45° .

4.5.1 Elastic Free-Free Angular Distribution

The elastic free-free angular distribution is comprised of relative cross sections at scattering angles 15° , 25° , 35° , 45° , 57° , 67.5° , and 80° . The one photon emission and absorption data were essentially the same (as expected), and were therefore combined to improve the statistics. The distribution is shown in figure 4.7. When compared to KWA, it has a goodness-of-fit of $\tilde{\chi}^2 = 2.1$. Thus, the experimental data is described quite well by the KWA.

Scattering Angle	Relative Cross Section (arb. units)
15°	0.21 ± 0.05
25°	0.41 ± 0.10
35°	0.84 ± 0.09
45°	1.02 ± 0.04
57°	0.95 ± 0.15
67.5°	0.91 ± 0.11
80°	0.33 ± 0.13

Table 4.1: The elastic free-free relative cross sections for various scattering angles. These values are plotted on figure 4.7. All experiments were normalized to the KWA that was fitted to the elastic free-free data.

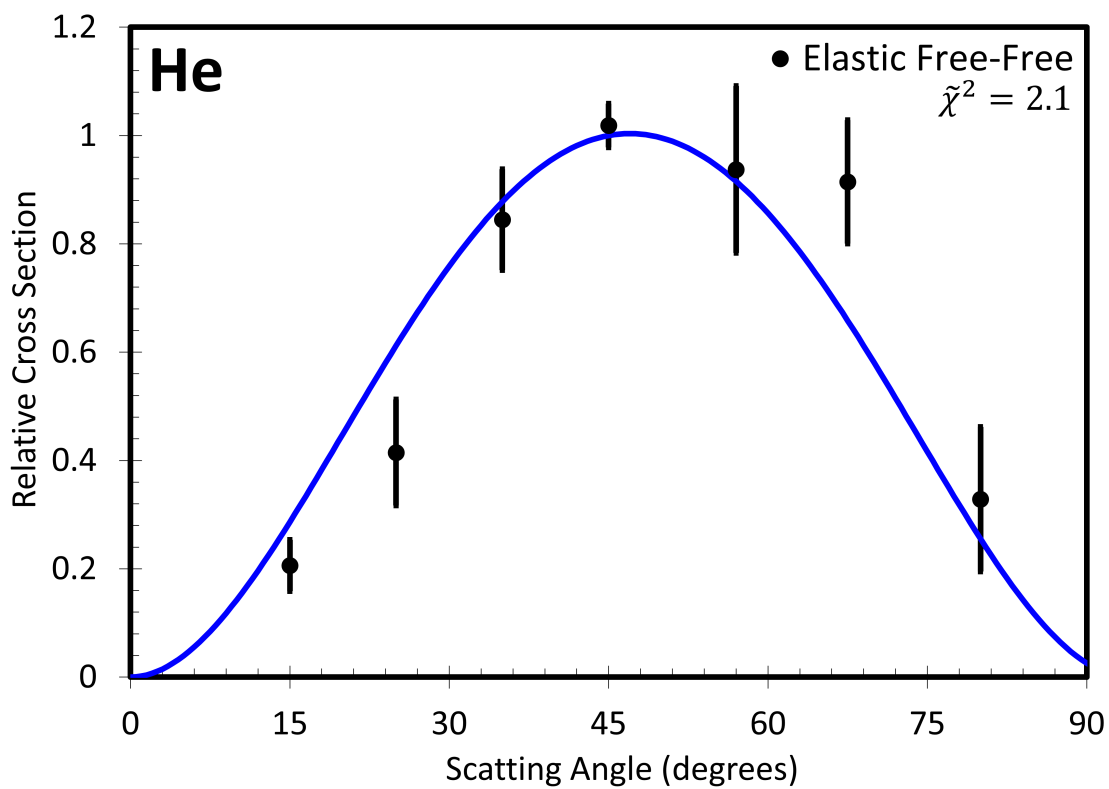


Figure 4.7: Elastic free-free angular distribution for one photon processes (black dots) with the Kroll-Watson approximation fitted to the data (blue solid-line) and then normalized. It has a $\tilde{\chi}^2 = 2.1$.

4.5.2 Inelastic Free-Free Angular Distribution

Our inelastic free-free experiments involve electron-impact excitation from the ground state of helium to the unresolved excited states 2^1S and 2^1P in the presence of a laser field. At high incident electron energies, exchange effects are small and singlet-singlet scattering processes predominate. Figure 4.8 shows the excited state energies and separation. The electron energy-loss spectrum with a resolution of 1.05 eV, taken in our laboratory, is shown in figure 4.9. The most intense peak in our spectrum is comprised of the unresolved 2^1S and 2^1P excited states of helium. A larger background for inelastic free-free scattering experiments (see vertical arrows in figure 4.9) is a consequence of having a broader scattering peak.

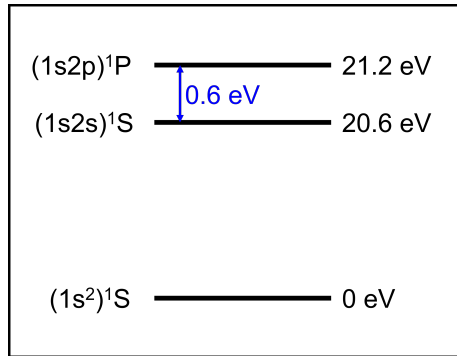


Figure 4.8: The three energy states of helium using in this work. Not shown are the $(1s2s)^3S$ and $(1s2p)^3P$ states of helium. Due to the dominance of singlet-singlet scattering processes for high incident electron energies, their contributions are negligible compared to the $(1s2s)^1S$ and $(1s2p)^1P$ states. Energy levels from [70].

Our experimental inelastic free-free angular distribution is comprised of relative cross sections at scattering angles 1° , 2° , 4° , 5° , 10° , 15° , 20° , 25° , 35° , 45° , 57° , 67.5° , and 80° , see figure 4.10. The emission, and absorption, relative free-free cross sections agree within statistics, and were therefore combined to reduce the uncertainties. (Note that the 15° data point only includes emission: the absorption experiment detected no signal and was clearly an outlier.)

In figure 4.10, the red dashed-line is the inelastic KWA fitted to the experimental data. This fit has $\tilde{\chi}^2$ of 1.9 and would seem to indicate that the KWA is a good description of our data. However, the green chained-line in the figure is a calculation of the angular distribution expected for inelastic processes relative to the normalized elastic fit shown in figure 4.7. Thus, the KWA predicts that the inelastic intensities should be about 80% of the elastic intensities due to the momentum transfer magnitude and direction for a 21.2 eV energy loss for 350 eV incident electrons. In fact, the green chained-line has $\tilde{\chi}^2 = 2.5$ for the experimental data. This $\tilde{\chi}^2$ value is similar to the elastic free-free fit in figure 4.7. Clearly, further experiments with better uncertainties are desirable to resolve this conundrum.

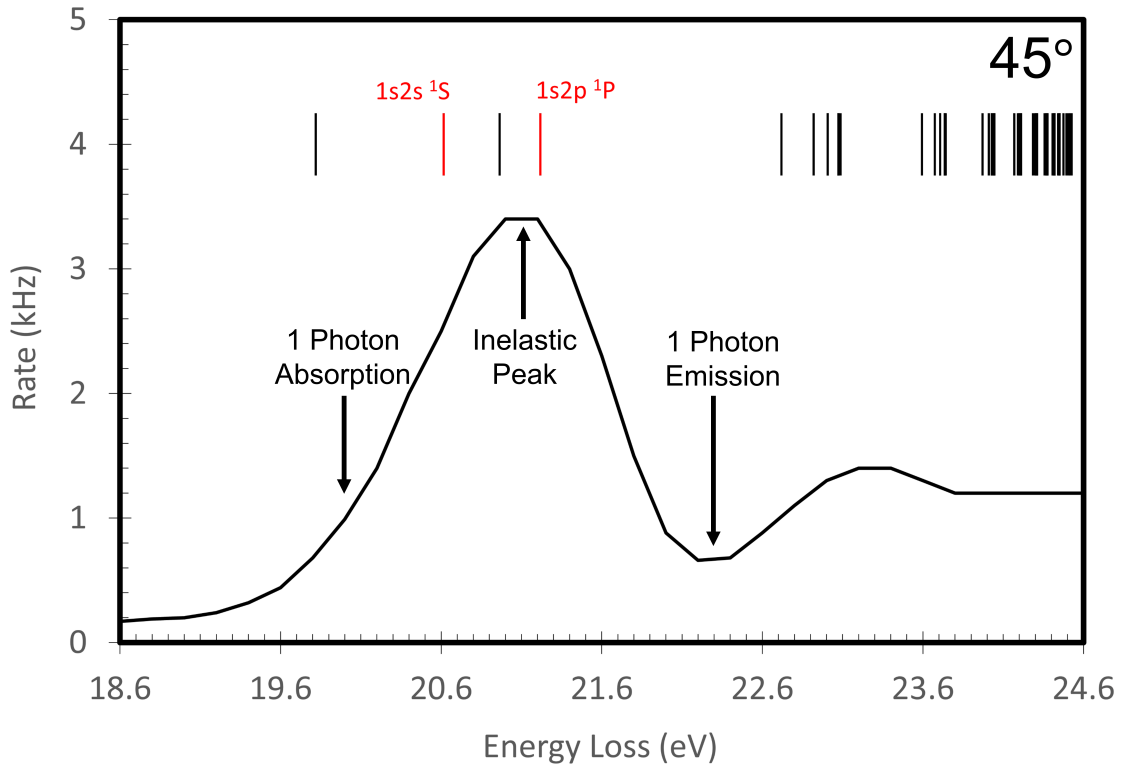


Figure 4.9: Electron energy-loss spectrum due to the excited states of helium at a scattering angle of 45° . The largest peak is what we refer to as the *inelastic peak*. It is predominately made up of the $(1s2s)^1S$ and $(1s2p)^1P$ scattering peaks (in red). Energy states (vertical lines) are from [70]. The location of the inelastic scattering peak, one photon absorption, and one photon emission are labeled.

Scattering Angle	Relative Cross Section (arb. units)
1°	0.037 ± 0.035
2°	0.018 ± 0.006
4°	0.094 ± 0.109
5°	0.068 ± 0.118
10°	0.11 ± 0.11
15°	0.77 ± 0.24
20°	0.75 ± 0.22
25°	0.85 ± 0.28
35°	1.2 ± 0.3
45°	1.1 ± 0.3
57°	1.0 ± 0.2
67.5°	0.36 ± 0.15
80°	0.29 ± 0.33

Table 4.2: The inelastic free-free relative cross sections for various scattering angles. These values are plotted on figure 4.10. All experiments were normalized to the curves that were fitted to the elastic free-free data for a scattering angle of 45°.

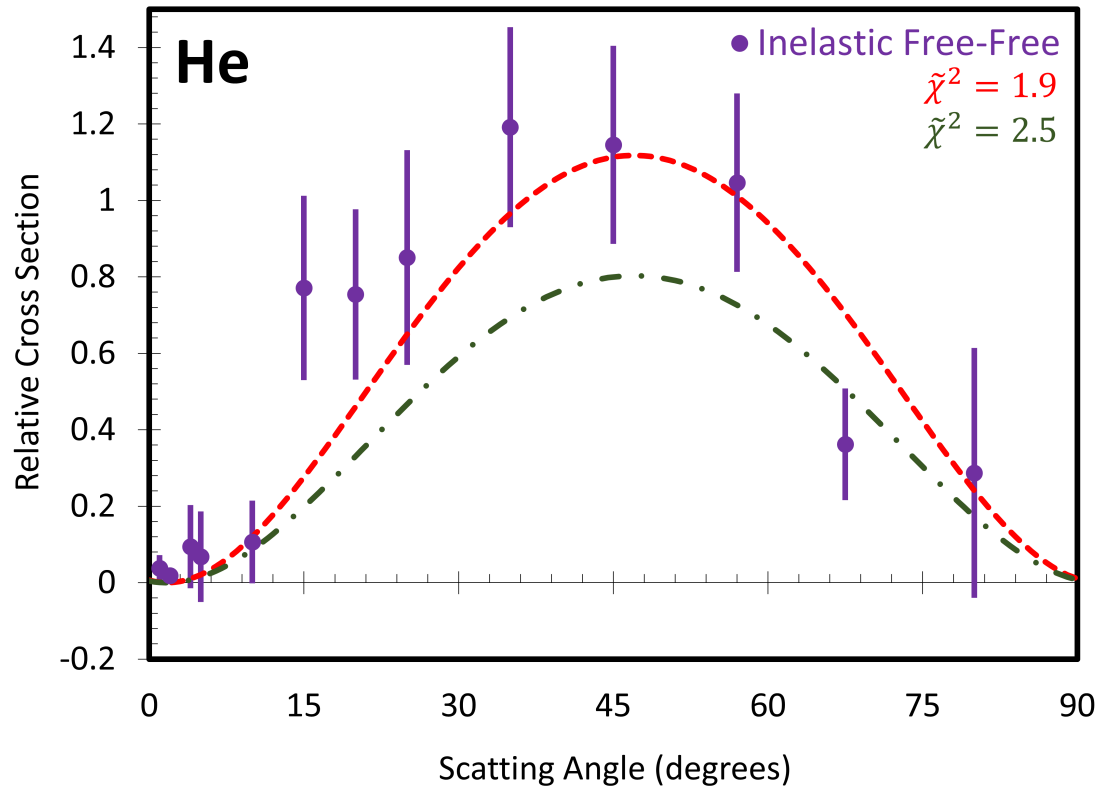


Figure 4.10: Inelastic LAFF angular distribution for one photon processes (purple dots). The red dashed-line is the the Kroll-Watson approximation that was fitted to our data with $\tilde{\chi}^2 = 1.9$. The green chained-line is the predicted inelastic KWA based on the elastic free-free data. It has a $\tilde{\chi}^2 = 2.5$.

4.5.3 Reanalyzed: Uncertainty of Apparatus

As stated at the end of section 4.4, the uncertainty of the apparatus was assumed to be uncorrelated and of a statistical nature. However, the origin of the uncertainty in the laser intensity plot (figure 4.6) is unknown and may not be purely statistical. Thus, it is not clear if it should be added in quadrature. We have therefore repeated the analysis assuming it should not be added in quadrature (i.e., the uncertainty should be added linearly). When this is done, we obtain two new figures for the elastic and inelastic angular distribution and the $\tilde{\chi}^2$ for both are dramatically lowered. For the elastic angular distribution (figure 4.11), a reduced chi-squared of 2.1 is lowered to 1.3. For the inelastic angular distribution (figure 4.12), a reduced chi-squared of 1.9 is lowered to 1.1 when compared to the red curve, and a reduced chi-squared of 2.5 is lowered to 1.3 when the data is compared to the green curve. This seems to indicate the data may, in fact, be consistent with the calculated inelastic KWA.

Scattering Angle	Relative Cross Section (arb. units)
15°	0.21 ± 0.07
25°	0.42 ± 0.12
35°	0.84 ± 0.12
45°	1.02 ± 0.05
57°	0.95 ± 0.20
67.5°	0.91 ± 0.14
80°	0.33 ± 0.19

Table 4.3: The elastic free-free relative cross sections with the uncertainty of the apparatus being added linearly for various scattering angles. These values are plotted on figure 4.11. See table 4.1 for details of the normalization.

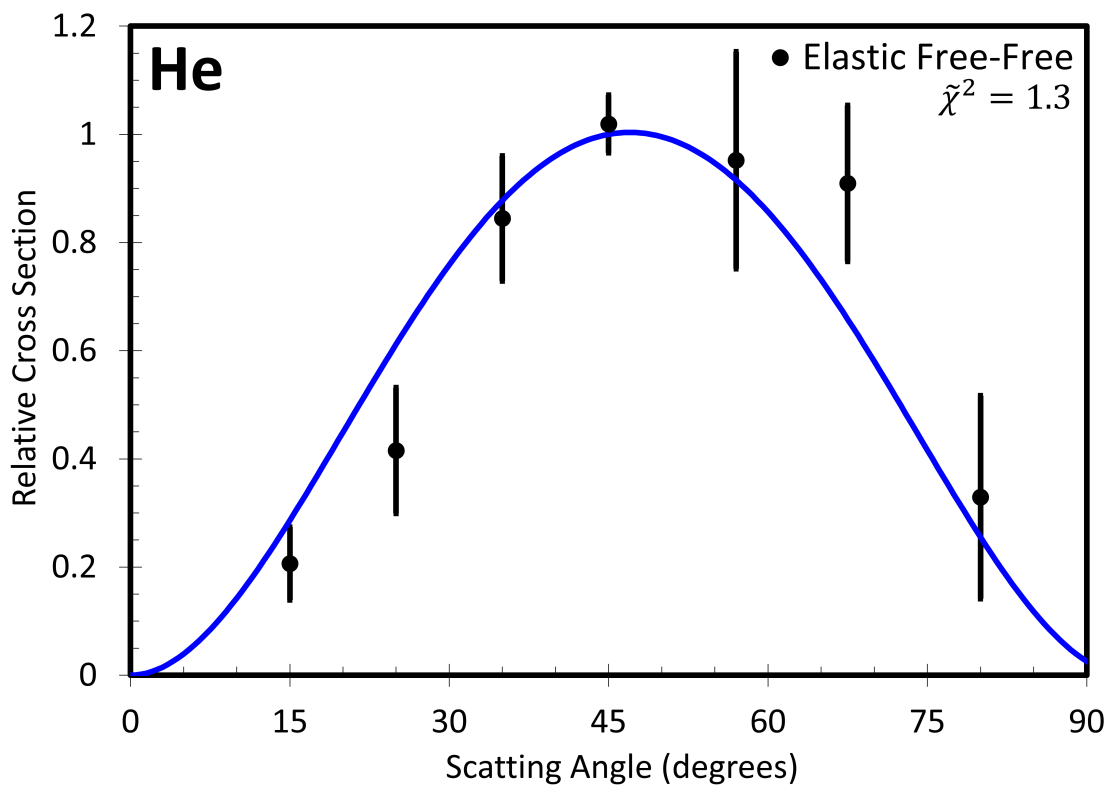


Figure 4.11: Elastic free-free angular distribution with the uncertainty of the apparatus being added linearly rather than in quadrature.

Scattering Angle	Relative Cross Section (arb. units)
1°	0.038 ± 0.044
2°	0.014 ± 0.007
4°	0.094 ± 0.120
5°	0.068 ± 0.132
10°	0.11 ± 0.13
15°	0.77 ± 0.34
20°	0.76 ± 0.31
25°	0.85 ± 0.40
35°	1.2 ± 0.4
45°	1.1 ± 0.4
57°	1.0 ± 0.3
67.5°	0.31 ± 0.19
80°	0.23 ± 0.37

Table 4.4: The inelastic free-free relative cross sections with the uncertainty of the apparatus being added linearly for various scattering angles for various scattering angles. These values are plotted on figure 4.12. All experiments were normalized to the curves that were fitted to the elastic free-free data for a scattering angle of 45°.

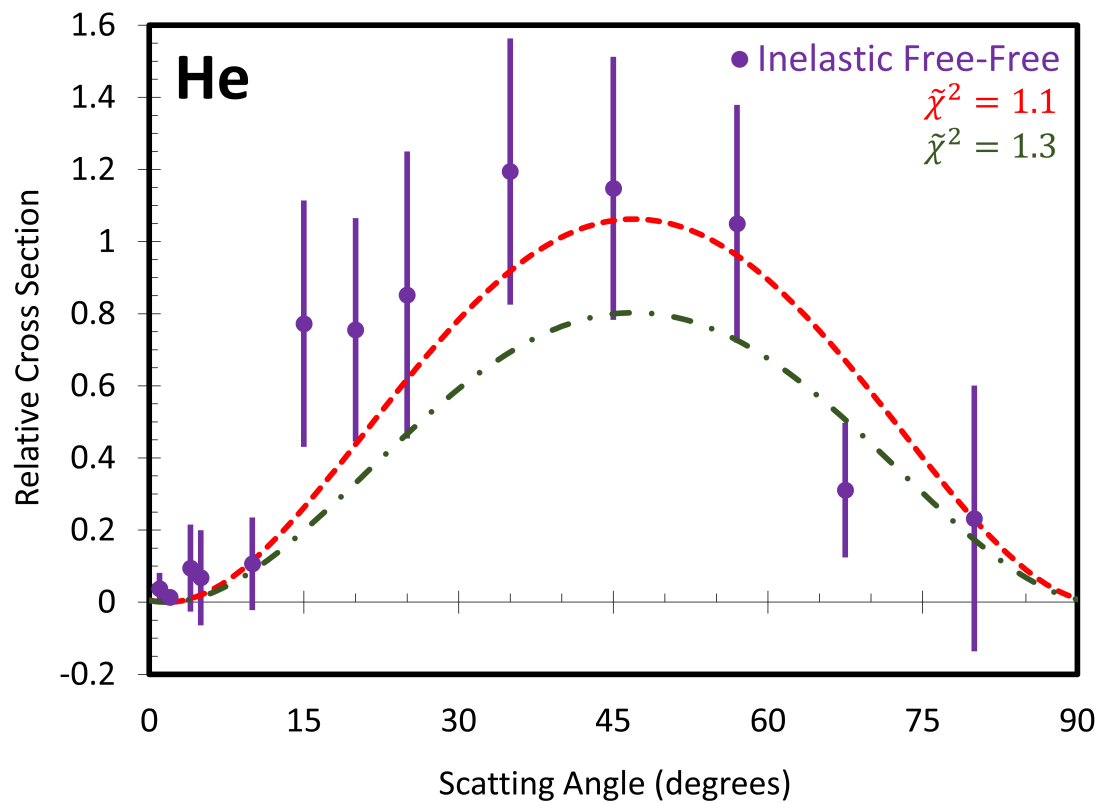


Figure 4.12: Inelastic free-free angular distribution with the uncertainty of the apparatus being added linearly rather than in quadrature.

Copyright© Brian N Kim, 2022.

Chapter 5 Summary and Conclusion

We have performed electron-helium scattering in an Nd:YAG laser field for various scattering angles between 1° to 80° . The electrons had an incident energy of 350 eV and the photons had an energy of 1.17 eV. Elastic laser-assisted free-free scattering is when an electron is elastically scattered by a helium atom in the presence of a laser field which allows the absorption or emission of one or more photons. In this work, what we refer to as inelastic laser-assisted free-free scattering is when a helium atom undergoes electron-impact excitation from its ground state to either its $(1s2s)^1S$ or $(1s2p)^1P$ excited energy states in the presence of a laser field. Similar to the elastic case, the electron will absorb or emit one or more photons of energy. In this work, we only focused on one photon processes (absorption and emission) of elastic and inelastic scattering. A theoretical model that is often compared with free-free experiments is the Kroll-Watson approximation (KWA). This model ignores the laser-atom interaction and at the soft-photon limit. Other theories, such as the Zon and our in-house model, included this interaction and predicts light-dressed atom effects to noticeably deviate from the KWA at small scattering angles for targets with high dipole polarizabilities.

To our knowledge, this is the first measurements of elastic and inelastic free-free angular distributions of helium with 350 eV incident electrons in an Nd:YAG laser field. Due to the unknown origin of the *uncertainty of the apparatus*, we analyzed our experimental results with this uncertainty added in quadrature, and also with this uncertainty being added linearly. The experimental results compared to the KWA for the former are shown in figures 4.7 and 4.10 and the latter are shown in figures 4.11 and 4.12. In all cases, the experimental data was consistent with the KWA, but the data was not accurate enough to reveal any possible deviations from the KWA. Thus, the present experiments cannot test the relationship between elastic and inelastic scattering of the KWA. Clearly, it would be desirable to repeat the experiments with a higher level of accuracy.

Our search for dressed-atom effects is inconclusive. Performing small angle scattering experiments is difficult due to the large background counts. At small scattering angles, the 2^1P contribution of the inelastic peak is an order of magnitude larger than the 2^1S [88], which is where light-dressing effects are expected to occur. As shown in figure 4.6, there are time-dependent variations and small angle experiments must be run over the course of days and possibly weeks. This causes some concerns about the stability of our apparatus during these long experiments.

To continue our investigation into the KWA and light-dressed atom effects, it is necessary to reduce the uncertainty of each data point. The uncertainty of the apparatus is our largest source of uncertainty. A method to better characterize and correct for these variations is necessary. We can follow a similar procedure performed in section 4.4 but the frequency of the normalization experiments should be increased and the experiment should be run long enough to obtain very small statistical uncertainty. Instead of normalization curves, we can normalize experiments directly to a

45° elastic free-free experiment.

We can also attempt to identify the specific sources of the uncertainty in our apparatus to minimize or correct them. We mentioned that a potential source of this unknown uncertainty may be due to the instability of the laboratory climate affecting the stability of our laser path. We can minimize the instability of our laser path by using a pair of *steering mirrors* and a pair of irises to define the laser path into the vacuum chamber. We can periodically check the laser path to see any shifts that may have occurred. The steering mirrors would allow us to correct the laser beam path if any deviations are observed. Additionally, the temperature and humidity of the laboratory should be monitored and note any correlation between the laser path deviation and temperature and humidity. It would be advantageous to monitor the degradation of the flash lamps independent of running experiments. A possible method could use a beamsplitter cube to “pick off” a tiny portion of the laser beam and into a photodiode to monitor the output power of the laser. In combination with monitoring the climate of the laboratory, we may find a correlation between the laser output with the temperature and humidity of the laboratory.

The effects of time-dependent variations can also be limited by reducing the time necessary to perform the experiments by reducing the background counts and by increasing our data-taking efficiency. A monochromated electron gun to resolve the 2^1S and 2^1P and a multipass laser system which traps the laser beam in a repetitive loop to increase the signal are currently being installed on our apparatus to accomplish this.

Appendices

Appendix A: Statistics

Here we will briefly discuss the relevant statistics definitions and relationships from Taylor[89].

Poisson Statistics

The Poisson distribution is used to describe counting experiments where the events occur randomly but at a definite average rate. This distribution is therefore suited for our experiments where we measure the rate of electrons detected. Any individual scattering event is random but there is a definite average scattering rate. The probability of observing ν events in some time interval T is

$$\text{Probability}(\nu \text{ counts in time interval } T) = P_\mu(\nu) = e^{-\mu} \frac{\mu^\nu}{\nu!} \quad (1)$$

where μ is the expected average number of events in time T . The standard deviation of observing ν events is

$$\sigma_\nu = \sqrt{\mu}. \quad (2)$$

The standard deviation of the observed number of events in the Poisson distribution is the square root of the observed number of events.

Weighted Averages

In this work, there are times when we measure the same physical quantity, but with varying uncertainties. To simply take the average gives equal importance to each measurement despite the size of their uncertainties. To combine multiple measurements together, we use weighted averages.

The i^{th} data point with an uncertainty σ_i is given a weight w_i that is defined as

$$w_i = \frac{1}{\sigma_i^2}. \quad (3)$$

The weighted average is

$$\bar{x}_{\text{weighted}} = \frac{\sum w_i x_i}{\sum w_i} \quad (4)$$

with the weighted uncertainty

$$\sigma_{\text{weighted}} = \frac{1}{\sqrt{\sum w_i}}. \quad (5)$$

The $\tilde{\chi}^2$ Test

Since we cannot measure the cross sections directly, we test the Kroll-Watson approximation (KWA) by fitting the model to our experimental data. We first define the χ^2 between the i^{th} observe value O_i with uncertainty σ_i to its corresponding expected value E_i . Then

$$\chi^2 = \sum_i^n \left(\frac{O_i - E_i}{\sigma_i} \right)^2 \quad (6)$$

where n is the number of data points.

To determine the scaling factor of the KWA, we minimize the χ^2 between the model and our data.

To determine the *goodness-of-fit* of our experimental data to KWA, we use the reduced χ^2 ($\tilde{\chi}^2$) defined as

$$\tilde{\chi}^2 = \frac{\chi^2}{d} \quad (7)$$

where d is the degrees of freedom. It is the number of data points n minus constraints. In our fit, only the scale factor of the model was determined by our experimental data. Thus, the degrees of freedom is $d = n - 1$. A “great fit” between data and a model is $\tilde{\chi}^2 \approx 1$ and a “good fit” is $\tilde{\chi}^2 \approx 2$ ¹. Anything larger would suggest a not so good fit between data and the model.

¹What is considered a “good fit” can be somewhat subjective.’

Bibliography

- [1] Mason, N. J. Laser-assisted electron-atom collisions. *Rep. Prog. Phys.* **56**, 1275 (1993).
- [2] Weingartshofer, A., Clarke, E. M., Holmes, J. K. & Jung, C. Experiments on multiphoton free-free transitions. *Phys. Rev. A* **19**, 2371–2376 (1979). URL <https://link.aps.org/doi/10.1103/PhysRevA.19.2371>.
- [3] Andrick, D. & Langhans, L. Measurement of the free-free cross section of e^- -ar scattering. *Journal of Physics B: Atomic and Molecular Physics* **11**, 2355–2360 (1978). URL <https://doi.org/10.1088/0022-3700/11/13/019>.
- [4] Morimoto, Y., Kanya, R. & Yamanouchi, K. Light-dressing effect in laser-assisted elastic electron scattering by Xe. *Phys. Rev. Lett.* **115**, 123201 (2015). URL <https://link.aps.org/doi/10.1103/PhysRevLett.115.123201>.
- [5] Mason, N. J. & Newell, W. R. Simultaneous electron-photon excitation of the helium 2^3S state. *Journal of Physics B: Atomic, Molecular and Optical Physics* **22**, 777–796 (1989). URL <https://doi.org/10.1088/0953-4075/22/5/009>.
- [6] Kanya, R. & Yamanouchi, K. Femtosecond laser-assisted electron scattering for ultrafast dynamics of atoms and molecules. *Atoms* **7** (2019). URL <https://www.mdpi.com/2218-2004/7/3/85>.
- [7] Pannekoek, A. The theoretical contours of absorption lines. *Monthly Notices of the Royal Astronomical Society* **91**, 139–169 (1930). URL <https://doi.org/10.1093/mnras/91.1.139>. <https://academic.oup.com/mnras/article-pdf/91/1/139/2855218/mnras91-0139.pdf>.
- [8] Stille, J. L. & Calaway, J. Free-free absorption coefficient of the negative hydrogen ion. *The Astrophysical Journal* **160**, 245 (1970).
- [9] Brantov, A. *et al.* Enhanced inverse bremsstrahlung heating rates in a strong laser field. *Physics of Plasmas* **10**, 3385–3396 (2003). URL <https://doi.org/10.1063/1.1586917>. <https://doi.org/10.1063/1.1586917>.
- [10] Shima, Y. & Yatom, H. Inverse bremsstrahlung energy absorption rate. *Phys. Rev. A* **12**, 2106–2117 (1975). URL <https://link.aps.org/doi/10.1103/PhysRevA.12.2106>.
- [11] Schlüter, D. Gaunt factors for free-free transitions in the fields of positive ions of carbon, nitrogen, and oxygen, calculated in the scaled thomas-fermi approximation. *Z. Phys. D* **11**, 273–276 (1989).
- [12] Kroll, N. M. & Watson, K. M. Charged-particle scattering in the presence of a strong electromagnetic wave. *Phys. Rev. A* **8**, 804–809 (1973). URL <https://link.aps.org/doi/10.1103/PhysRevA.8.804>.

- [13] Madsen, L. B. *STRONG FIELD DYNAMICS: Scattering and Multiphoton Ionization*. Ph.D. thesis, Institute of Physics and Astronomy, University of Aarhus (1998). URL https://phys.au.dk/fileadmin/site_files/publikationer/phd/Lars_Bojer_Madsen.pdf.
- [14] Martin, N. L. S., Weaver, C. M., Kim, B. N. & deHarak, B. A. Angular distribution of electrons elastically scattered from Ar in the presence of a 1.17 eV laser field. *Phys. Rev. A* **99**, 032708 (2019). URL <https://link.aps.org/doi/10.1103/PhysRevA.99.032708>.
- [15] Ehlotzky, F., Jaroń, A. & Kamiński, J. Z. Electron-atom collisions in a laser field. *Phys. Rep.* **297**, 63 (1998).
- [16] Andrick, D. & Langhans, L. Measurement of free-free transitions in e⁻-Ar scattering. *Journal of Physics B: Atomic and Molecular Physics* **9**, L459–L461 (1976). URL <https://doi.org/10.1088/0022-3700/9/15/006>.
- [17] Krüger, H. & Schulz, M. Laser-induced free-free electronic transitions near a resonance. *Journal of Physics B: Atomic and Molecular Physics* **9**, 1899–1910 (1976). URL <https://doi.org/10.1088/0022-3700/9/11/015>.
- [18] Geltman, S. Free-free radiation in electron-neutral atom collisions. *Quant. Spectrosc. Radiat. Transfer* **13**, 601 (1973).
- [19] Weingartshofer, A., Holmes, J. K., Caudle, G., Clarke, E. M. & Krüger, H. Direct observation of multiphoton processes in laser-induced free-free transitions. *Phys. Rev. Lett.* **39**, 269–270 (1977). URL <https://link.aps.org/doi/10.1103/PhysRevLett.39.269>.
- [20] Krüger, H. & Jung, C. Low-frequency approach to multiphoton free-free transitions induced by realistic laser pulses. *Phys. Rev. A* **17**, 1706–1712 (1978). URL <https://link.aps.org/doi/10.1103/PhysRevA.17.1706>.
- [21] Weingartshofer, A., Holmes, J. K., Sabbagh, J. & Chin, S. L. Electron scattering in intense laser fields. *Journal of Physics B: Atomic and Molecular Physics* **16**, 1805–1817 (1983). URL <https://doi.org/10.1088/0022-3700/16/10/016>.
- [22] Bader, H. Measurement of the free-free cross section of e–Ar scattering at $\lambda_0=5.3\mu\text{m}$. *Journal of Physics B: Atomic and Molecular Physics* **18**, L235–L237 (1985). URL <https://doi.org/10.1088/0022-3700/18/8/005>.
- [23] Wallbank, B., Holmes, J. K. & Weingartshofer, A. Experimental differential cross sections for multiphoton free-free transitions. *Journal of Physics B: Atomic and Molecular Physics* **20**, 6121–6138 (1987). URL <https://doi.org/10.1088/0022-3700/20/22/021>.
- [24] Wallbank, B., Connors, V. W., Holmes, J. K. & Weingartshofer, A. Experimental differential cross sections for one-photon free-free transitions. *Journal of Physics*

- B: Atomic and Molecular Physics* **20**, L833–L838 (1987). URL <https://doi.org/10.1088/0022-3700/20/24/002>.
- [25] Wallbank, B. & Holmes, J. K. Differential cross sections for laser-assisted elastic electron scattering from argon. *Journal of Physics B: Atomic, Molecular and Optical Physics* **27**, 5405–5418 (1994). URL <https://doi.org/10.1088/0953-4075/27/21/027>.
- [26] Wallbank, B. & Holmes, J. K. Laser-assisted elastic electron-atom collisions. *Phys. Rev. A* **48**, R2515–R2518 (1993). URL <https://link.aps.org/doi/10.1103/PhysRevA.48.R2515>.
- [27] Wallbank, B. & Holmes, J. K. Laser-assisted elastic electron-atom collisions: low electron energy and small scattering angle. *Journal of Physics B: Atomic, Molecular and Optical Physics* **27**, 1221–1231 (1994). URL <https://doi.org/10.1088/0953-4075/27/6/020>.
- [28] Wallbank, B. & Holmes, J. K. Low-energy electron - helium scattering in a laser field. *Journal of Physics B: Atomic, Molecular and Optical Physics* **29**, 5881–5887 (1996). URL <https://doi.org/10.1088/0953-4075/29/23/027>.
- [29] Wallbank, B. & Holmes, J. K. Laser-assisted elastic electron scattering from helium. *Can. J. Phys.* **79**, 1237 (2001).
- [30] Nehari, D., Holmes, J., Dunseath, K. M. & Terao-Dunseath, M. Experimental and theoretical study of free–free electron–helium scattering in a CO₂ laser field. *Journal of Physics B: Atomic, Molecular and Optical Physics* **43**, 025203 (2010). URL <https://doi.org/10.1088/0953-4075/43/2/025203>.
- [31] Musa, M. O., MacDonald, A., Tidswell, L., Holmes, J. & Wallbank, B. Laser-induced free–free transitions in elastic electron scattering from CO₂. *Journal of Physics B: Atomic, Molecular and Optical Physics* **43**, 175201 (2010). URL <https://doi.org/10.1088/0953-4075/43/17/175201>.
- [32] deHarak, B. A., Ladino, L., MacAdam, K. B. & Martin, N. L. S. High-energy electron-helium scattering in a Nd:YAG laser field. *Phys. Rev. A* **83**, 022706 (2011). URL <https://link.aps.org/doi/10.1103/PhysRevA.83.022706>.
- [33] deHarak, B. A., Nosarzewski, B., Siavashpouri, M. & Martin, N. L. S. Electron-helium scattering in a 1.17 eV laser field: The effect of polarization direction. *Phys. Rev. A* **90**, 032709 (2014). URL <https://link.aps.org/doi/10.1103/PhysRevA.90.032709>.
- [34] deHarak, B. A. *et al.* Effects of polarization direction on laser-assisted free–free scattering. *Plasma Sources Science and Technology* **25**, 035021 (2016). URL <https://doi.org/10.1088/0963-0252/25/3/035021>.

- [35] Martin, N. L. S. & deHarak, B. A. Test of target independence for free-free scattering in a Nd:YAG laser field. *Phys. Rev. A* **93**, 013403 (2016). URL <https://link.aps.org/doi/10.1103/PhysRevA.93.013403>.
- [36] Kanya, R., Morimoto, Y. & Yamanouchi, K. Observation of laser-assisted electron-atom scattering in femtosecond intense laser fields. *Phys. Rev. Lett.* **105**, 123202 (2010). URL <https://link.aps.org/doi/10.1103/PhysRevLett.105.123202>.
- [37] Morimoto, Y., Kanya, R. & Yamanouchi, K. Light-dressing effect in laser-assisted elastic electron scattering by Xe. *Phys. Rev. Lett.* **115**, 123201 (2015). URL <https://link.aps.org/doi/10.1103/PhysRevLett.115.123201>.
- [38] Zon, B. A. Bremsstrahlung in collisions between electrons and atoms. *Sov. Phys. JETP* **46**, 65 (1977).
- [39] Morimoto, Y., Kanya, R. & Yamanouchi, K. *Phys. Rev. Lett.* **115**, 123201 (2015). Supplemental material.
- [40] Mason, N. J. & Newell, W. R. Simultaneous electron-photon excitation of the helium 2^3S state. *Journal of Physics B: Atomic and Molecular Physics* **20**, L323–L325 (1987). URL <https://doi.org/10.1088/0022-3700/20/10/006>.
- [41] Wallbank, B., Holmes, J. K., LeBlanc, L. & Weingartshofer, A. Simultaneous off-shell excitation of He 2^3s by an electron and one or more photons. *Z. Phys. D* **10**, 467 (1989).
- [42] Geltman, S. & Maquet, A. Laser-assisted electron-impact atomic excitation in the soft-photon limit. *Journal of Physics B: Atomic, Molecular and Optical Physics* **22**, L419–L425 (1989). URL <https://doi.org/10.1088/0953-4075/22/14/006>.
- [43] Mason, N. J. & Newell, W. R. The polarisation dependence of the simultaneous electron-photon excitation cross section of the helium 2^3s state. *Journal of Physics B: Atomic, Molecular and Optical Physics* **23**, L179–L182 (1990). URL <https://doi.org/10.1088/0953-4075/23/10/003>.
- [44] Wallbank, B., Holmes, J. K. & Weingartshofer, A. Simultaneous electron-photon excitation of He 2^3s : an experimental investigation of the effects of laser intensity and polarisation. *Journal of Physics B: Atomic, Molecular and Optical Physics* **23**, 2997–3005 (1990). URL <https://doi.org/10.1088/0953-4075/23/17/012>.
- [45] Wallbank, B., Holmes, J. K. & Weingartshofer, A. Simultaneous electron-photon excitation of metastable states of rare-gas atoms. *Journal of Physics B: Atomic, Molecular and Optical Physics* **22**, L615–L619 (1989). URL <https://doi.org/10.1088/0953-4075/22/21/002>.

- [46] Wallbank, B., Holmes, J. K. & Weingartshofer, A. Absorption and emission of radiation during electron excitation of the 2^1s and 2^1p states of helium. *Phys. Rev. A* **40**, 5461–5463 (1989). URL <https://link.aps.org/doi/10.1103/PhysRevA.40.5461>.
- [47] Wallbank, B., Holmes, J. K. & Weingartshofer, A. Electron impact excitation of he 2^1P in the presence of a nonresonant laser field. *Can. J. Phys.* **71**, 326 (1993).
- [48] Ajana, I. *et al.* Simultaneous excitation of helium by means of an electron and a photon: A joined experimental and theoretical study. *Atoms* **9** (2021). URL <https://www.mdpi.com/2218-2004/9/3/67>.
- [49] Luan, S., Hippler, R. & Lutz, H. O. Simultaneous electron-photon excitation of helium ($\hbar\omega = 1.17$ eV). *Journal of Physics B: Atomic, Molecular and Optical Physics* **24**, 3241–3249 (1991). URL <https://doi.org/10.1088/0953-4075/24/14/017>.
- [50] Taylor, J. R. *Classical Mechanics* (University Science Books, Mill Valley, California, 2005).
- [51] Joachain, C. J. *Quantum Collision Theory* (North-Holland Publishing Company, Amsterdam, Netherlands, 1975).
- [52] Boas, M. L. *Mathematical Methods in the Physical Sciences* (John Wiley & Sons, Inc., Hoboken, NJ, 2006), 3 edn.
- [53] Bransden, B. H. & Joachain, C. J. *Physics of Atoms and Molecules* (Prentice Hall, Harlow, England, 2003), 2 edn.
- [54] Sakurai, J. J. & Napolitano, J. *MODERN QUANTUM MECHANICS* (Addison-Wesley, San Francisco, CA, 2011), 2 edn.
- [55] Rahman, N. K. Effect of intense electromagnetic wave in charged-particle scattering. *Phys. Rev. A* **10**, 440–441 (1974). URL <https://link.aps.org/doi/10.1103/PhysRevA.10.440>.
- [56] Griffiths, D. J. *INTRODUCTION TO QUANTUM MECHANICS* (PEARSON, 2004), 2 edn.
- [57] Arfken, G. B., Weber, H. J. & Harris, F. E. *MATHEMATICAL METHODS FOR PHYSICISTS* (ELSEVIER, Amsterdam, Netherlands, 2013), 7 edn.
- [58] Matviyenko, G. On the evaluation of bessel functions (1992). URL <https://www.cs.yale.edu/publications/techreports/tr903.pdf>.
- [59] Jackson, J. D. *CLASSICAL ELECTRODYNAMICS* (JOHN WILEY & SONS, INC., Hoboken, NJ, 1999), 3 edn.

- [60] Griffiths, D. J. *INTRODUCTION TO ELECTRODYNAMICS* (PEARSON, Upper Saddle River, New Jersey, 2013), 4 edn.
- [61] Mason, N. J. & Newell, W. R. Simultaneous electron-photon excitation of the helium 2^3s state. *Journal of Physics B: Atomic and Molecular Physics* **20**, L323–L325 (1987). URL <https://doi.org/10.1088/0022-3700/20/10/006>.
- [62] Martin, N. L. S., Weaver, C. M., Kim, B. N. & deHarak, B. A. Free-free experiments: the search for dressed atom effects. *Journal of Physics B: Atomic, Molecular and Optical Physics* **51**, 134003 (2018). URL <https://doi.org/10.1088/1361-6455/aac31b>.
- [63] Peter Schwerdtfeger & Jeffrey K. Nagle (2019) 2018 Table of static dipole polarizabilities of the neutral elements in the periodic table, *Molecular Physics*, 117:9-12, 1200-1225, DOI: 10.1080/00268976.2018.1535143.
- [64] Jablonski, A., Salvat, F., Powell, C. J. & Lee, A. Y. NIST electron elastic scattering cross-section database version 4.0, nist standard reference database number 64 (2016). URL <https://srdata.nist.gov/srd64/>.
- [65] Crosby, D. A. & Zorn, J. C. Dipole polarizability of 2^3S_1 and 2^1S_0 metastable helium measured by the electric deflection time-of-flight method. *Phys. Rev. A* **16**, 488–491 (1977). URL <https://link.aps.org/doi/10.1103/PhysRevA.16.488>.
- [66] Fursa, D. V. & Bray, I. Calculation of electron-helium scattering. *Phys. Rev. A* **52**, 1279–1297 (1995). URL <https://link.aps.org/doi/10.1103/PhysRevA.52.1279>.
- [67] Martin, N. L. S. Private communication (2018).
- [68] Khalil, D., Akramine, O. E., Makhoute, A., Maquet, A. & Taïeb, R. Light polarization effects in laser-assisted elastic electron-helium collisions: a sturmian approach. *Journal of Physics B: Atomic, Molecular and Optical Physics* **31**, 1115–1125 (1998). URL <https://doi.org/10.1088/0953-4075/31/5/018>.
- [69] Akramine, O. E., Makhoute, A., Khalil, D., Maquet, A. & Taïeb, R. Effects of laser polarization in laser-assisted electron-helium inelastic collisions: a sturmian approach. *Journal of Physics B: Atomic, Molecular and Optical Physics* **32**, 2783–2799 (1999). URL <https://doi.org/10.1088/0953-4075/32/12/301>.
- [70] Kramida, A., Ralchenko, Y., Reader, J. & NIST ASD TEAM. NIST atomic spectra database (ver. 5.9) (2021). URL <https://physics.nist.gov/asd>.
- [71] Kim, B. N., Weaver, C. M., Martin, N. L. S. & DeHarak, B. A. Poster Presentation (2019).
- [72] Thompson, D. B. *INVESTIGATION OF COMPLEX IONIZATION AMPLITUDES IN CADMIUM BY ($e,2e$) SPECTROSCOPY*. Ph.D. thesis, University of Kentucky (1994).

- [73] Erdman, P. W. & Zipf, E. C. Low-voltage, high-current electron gun. *Rev. Sci. Instrum.* **53**, 225 (1992).
- [74] Comstock, Oak Ridge, TN. *ELECTROSTATIC ENERGY ANALYZERS*.
- [75] Dahl, D. A. SIMION for the personal computer in reflection. *Int. J. Mass Spectrom* **200**, 3 (2000).
- [76] Quantar Technology Inc., Santa Cruz, CA. *QUANTAR TECHNOLOGY 3300 SERIES OPEN-FACE MCP/RAE SENSORS INSTALLATION AND MAINTENANCE MANUAL* (2013).
- [77] Quantar Technology Inc., Santa Cruz, CA. *QUANTAR TECHNOLOGY MODEL 2401 POSITION ANALYZER INSTALLATION AND MAINTENANCE MANUAL* (1991).
- [78] Quantar Technology Inc., Santa Cruz, CA. *QUANTAR TECHNOLOGY MODEL 3300/2400 SERIES SYSTEM INSTALLATION AND OPERATION MANUAL* (2013).
- [79] ORTEC, Oak Ridge, TN. *Models 9301 and 9301S Fast Preamplifiers Operating and Service Manual* (2002).
- [80] ORTEC, Oak Ridge, TN. *Models 579 Fast-Filter Amplifier Operating and Service Manual* (2002).
- [81] ORTEC, Oak Ridge, TN. *Model 473A Constant-Fraction Discriminator Operating and Service Manual*.
- [82] Continuum, Santa Clara, CA. *Operation and Maintenance Manual for the Powerlite 9000 Series Laser* (1993).
- [83] Stanford Research Systems, Sunnyvale, CA. *MODEL DG535 Digital Delay/Pulse Generator* (2017).
- [84] Koechner, W. *Solid-State Laser Engineering* (Springer, New York, NY, 2006), 6 edn.
- [85] Wolfram Research, Inc. Mathematica, Version 10.3.0.0. URL <https://www.wolfram.com/mathematica>. Champaign, IL, 2015.
- [86] Wolfram Research. Findfit, wolfram language function (2003). URL <https://reference.wolfram.com/language/ref/FindFit.html>.
- [87] Wolfram Research. NonlinearModelFit, wolfram language function (2008). URL <https://reference.wolfram.com/language/ref/NonlinearModelFit.html>.

- [88] Ward, R. *et al.* Differential cross sections for electron impact excitation of the $n = 2$ states of helium at intermediate energies (80, 100 and 120 eV) measured across the complete angular scattering range (0–180°). *Journal of Physics B: Atomic, Molecular and Optical Physics* **44**, 045209 (2011). URL <https://doi.org/10.1088/0953-4075/44/4/045209>.
- [89] Taylor, J. R. *An Introduction to Error Analysis: The study of uncertainties in physical measurements* (University Science Books, Sausalito, California, 1982), 2 edn.

Vita

Brian N Kim

Place of Birth:

- Chicago, IL

Education:

- University of Kentucky, Lexington, KY
M.S. in Physics, Aug. 2019
- Illinois Wesleyan University, Bloomington, IL
B.A. in Physics, Minor in Mathematics, April 2015

Professional Positions:

- Graduate Teaching Assistant, University of Kentucky Fall 2015–Fall 2020
- Graduate Research Assistant, University of Kentucky Summer 2016–Spring 2022

Honors

- Certificate of Outstanding Teaching, College of Arts & Sciences, University of Kentucky (2021)
- Outstanding Teaching Assistant, Department of Physics & Astronomy, University of Kentucky (2020)

Publications:

- N. L. S. Martin, C. M. Weaver, B. N. Kim, and B. A. deHarak, *Phys. Rev. A* **99**, 032708 (2019).
- N. L. S. Martin, C. M. Weaver, B. N. Kim, and B. A. deHarak, *J. Phys. B* **51**, 134003 (2018).
- B. A. deHarak, B. N. Kim, C. M. Weaver, N. L. S. Martin, M. Siavashpouri, and B. Nosarzewski, *Plasma Sources Sci. Technol.* **25**, 035021 (2016)